

DOKUZ EYLÜL UNIVERSITY
GRADUATE SCHOOL OF NATURAL AND APPLIED
SCIENCES

EXPERIMENTAL AND NUMERICAL
INVESTIGATION OF BED LOAD TRANSPORT
IN UNSTEADY FLOWS

by
Gökçen BOMBAR

October, 2009
İZMİR

**EXPERIMENTAL AND NUMERICAL
INVESTIGATION OF BED LOAD TRANSPORT
IN UNSTEADY FLOWS**

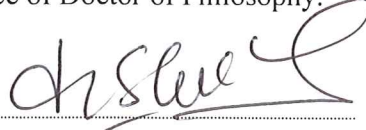
**A Thesis Submitted to the
Graduate School of Natural and Applied Sciences of Dokuz Eylül University
In Partial Fulfillment of the Requirements for the Degree of Doctor of
Philosophy in Civil Engineering, Hydraulics Hydrology Water Resources
Program**

**by
Gökçen BOMBAR**

**October, 2009
İZMİR**

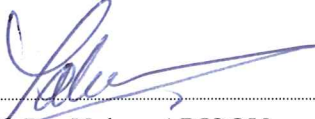
Ph.D. THESIS EXAMINATION RESULT FORM

We have read the thesis entitled “**EXPERIMENTAL AND NUMERICAL INVESTIGATION OF BED LOAD TRANSPORT IN UNSTEADY FLOWS**” completed by **GÖKÇEN BOMBAR** under supervision of **PROF. DR. MEHMET ŞÜKRÜ GÜNEY** and we certify that in our opinion it is fully adequate, in scope and in quality, as a thesis for the degree of Doctor of Philosophy.



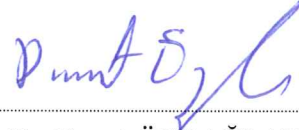
Prof. Dr. Mehmet Şükrü GÜNEY

Supervisor



Prof. Dr. Yalçın ARISOY

Thesis Committee Member



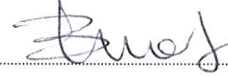
Prof. Dr. Davut ÖZDAĞLAR

Thesis Committee Member



Doç. Dr. Şevket ÇOKGÖR

Examining Committee Member



Yrd. Doç. Dr. Pınar KAYA

Examining Committee Member

Prof. Dr. Cahit HELVACI

Director

Graduate School of Natural and Applied Sciences

ACKNOWLEDGMENTS

I would like to thank my advisor Prof. Dr. M. Şükrü GÜNEY for his patience, guidance, and support during my PhD.

I would like to express my sincere appreciation to retired Prof. Dr. Turhan ACATAY, for his precious advices and suggestions.

I would like to express my sincere thanks to Prof. Dr. Mustafa ALTINAKAR for his invaluable advices who advised this subject to study.

I am grateful to our technician İsa ÜSTÜNDAĞ who participated in the construction of the flume and for his contribution during the experiments.

I am especially indebted to my family for their unfailing support and patience. I would like to thank them to encourage me during my PhD.

I would like to thank to my colleagues Erdi AYDÖNER, Dr. Ayşegül ÖZGENÇ AKSOY, and Mustafa DOĞAN for their help during the experiments. I would like to thank my friends and my colleagues at Hydraulic Laboratory for their helps when I needed. I wish them a successful career.

The financial support provided by the TÜBİTAK (project no 106M274) is gratefully acknowledged.

EXPERIMENTAL AND NUMERICAL INVESTIGATION OF BED LOAD TRANSPORT IN UNSTEADY FLOWS

ABSTRACT

An elaborate experimental system is designed and built in Hydraulics Laboratory of DEU, in order to study bed load transport in unsteady flows caused by different triangular shaped input hydrographs.

The steady flow experiments are performed with fixed and mobile bed. The unsteady flow experiments are conducted by means of hydrographs with discharging from 12.0 l/s to 89.9 l/s.

The bed load is collected at the downstream end of the channel. The sediment motion is recorded by a camera and analyzed by image processing technique. The water depths are also measured. The velocity profiles are obtained by using Ultrasonic Velocity Profiler (UVP). Painted sediments are used to determine the displacements.

The critical point for inception of sediment motion is investigated in the light of available literature and compared with the experimentally obtained results for steady flow case. The bed load values measured in both steady and unsteady flow conditions are compared with those calculated from the empirical relations given in the relevant literature. The most compatible empirical relations are identified.

In image processing analysis, the average grain velocity is investigated throughout the hydrograph. From the camera records, it is revealed that the bed load motion is not continuous, but sporadic, which results in fluctuating character.

In the time lag analysis, when the dimensionless shear stress τ_* obtained from the UVP and dimensionless bed load q_* obtained from the video recordings are used,

a hysteresis is not observed. If the latter is obtained from the baskets a hysteresis of a counter-clock-wise is noted.

The one dimensional governing equations are numerically solved by a finite difference scheme developed by Lax. The bed elevations, the velocity and flow depth variations and the bed loads collected in baskets are compared with the numerical model solutions. An acceptable accordance between experimental findings and numerical results is observed.

Keywords: sediment transport, unsteady flows, mobile bed, image processing, numerical solution

KARARSIZ AKIMLARDA TABAN MALZEMESİ TAŞINMASININ DENEYSEL VE NÜMERİK ARAŞTIRILMASI

ÖZ

Bu çalışmada zamana bağlı akımlarda sürüntü maddesi taşınmasını araştırmak için DEÜ Hidrolik Laboratuvarında kapsamlı bir deney sistemi tasarlanmış ve inşa edilmiştir. Farklı üçgen şekilli giriş hidrografları kullanılarak çok miktarda deney yapılmıştır.

Zamanla değişmeyen kararlı akım şartlarındaki deneyler hem hareketsiz hem de hareketli taban üzerinde gerçekleştirilmiştir. Zamana bağlı olarak değişen kararsız akım deneyleri, debileri 12.0 lt/sn ile 30.3 lt/sn arasında değişen hidrograflar kullanılarak gerçekleştirilmiştir.

Taban malzemesi kanalın mansabında bulunan sepetlerle toplanmıştır. Taban malzemesi hareketi kamera ile kaydedilmiş ve görüntü işleme tekniği ile analiz edilmiştir. Akım derinlikleri ile hız profilleri de deneyler sırasında ölçülmüştür. Taban malzemesinin bir kısmı boyanarak malzemenin hareket mesafeleri elde edilmiştir.

Taban malzemesinin harekete geçişi ile ilgili kritik nokta teorik yaklaşımlar ile incelenmiş ve zamanla değişmeyen kararlı akım şartlarındaki deneylerle elde edilenler ile karşılaştırılmıştır. Zamanla değişmeyen ve zamanla değişen akım şartlarındaki deneylerle elde edilen taban malzemesi yükü, literatürde verilen ampirik denklemler ile hesaplanarak karşılaştırılmıştır. Mevcut ampirik bağıntılardan en uygun olanları belirlenmiştir.

Görüntü işleme tekniği ile yapılan analizde, tüm hidrograf boyunca ortalama dane hızı incelenmiştir. Kamera kayıtlarına göre, taban malzemesi hareketi sürekli değil, kesikli ve dalgalıdır.

Zamansal gecikme analizinde, UVP ölçümlerinden elde edilen boyutsuz kayma gerilmesi τ_* ile video kayıtlarından elde edilen boyutsuz taban malzemesi yükü q_* karşılaştırıldığında bir histerisiz görülmemiştir. Kanal sonundaki sepetlerle ölçülen taban malzemesi kullanıldığında saat yönünün tersi yönündeki bu histerisiz görülmüştür.

Akımın sürekliliği ve taban malzemesinin sürekliliği için verilen bir boyutlu kısmi diferansiyel denklemler ile yayınım (difüzyon) dalgası varsayımı ile verilen momentum diferansiyel denklemleri Lax tarafından önerilmiş sonlu farklar şeması yöntemi ile sayısal olarak çözülmüştür. Deneylerde elde edilen hız ve akım derinliğinin zamanla değişimi, deney sonunda kanaldaki taban kotları ve sepetlerde toplanan taban malzemesi yükü sayısal çözüm sonuçları ile karşılaştırılmıştır. Deneysel ve sayısal sonuçlar arasında kabul edilebilir bir uyum gözlenmiştir.

Anahtar Kelimeler: katı madde taşınımı, zamana bağlı akım, hareketli taban, görüntü işleme, sayısal çözüm

CONTENTS

	Page
THESIS EXAMINATION RESULT FORM	ii
ACKNOWLEDGEMENTS	iii
ABSTRACT	iv
ÖZ	vi
CHAPTER ONE – INTRODUCTION	1
CHAPTER TWO –THEORY OF SEDIMENT TRANSPORT	4
2.1 Steady Flow Case	4
2.1.1 Incipient Motion of Sediment	4
2.1.1.1 Shields approach (1936)	4
2.1.1.2 Meyer, Peter and Müller approach (1948)	5
2.1.1.3 Yang Approach (1973)	6
2.1.2 Empirical Equations for Calculation of Bed Load.....	7
2.1.2.1 DuBoys Equation (1879)	7
2.1.2.2 Schoklitch Equation (1934 & 1943)	8
2.1.2.3 Shields approach (1936).....	9
2.1.2.4 Meyer Peter Equation (1948)	9
2.1.2.5 Meyer, Peter and Müller Equation (1948)	10
2.1.2.6 Rottner Equation (1959)	12
2.1.2.7 Ashida and Michue Equation (1972)	12
2.1.2.8 Engelund and Fredsoe Equation (1976)	12
2.1.2.9 Fernandez Luque and Van Beek Equation (1976)	13
2.1.2.10 Parker (1979) fit to Einstein (1950) Equation	13
2.2 Unsteady Flow Case	13
2.2.1 Time Lag Between τ_* and q_* and Hysteresis	13
2.2.2 Pulsing Nature of Bed Load	19

**CHAPTER THREE –EXPERIMENTAL SET-UP, INSTRUMENTATION
AND PROCEDURE22**

3.1 Experimental Set-up 22

3.2 Bed Material Characteristics 24

3.3 Instrumentation..... 26

 3.3.1 Visualization Experiments for Bed Load Motion Detection..... 26

 3.3.2 Velocity Profile Determination and Bottom Elevation..... 27

 3.3.3 Flow Tracker for Velocity Measurement 29

 3.3.4 Velocity measurement with VS100 30

 3.3.5 Flow meter..... 30

 3.3.6 Level meter..... 31

 3.3.7 Data recorder 31

3.4 Experimental Procedure 32

CHAPTER FOUR –EXPERIMENTS IN STEADY FLOW CONDITIONS35

4.1 Steady Flow Experiments 35

4.2 Threshold of Motion and Mobile Bed 40

4.3 Bed Forms 46

CHAPTER FIVE –EXPERIMENTS IN UNSTEADY FLOW CONDITIONS .49

5.1 Introduction 49

5.2 Flow Depth..... 52

5.3 Data Processing Approaches..... 56

5.4 Mean Point Velocity and Shear Velocity, Mean Cross-sectional Velocity,
 and Flowrate 57

5.5 Bed Load from Sediment Baskets 63

5.6 Bed Load from Image Processing Technique 74

5.7 Relation between Dimensionless Shear Stress and Dimensionless Bed Load 81

5.8 Bottom Elevation	82
5.9 Spatial and Temporal Distribution of Painted Sediments after Hydrograph ...	83
CHAPTER SIX– GOVERNING EQUATIONS OF SEDIMENT TRANSPORT	85
6.1 Differential Equations of One Dimensional Bed Load Transport	86
6.2 Differential Equations of Two Dimensional Bed Load Transport	88
CHAPTER SEVEN– NUMERICAL SOLUTION	91
7.1 Numerical Model	91
7.2 Comparison of Numerical and Experimental Results	95
CHAPTER EIGHT–CONCLUSION.....	99
REFERENCES	103
APPENDIX I - Design and Construction Stages of the Experimental System	112
APPENDIX II - Ultrasonic Velocity Profiler and Its Transducers	137
APPENDIX III – Pump Speed Control Unit Software.....	144

CHAPTER ONE

INTRODUCTION

In open channels flow over mobile bed is a continuous interaction between flowing water and sediment particles. Up to now, several empirical formulae of transported bed load have been developed. Most of these formulas estimating bed load, have been proposed for uniform flow and uniform bed conditions. The laboratory and field studies performed under unsteady flow conditions revealed that there is not a unique relationship between dimensionless shear stress τ_* and dimensionless bed load q_* . The aim of this study is to investigate this hysteresis behavior and the mechanism of sediment inception under hydrographs, also to determine the most appropriate bed load transport formula given in literature.

An elaborate experimental system is designed and built in Hydraulics Laboratory of Civil Engineering Department of Dokuz Eylül University, in order to carry out experiments and study sediment transport in steady and unsteady flows. Numerous flume experiments are conducted using different triangular shaped input hydrographs without sediment feeding at upstream.

The steady flow experiments are done on rough bed with fixed and mobile bed. The unsteady flow experiments are conducted by generating the hydrographs having rising and falling durations ranging from 15 seconds to 120 seconds, with the steady state value of 12.0 l/s and 30.3 l/s and the peak value of 53.5 l/s and 89.9 l/s, without sediment supply from the upstream.

The bed load is collected at the downstream end of the channel. The sediment motion is recorded by a camera and analyzed by image processing techniques. The water depths are also measured. The velocity profiles are obtained during the experiments with Ultrasonic Velocity Profiler (UVP). The grain size distributions of the sediments collected at the baskets are obtained by sieve analysis. Painted

sediments are placed at various sections of the channel and after the passage of the hydrograph; they are collected noting the final locations and their numbers in order to determine the travelled distances.

The hysteresis during the rising and falling stages between the functional relation between dimensionless sediment transport intensity q_* and dimensionless shear stress τ_* is studied.

The number of grains and the area of the moving grains as well as the average velocities of the sediments are determined at two sections of the channels by using the camera records and image processing techniques in order to evaluate the continuous bed load transport during the unsteady flow.

The sediment transport equations are solved and their results are compared with the experimental ones.

The chapter 1 involves a brief introduction of this thesis.

In the 2nd chapter, the theoretical aspects of sediment transport in steady flow conditions are summarized. The initiation of sediment motion and the empirical relations for the bed load are given. The notions related to unsteady flow conditions are also involved in this chapter.

The experimental set-up, instrumentation and experimental procedure are described in the 3rd chapter. The experimental results obtained in steady flow conditions with immobile bed and live bed are given in chapter 4 and those obtained at unsteady flows with different hydrographs are given in chapter 5. The fourth and fifth chapter involve the comparison of experimental results together with empirical relations followed by related interpretations.

The differential equations related to sediment transport are given in chapter 6. The numerical model and comparison between theoretical results obtained from numerical solution and experimental ones are given in chapter 7.

Conclusion and suggestions are stated in chapter 8.

The design and construction stages of the experimental system are given in Appendix I.

Some basic information related to the ultrasonic velocity profiler and its transducers is provided in Appendix II.

Appendix III contains pump speed control unit software.

CHAPTER TWO

THEORY OF SEDIMENT TRANSPORT

2.1 Steady Flow Case

2.1.1 Incipient Motion of Particles

When the flow conditions satisfy or exceed the criteria for incipient motion, sediment particles start to move. In this study the widely used three of the incipient motion criteria are studied. The empirical equations are given in MKS unit system.

2.1.1.1 Shields approach (1936)

To determine the critical point for the determination of the inception of motion of the grains Shields has developed the graph given in Figure 2.1. The horizontal and vertical axes of this figure corresponds to boundary Reynolds number, Re_* , and dimensionless shear stress, τ_* , which are given in equations (2.1) and (2.2) respectively. The shear velocity, u_* is expressed as in equation (2.3).

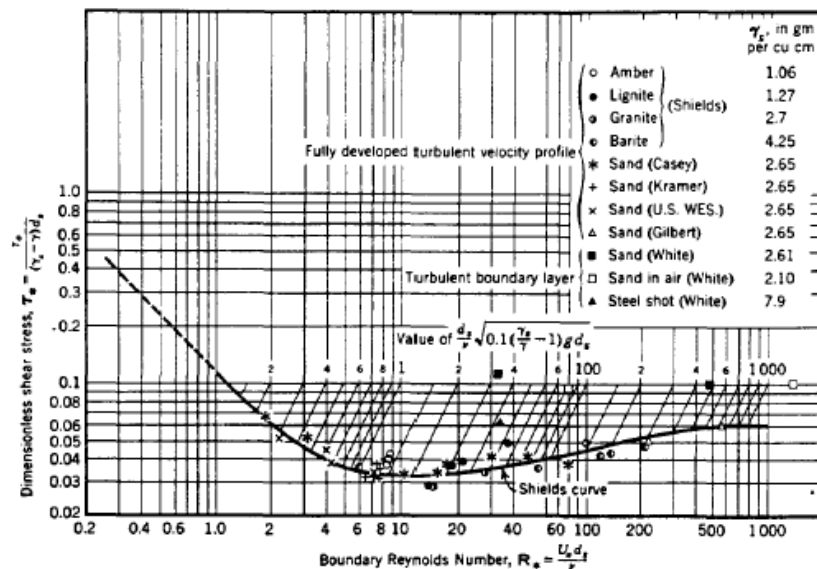


Figure 2.1 Shields graph (Shields, 1936)

$$\text{Re}_* = \frac{u_* d_s}{\nu} \quad (2.1)$$

$$\tau_* = \frac{\tau_0}{\gamma \Delta d_s} = \frac{u_*^2}{g \Delta d_s} \quad (2.2)$$

$$u_* = \sqrt{g H S_0} \quad (2.3)$$

τ_0 can be obtained from equation (2.4).

$$\tau_0 = \gamma H S_0 = \rho u_*^2 \quad (2.4)$$

where g is the gravitational acceleration, $\Delta = (\gamma_s - \gamma)/\gamma$, γ_s and γ are the specific weights of sediment and water respectively, d_s grain diameter, ν kinematic viscosity, H flow depth, S_0 bed slope. By the help of the parameter defined in equation (2.5), the usage of Shields curve becomes easier (Vanoni, 2006).

$$p = \frac{d_s}{\nu} \sqrt{0.1 \Delta g d_s} \quad (2.5)$$

The area below the curve in figure 2.1 means that there is no sediment motion, whereas the area above the curve means that there is sediment motion. The curve gives the critical value of Shields parameter, τ_* , corresponding to the beginning of the motion.

2.1.1.2 Meyer, Peter and Müller approach (1948)

Meyer, Peter and Müller (1948) obtained sediment size at incipient motion as given in equation (2.6).

$$d_s = \frac{S_0 H}{K_1 (n/d_{90}^{1/6})^{3/2}} \quad (2.6)$$

where K_1 is a constant which is 0.058, n is Manning roughness coefficient, d_{90} is the bed material size where 90% of the material is finer (m) and d_s is in mm.

2.1.1.3 Yang Approach (1973)

Yang (1973) obtained incipient motion criteria by obtaining the relationship between the parameters critical velocity V_{cr} (m/s) and v_f (m/s) fall velocity using laboratory data collected by different investigators. This relation is given in equation (2.7a) and equation (2.7b).

$$\frac{V_{cr}}{v_f} = \frac{2.5}{\log(u_* d_s / \nu) - 0.06} + 0.06 \quad \text{if} \quad 1.2 < \frac{u_* d_s}{\nu} < 70 \quad (2.7a)$$

$$\frac{V_{cr}}{v_f} = 2.05 \quad \text{if} \quad 70 \leq \frac{u_* d_s}{\nu} \quad (2.7b)$$

Yang (1996) defined the fall velocity as in equation (2.8).

$$v_f = \begin{cases} \frac{1}{18} \frac{(\gamma_s - \gamma) g d_s^2}{\gamma \nu} \\ F \left[\frac{g d_s (\gamma_s - \gamma)}{\gamma} \right]^{0.5} \\ 3.32 \sqrt{d_s} \end{cases} \quad \text{if} \quad \begin{cases} d_s \leq 0.1mm \\ 0.1mm < d_s \leq 2.0mm \\ d_s > 2.0mm \end{cases} \quad (2.8)$$

where the dimensionless coefficient F is defined as follows

$$F = \begin{cases} \left[\frac{2}{3} + \frac{36 v^2 \gamma}{g d_s^3 (\gamma_s - \gamma)} \right]^{0.5} - \left[\frac{36 v^2 \gamma}{g d_s^3 (\gamma_s - \gamma)} \right]^{0.5} & \text{if } \begin{cases} 0.1\text{mm} < ds < 1.0\text{mm} \\ 1.0\text{mm} < ds < 2.0\text{mm} \end{cases} \\ F = 0.79 & \end{cases} \quad (2.9)$$

2.1.2 Empirical Equations for Calculation of Bed Load

In open channel with mobile bed, there is a continuous interaction between flowing water and sediment particles. Up to now, several empirical formulae of transported bed load have been developed. Most of these formulas estimating bed load, have been proposed for uniform flow and uniform bed conditions.

Sediment transport consists of both bed material transport and suspended sediment. If the motion of sediment particles is rolling, sliding or jumping along the bed, it is called bed load transport (Yang, 1996) Bed load transport is defined as the bed material weight per unit width per unit time, g_b (kg/s/m) or the volume of the transported bed material per unit width per unit time, q_b ($\text{m}^3/\text{s}/\text{m}$) where the relation between them is given in equation (2.10).

$$g_b = \gamma_s q_b \quad (2.10)$$

The empirical formulas derived for bed load calculation are given below.

2.1.2.1 DuBoys Equation (1879)

DuBoys (1879) assumed that the sediment particles move in layers along the bed because of the tractive force acting along the bed as given in equation (2.11) (Yang, 1996).

$$g_b = \psi_1 \tau_0 (\tau_0 - \tau_c) \quad (2.11)$$

where ψ_1 is the sediment coefficient ($\text{m}^3/\text{kg}/\text{s}$), τ_0 and τ_c are bed and critical shear stress (kg/m^2).

where ρ is the density of water ($\text{kg}/\text{m}^4 \cdot \text{s}^2$). ψ_1 and τ_c values can be calculated for various sediment diameters by the help of figure 2.2.

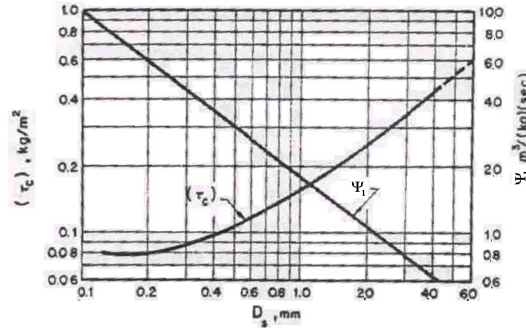


Figure 2.2 The sediment coefficient ψ_1 and critical shear stress τ_c in DuBoys equation (Simons and Şentürk, 1992)

2.1.2.2 Schoklitch Equation (1934 & 1943)

The first of the two equations proposed by Schoklitch (1934) is given in equation (2.12) (Yang, 1996).

$$g_b = 7000 \frac{S_0^{3/2}}{d_s^{1/2}} (q - q_c) \quad (2.12)$$

where d_s is in mm in equation (2.12) and q_c is the incipient motion critical unit flow rate and given by equation (2.13).

$$q_c = \frac{0.01944 d_s}{S_0^{4/3}} \quad (2.13)$$

The second equation proposed by Schoklitch (1943) is given in equation (2.14) and the q_c in this equation is expressed by equation (2.15) (Graf, 1971).

$$g_b = 2500 S_0^{3/2} (q - q_c) \quad (2.14)$$

$$q_c = 0.26 \frac{\Delta^{5/3} d_s^{3/2}}{S_0^{7/6}} \quad (2.15)$$

2.1.2.3 Shields Equation (1936)

Shields (1936) proposed the equation (2.16) for bed load transport which is dimensionally homogeneous (Vanoni, 2006).

$$g_b = 10 \frac{(\tau_0 - \tau_{cr}) q S_0}{\Delta^2 d_s} \quad (2.16)$$

2.1.2.4 Meyer Peter Equation (1948)

Meyer Peter (1948) derived the equation (2.17) that can be applied only to coarse material with particle size greater than 3 mm (Vanoni, 2006).

$$g_b = [250 q^{2/3} S_0 - 42.5 d_s]^{3/2} \quad (2.17)$$

where q is the unit width flow rate ($\text{m}^3/\text{s}/\text{m}$). For nonuniform sediment d_s is taken as equal to D_{35} .

2.1.2.5 Meyer, Peter and Müller Equation (1948)

Meyer, Peter ve Müller (1948) proposed equation (2.18) (Vanoni, 2006).

$$\gamma \left(\frac{K_s}{K_r} \right)^{3/2} R S_0 = 0.047 (\gamma_s - \gamma) d_s + 0,25 \rho^{1/3} g_b^{2/3} \Delta^{2/3} \quad (2.18)$$

where R is the hydraulic radius (m), the coefficients K_r and K_s can be expressed as.

$$K_r = \frac{26}{D_{90}^{1/6}} \quad (2.19)$$

$$K_s = 1/n \quad (2.20)$$

By using the familiar expression for dimensionless bed load q_* given by

$$q_* = \frac{q_b}{\sqrt{\Delta g d_s^3}} \quad (2.21)$$

and by writing $\xi_M = (K_s/K_r)^{3/2}$ and using the common expression of $\tau_0 = \gamma R S_0$, after some algebra described below:

$$(\xi_M) \gamma R S_0 = 0.047 (\gamma_s - \gamma) d_s + 0.25 \left(\frac{\gamma}{g} \right)^{1/3} \left(\frac{\gamma_s - \gamma}{\gamma} \right)^{2/3} g_b^{2/3} \quad (2.22.a)$$

$$(\xi_M) \tau_0 = 0.047 (\gamma_s - \gamma) d_s + 0.25 \left(\frac{\gamma}{g} \right)^{1/3} \left(\frac{\gamma_s - \gamma}{\gamma} \right)^{2/3} g_b^{2/3} \quad (2.22.b)$$

$$\xi_M \frac{\tau_0}{\gamma \Delta d_s} = \frac{0.047 (\gamma_s - \gamma) d_s}{\gamma \left(\frac{\gamma_s - \gamma}{\gamma} \right) d_s} + \frac{0.25}{(\gamma_s - \gamma) d_s} \left(\frac{\gamma}{g} \right)^{1/3} (\gamma_s - \gamma)^{2/3} \left(\frac{g_b}{\gamma_s} \right) \quad (2.22.c)$$

$$\xi_M \frac{\tau_0}{\gamma \Delta d_s} = 0.047 + \frac{0.25}{(\gamma_s - \gamma)^{1/3} d_s} \left(\frac{\gamma}{g} \right)^{1/3} q_b \quad (2.22.d)$$

$$\xi_M \frac{\tau_0}{\gamma \Delta d_s} = 0.047 + 0.25 \left[\frac{q_b \sqrt{\gamma}}{\sqrt{g(\gamma_s - \gamma) d_s^3}} \right]^{2/3} \quad (2.22.e)$$

One arrives at different fashions of the relation between dimensionless volumetric bed load and dimensionless shear stress:

$$\xi_M \tau_* = 0.047 + 0.25 q_*^{2/3} \quad (2.22.f)$$

$$q_* = \left[\frac{\xi_M \tau_* - 0.047}{0.25} \right]^{3/2} \quad (2.22.g)$$

$$q_* = 8(\xi_M \tau_* - 0.047)^{3/2} \quad (2.22.h)$$

ξ_M can be taken as 1, when no bed forms exist, (Graf, 1971). The equation (2.22.h) can be expressed as equation (2.23.a) and (2.23.b) (Wong, 2003).

$$q_* = 8 (\tau_* - \tau_{*cr})^{3/2} \quad (2.23.a)$$

$$q_b = 8 \sqrt{\Delta g d_s^3} (\tau_* - \tau_{*cr})^{3/2} \quad (2.23.b)$$

Wong (2003) revised the equation of Meyer, Peter and Müller, and proposed the expressions given in equations (2.24.a) and (2.24.b) with $\tau_{*cr}=0.047$ and (2.25.a) and (2.25.b) with $\tau_{*cr}=0.0495$.

$$q_* = 4.93 (\tau_* - \tau_{*cr})^{1.6} \quad (2.24.a)$$

$$q_b = 4.93 \sqrt{\Delta g d_s^3} (\tau_* - \tau_{*cr})^{1.6} \quad (2.24.b)$$

$$q_* = 3.97 (\tau_* - \tau_{*cr})^{3/2} \quad (2.25.a)$$

$$q_b = 3.97 \sqrt{\Delta g d_s^3} (\tau_* - \tau_{*cr})^{3/2} \quad (2.25.b)$$

2.1.2.6 Rottner Equation (1959)

Rottner (1959) proposed the following equation (Yang, 1996):

$$g_b = \gamma_s [\Delta \cdot g \cdot H^3]^{1/2} \times \left\{ \frac{V}{[\Delta \cdot g \cdot H]^{1/2}} \left[0.667 \left(\frac{D_{50}}{H} \right)^{2/3} + 0.14 \right] - 0.778 \left(\frac{D_{50}}{H} \right)^{2/3} \right\}^3 \quad (2.26)$$

where V is the mean velocity (m/s).

2.1.2.7 Ashida and Michue Equation (1972)

Ashida and Michue (1972) proposed $\tau_{*cr} = 0.05$ in equations (2.27.a) and (2.27.b).

$$q_* = 17(\tau_* - \tau_{*cr}) (\sqrt{\tau_*} - \sqrt{\tau_{*cr}}) \quad (2.27.a)$$

$$q_b = 17\sqrt{\Delta g d_s^3} (\tau_* - \tau_{*cr}) (\sqrt{\tau_*} - \sqrt{\tau_{*cr}}) \quad (2.27.b)$$

2.1.2.8 Engelund and Fredsoe Equation (1976)

Engelund and Fredsoe (1976) proposed $\tau_{*cr} = 0.05$ in equations (2.28.a) and (2.28.b).

$$q_* = 18.74(\tau_* - \tau_{*cr}) (\sqrt{\tau_*} - 0.7\sqrt{\tau_{*cr}}) \quad (2.28.a)$$

$$q_b = 18.74\sqrt{\Delta g d_s^3} (\tau_* - \tau_{*cr}) (\sqrt{\tau_*} - 0.7\sqrt{\tau_{*cr}}) \quad (2.28.b)$$

2.1.2.9 Fernandez Luque and Van Beek Equation (1976)

Fernandez Luque and Van Beek (1976) proposed $\tau_{*cr} = 0.037 - 0.0455$ in equations (2.29.a) and (2.29.b).

$$q_* = 5.7(\tau_* - \tau_{*cr})^{3/2} \quad (2.29.a)$$

$$q_b = 5.7\sqrt{\Delta g d_s^3} (\tau_* - \tau_{*cr})^{3/2} \quad (2.29.b)$$

2.1.2.10 Parker (1979) fit to Einstein (1950) Equation

Parker (1979), commented the equation of Einstein (1950) and proposed equations (2.30.a) and (2.30.b). The critical dimensionless shear stress is taken as $\tau_{*cr} = 0.03$.

$$q_* = 11.2(\tau_*)^{1.5} [1 - \tau_{*cr}/\tau_*]^{4.5} \quad (2.30.a)$$

$$q_b = 11.2\sqrt{\Delta g d_s^3} (\tau_*)^{1.5} [1 - \tau_{*cr}/\tau_*]^{4.5} \quad (2.30.b)$$

2.2 Unsteady Flow Case

The sediment transport in unsteady flows has been studied with different approaches. It is intended to correlate the flow parameters to the transported sediment amount as in steady flow cases. But the time lag between the flow and the sediment transport is the main issue that is discussed in literature. The pulsing nature of the sediment transport was recorded both in field and in situ studies. The previous studies are discussed in this section.

2.2.1 Time Lag Between τ_* and q_* and Hysteresis

It has been a discussion for the researchers whether there is a unique relationship between dimensionless shear stress τ_* and dimensionless bed load q_* or not under

unsteady flow case for laboratory and field studies. Some researchers claimed that the bed load precedes flow parameters some others claimed the vice versa. The time lag between τ_* and q_* has been investigated with different measurement techniques in laboratory and in situ.

Griffiths and Sutherland (1977) and Bell and Sutherland (1983) have conducted a series of experiments on the transport of sediment under steady and unsteady flows and found that bed load transport rates were essentially the same for experiments in which the sediment was fed to the upstream end of the flume. Their result suggested that for the range of conditions tested, flow unsteadiness does not affect the rate of bed load transport rate unless the bed is degrading.

The experiments of Graf and Suszka (1985) showed that the bed load transport is either in front of or behind the friction velocity, u_* , but they don't proposed any relation about the flow unsteadiness.

Kuhnle (1992) investigated the time lag with field data by measuring the bed load with continuously recording pit samplers. The water depths were measured at a location which is 30 meters before the samplers. He correlated the shear stress with the bed load data. He concluded that at high flow strengths; mean bed load transport rates were greater during rising stages than during falling stages which may be caused by a lag in the formation and destruction of bed roughness elements, bed forms and/or the bed pavement relative to the flow.

Plate (1994) concluded that the moveable bed does not have time to adjust to the fast change of the flow; therefore, a lag-time exists between the occurrence of peak discharge and that of the peak sediment transport rate.

Qu (2003) studied various hydrographs experimentally without sediment feeding. He obtained the shear velocity by fitting the data in the inner region of the flow to log law. He measured the velocity at the 10 m which corresponds approximately to 4m from the downstream end. With the small unsteadiness, the bed load attains its

maximum value preceding the mean velocity, or the discharge and after the friction velocity. However for experiments with large unsteadiness g_b always attains its maximum after them all. He concluded that this may imply that the bed load transport responses slowly to the flow condition with large unsteadiness (Tsujimoto et. al, 1990). This is also obvious in his graphs relating the dimensionless parameters q_* and τ_* (figure 2.3). The relation between them is no more unique for flows with large unsteadiness. The hysteresis loop exists in this relation with a counter-clockwise implying that the dimensionless shear stress arrives at its maximum value before the bed load. This means that the bed load in falling limb is greater than that in rising limb. The time lag is 2.5 s for the 30s+30s hydrograph and 4.4 s for the 10s+10 s hydrograph.

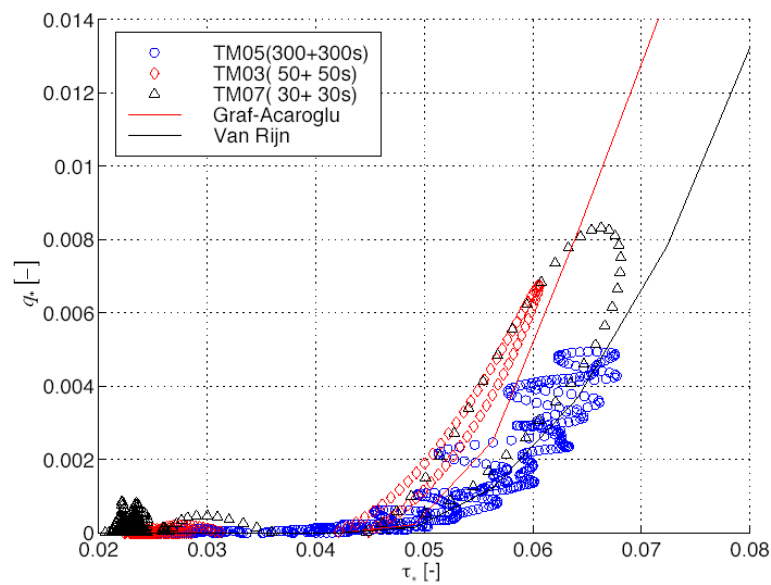


Figure 2.3 Relationship between dimensionless shear stress τ_* and dimensionless bed load q_* (Qu, 2003)

Lee et. al. (2004) conducted a series of flume experiments with triangular hydrograph with small unsteadiness values (with respect to this study and that of Qu (2003)) without sediment supply from the upstream. They concluded that a temporal lag was found between flow hydrograph and the sediment hydrograph peak because large size sand dunes lasted for a short period in the falling limb. The temporal lag

was found to be equal to 6-15% of hydrograph duration. Owing to the temporal lag, the bed load yield in the rising period was less than that in the falling period. They measured the flow depth at 4m, 10m, and 16 m of the flume which is 21 long. The quantity of sediment is recorded by a bed load collector placed at the end of the flume. The bed load fluctuations are induced by existing sand dunes. In order to remove fluctuations in the records, a fast Fourier Transform (FFT) was adopted. They found a significant hysteresis in the bed load transport rates with respect to flow depth but they don't mention the section they considered the flow depth. Because of the inertia of the moveable sand bed, an adjustment time is required to build up the flow corresponding bed load transport rate in the rising period. On the other hand, an adjustment time was needed to adjust the corresponding bed form in the falling period. Consequently, a lower bed load transport rate was found during the rising period; conversely, a higher bed load transport rate was found during the falling period.

Wu et. al (2006) examined the phenomenon of time lag and defined the term as "time lag" and "spatial lag" according to its mechanical reason. The bed-load velocity is smaller than the depth averaged flow velocity, inducing a "time lag" between water and sediment transport. The exchange between the moving sediment and the bed material induces "spatial lag" between flow and sediment transport. They established a depth-averaged 2D model with a non-equilibrium transport approach to simulate unsteady flow and sediment transport which is capable of resolving the temporal and spatial lags. There exists a counter-clock-wise looped curve between flow velocity and sediment discharge. The sediment discharge observed in the experiments is qualitatively predicted by numerical model. It has been demonstrated that the hysteresis is stronger when the hydrograph has steeper rising and falling limbs.

In perennial or snowmelt runoff regimes, sediment is usually supply-limited. Finer grained material is selectively entrained, thus leaving the bed surface armored, and the armor layer is usually covered with microforms such as pebble clusters that increase both flow resistance and bed strength, thereby complicating the relations

between sediment transport and hydraulics (Reid et.al., 1996). In ephemeral streams, the abundant and ready supply of sediment to the channel system ensures that the channel bed remains unarmored (Reid et.al., 1996). In addition, dimensionless transport rates higher than those recorded in perennial or seasonal streams over a similar dimensionless shear stress have been ascribed to a lack of armor development in desert ephemeral systems and to the fact that the supply of sediment from sparsely vegetated desert hill slopes is abundant (Reid et.al., 1995). He also concluded that the equation of Meyer-Peter and Müller (1948) provides the best fit to the empirical data set.

Çokgör and Diplas (2001) examined bed load data from a perennial and ephemeral gravel bed streams and conclude that the pavement layer controls the release of the bed material and greatly influences the transport rates during the passage of a flood. They correlate the bed load with unit width discharge. In the perennial stream, they observed that the majority of the bed material was transported during the falling limb. They suggested that the initial phase of the hydrograph removes the pavement layer and exposes the sub-pavement material, which is more susceptible to erosion, resulting in higher bed load transport rates. This suggestion is supported by their fractional analysis results. For the ephemeral stream case, they concluded that, the rise in bed load transport coincides with that of the water discharge and mentioned that, no coarser pavement layer exists in this ephemeral stream, a feature that is omnipresent in perennial gravel streams. The fact that the distinction between the behaviors of ephemeral and perennial streams contributes to the large scatter present in the bed load transport versus shear stress, or some other flow parameter is highlighted. They concluded that several factors might influence the bed load transport under unsteady flow conditions.

Milhous and Klingeman (1973) showed variability in the direction of the loop between floods that is dependent upon the availability of finer bed load material.

Meade, Emmett, and Myrick (1981) conducted field measurements in East Fork River and provide some useful reasoning for the differences in direction of any

possible hysteric loop by considering the position of sampling locations in relation to sand storage areas: sampling points immediately downstream from bars receive sediment quickly and sediment transport rates are higher on the rising limb; the opposite holds for points distant from bar sediment sources.

Reid et. al. (1985) made field experiments in Turkey Brook, Enfield Chase, 18 km north of London with Birkbeck Bed load Samplers which records the bed load continuously. It drains a London Clay catchment that has a rapid rainfall-runoff response; as a result the hydrograph is flashy. There are point-bars and associated scour pools at the meanders, the straight reaches do not have well-developed bed forms. Alternating low-amplitude bars have a relief of about 10 cm and become obvious only at low flows. The average width is 3m. The armor layer has a median diameter of 22mm that of the bed load is 11 mm. Water stage was recorded at two gauging sites up- and downstream of pit samplers in order to assess changes in water surface slope. The average water-surface slope at this reach is 0.0086. The continuous record reveals that the incidence of bed load in a coarse-grained river channel changes from flood to flood. Reid et. al. (1985) noticed the poor correlation between bed load transport and water stage. They explained this as: Long period of inactivity encourage the channel bed to consolidate sufficiently so that bed load is largely confined to the recession limb of the next-flood wave. But when flood's follow each other closely, the bed material is comparatively loose and offers less resistance to entrainments. In this case substantial amounts of bed load are generated on the rising limb. This is confirmed by values of bed shear stress or stream power at the threshold of initial motion which can be up to five times the overall mean in the case of isolated floods or those which are the first of the season. Nanson (1974) reports greater bed load transport rates on the rising limb than the falling limb in one of the hydrographs.

Govi et.al. (1993) carried out field experiments in Gallina Valley, Italy for continuous recording of bed load transport rates in a coarse-grained alluvial channel in Italian Alps using seismic detectors where the water depth is measured at flow gauging station. 7 hydrographs were investigated. The channel width is from 2m to

6m with a mean slope of 0.013. The transport rate is higher during the rising limb of the hydrograph.

Reid et. al. (1998) made field experiments in Nahal Yatir, an ephemeral stream, and concluded that there is a relative degree of unsteadiness in the bed load curve, but in relative terms, this is not as exaggerated as has been discovered to be characteristic of perennial gravel-bed streams. The comparatively simple bed load response which is the contrast behavior with perennial gravel-bed streams is attributed to the ready and abundant supply of material.

2.2.2 Pulsing Nature of Bed Load

Emmett (1975) reported pulses under steady flow conditions in Slate Cr. Idaho and pointed that the complicated interaction between fluid and bed material need not produce a simple bed load response. He found bed load pulse interval of 6 min – 42 min. Einstein (1937) in his experiments at steady flow condition in Rhine - Switz, found the bed load pulse as 20 hours and accredits it to the passage of sand and gravel waves. Klingeman and Emmett (1982) noted no apparent bed form migration even though bed load transport rates fluctuate rhythmically.

Govi et.al. (1993) stated that the mechanism of bed load transport was inferred from two or three microseismic impulse peaks occurring before and after the discharge peak. The microseismic peaks are thought to reflect the pulsed nature of bed load transport while periods elapsing between them are interpreted as indicating the duration of the transport process independent of the peak discharges. A first peak of microseismic activity occurs earlier than the peak flow. The second or third peak occurs during the recession limb of the hydrograph. Two or three microseismic peaks were associated with bed load pulses, the first coming before the peak flow and the others occurring during the recession limb of the hydrograph. The bed load pulses indicated by microseismic peaks occurred at intervals of 1 to 4 h between the first and second pulses, and 2 to 3 h between the second and third pulses, regardless of the

peak flow. The third pulse can be interpreted as a tail pulse of finer sediment delivery, or as a decrease in sediment transport rate. Microseismic continuous monitoring established that bed load transport occurs in successive pulses in the course of a single flood flow, and that bed load transport precedes the peak flow.

Banzinger and Burch (1990) have tested acoustic devices (hydrophones) in Switzerland in an Alpine stream to estimate bed load transport in mountain torrent by recording the sound generated by gravel collisions. They also found the presence of impulse peaks not coinciding with the flood peak.

Tazioli (1989) made direct field sampling of bed load in the Appennine region and showed that bed load transport occurs with pulses of diversified transport rates and grain size fractions. The coarser fraction appears at the maximum transport rate on the falling limb of the flood hydrograph, several hours after the peak flow.

Billi and Tacconi (1987), Ergenzinger (1988), Reid et.al (1985) have shown that sediment transport during one flood occurred in the form of pulses or waves at practically even intervals; the time intervals changed from about 30 min to 7 h, depending on basin characteristics and location.

Reid et.al. (1985) characterized the bed load by a series of pulses with a mean periodicity of 1.7 hours. In the absence of migrating bed forms, they speculated on the appositeness of Langbein and Leopold's (1968) application of kinematic wave theory to bed load. The pulses are due to stream wise differences in the concentration of particles in a slow-moving traction carpet.

Lee et. al (2004) also observed the rhythmic fluctuation in their experiments while measuring the bed load continuously and attributed this phenomenon to the migrating dunes. Higher frequency fluctuation was associated with a shorter wavelength and a smaller dune height, which was usually induced in a lower peak-flow run. Conversely, lower frequency fluctuation was associated with runs with higher peak flow because a longer wavelength and a larger size sand dune were

induced under higher peak flow. Moreover, the scale of the fluctuation, that is, the size of the sand dune grew in the rising of the hydrograph and shrank during the falling period of the hydrograph.

Jong and Ergenzinger (1994) measured bed load electronically down to sub-second frequency during flood flows by using magnetically sensitive sills. The largest pulses occurred during the ascending and descending flood limbs.

Tacconi and Bill (1987) obtained pulses with a period of about 30 minutes. Hubbell et.al. (1987) observed similar short period pulses and related them to the movement of bed forms in his experiments in a special flume (Ergenzinger, 1988).

CHAPTER THREE

EXPERIMENTAL SET-UP, INSTRUMENTATION AND PROCEDURE

3.1 Experimental Set-up

Experimental studies are carried out on an experimental system involving a rectangular flume of 80 cm width and 18.6 m length. The transparent sides of the flume made from plexiglas are 75 cm high. The slope of flume may be changed from horizontal to 0.01. The water is circulated continuously. The volume of the water supply reservoir (main tank) is 27 m³. The experimental set-up and the locations of the instruments are given in figure 3.1. The general view of the experimental set-up is given in figure 3.2.a and figure 3.2.b. The design and construction stages of the experimental system are given in Appendix I.

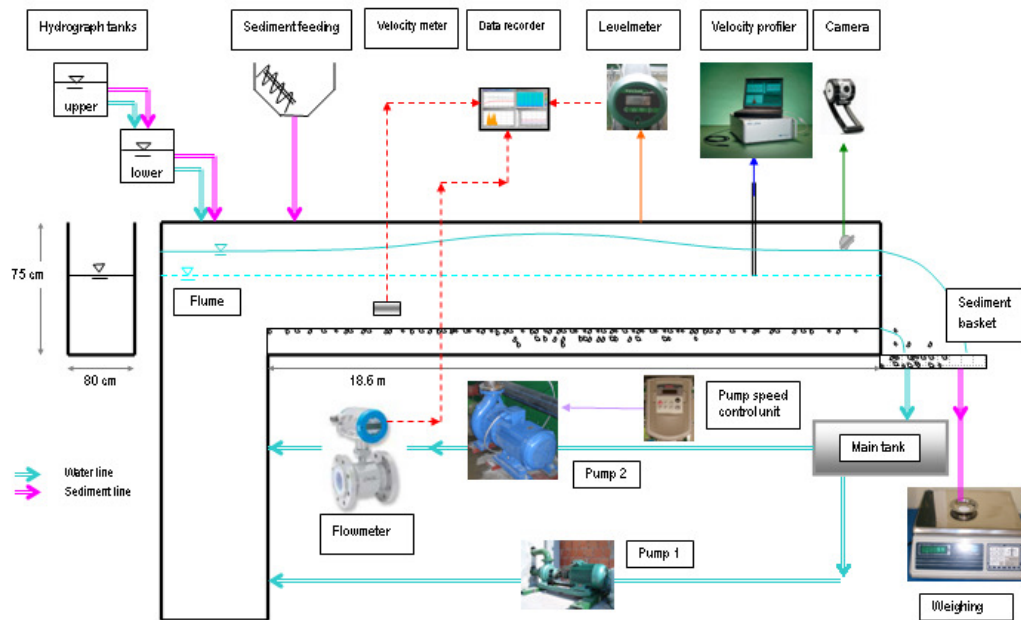


Figure 3.1 The scheme of the experimental set-up.



Figure 3.2a and b The general view of the experimental set-up.

The main tank and rectangular Bazin weir are located at the downstream end of the channel as given in figure 3.3.a. A tail gate is built in order to obtain the desired water depths as shown in figure 3.3.b.

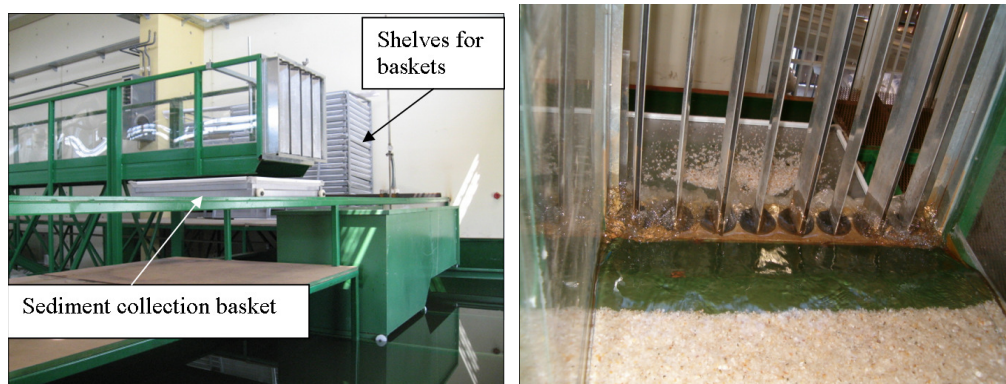


Figure 3.3 (a) The downstream part of the experimental set-up, (b) tail gate

The bed load coming from the flume is collected in the sediment baskets located at the downstream part of the flume as given in figure 3.4.a. There are 60 baskets totally. Each basket collects sediments during 15 s, and changed with an empty new one. After the drying of the sediments in the baskets placed in the shelves, the collected material is weighed with a balance having a 10 kg capacity and 1 gr accuracy as given in figure 3.4.b.

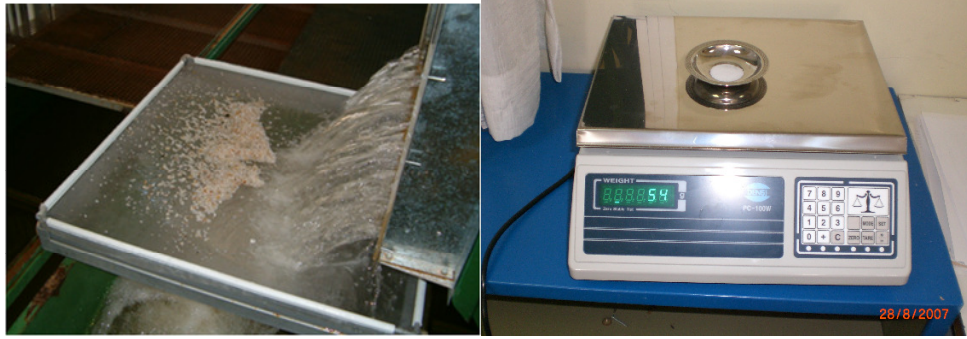


Figure 3.4 (a) The sediment baskets, (b) balance

The experimental system contains two supply lines with two pumps. The Pump 1 has a maximum capacity of 30 l/s. The Pump 2 used in this study (figure 3.5.a), has a maximum capacity of 100 l/s, and connected to pump rotational speed control unit (figure 3.5.b) which can control the flow rate by adjusting the settings. It is also possible to program the device for hydrograph generation. It is possible to increase and decrease the pump speed at desired time increments by software Drive Link-C. The detail of the software is given in Appendix II. The power of the pump is 18.5 kW and the maximum rotational speed is 1450 rpm.

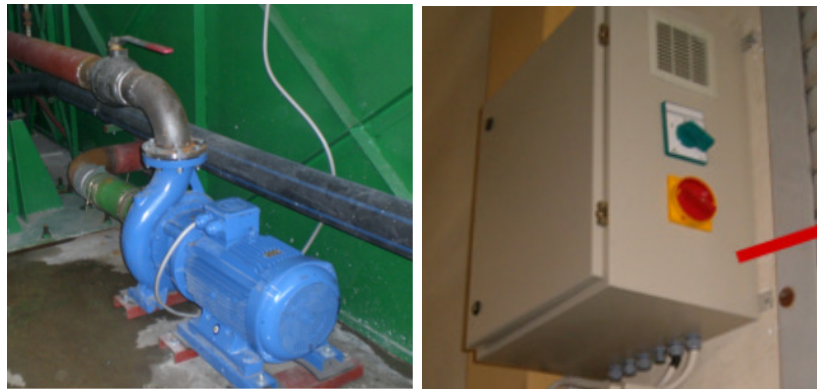


Figure 3.5 (a) Pump 2 used in this study, (b) pump rotational speed control unit

3.2 Bed Material Characteristics

Bed material used in the flume is composed of uniform graded material with $D_{50}=4.8$ mm. The geometric standard deviation is $\sigma_g=1.4$ mm which implies that the sediment may be assumed as uniform. The used bed material is shown in figure 3.6.



Figure 3.6 Sediments used in this study

Sieve analysis is performed with 5 different samples taken at different locations of the channel as given in table 3.1 and the average grain size distribution is obtained as given in figure 3.7.

Table 3.1 Results of sieve analysis to obtain grain size distribution

Grain size (mm)	Sample1	Sample2	Sample3	Sample4	Sample5	Mean
1	0	0	0	0	0	0
2	0.2	0.1	1.19	1.36	1.44	0.86
4	29.2	24.7	31.7	39.7	10.8	33.21
8	99.0	98.6	98.3	99.4	99.0	98.85
16	100	100	100	100	100	100
D_{50}	4.9	5.1	4.8	4.5	4.5	4.8
D_{10}	2.5	2.6	2.4	2.3	2.3	2.4
D_{60}	5.4	5.6	5.4	5.1	5.0	5.3
D_5	2.2	2.3	2.2	2.1	2.1	2.2
D_{95}	7.7	7.7	7.7	7.6	7.6	7.7
D_g	4.6	4.8	4.6	4.3	4.2	4.5
σ_g	1.4	1.3	1.4	1.4	1.4	1.4

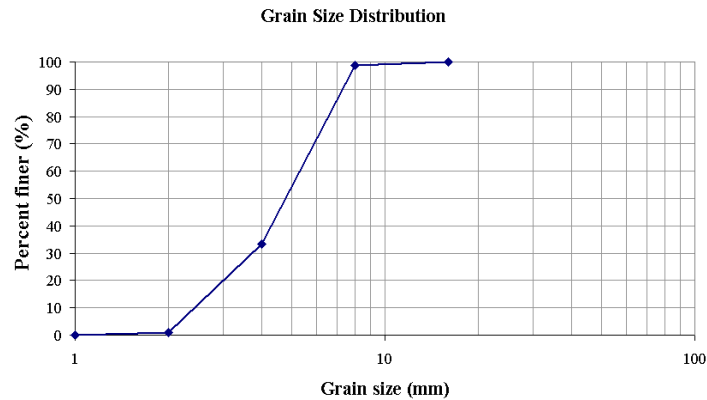


Figure 3.7 Grain size distribution of the bed material

3.3 Instrumentation

3.3.1 Visualization Experiments for Bed Load Motion Detection

The bed-load transport in unsteady flows is recorded by a 640x480 pixel 25 fps SONY CCD camera located at 11m and 16m from the channel entrance mounted vertically (figure 3.8). An acrylic plate is used to prevent disturbance of the wavy surface. While the flow depth increasing, the acrylic plate was raised over the water surface keeping it in contact with the water surface, and then lowered in accord with the decrease in flow depth. The observation area is 17.0 cm by 12.2 cm. The records are analyzed by image processing techniques to determine the number and area of active grains moving at any instant. The average velocity of the grains in two consecutive frames is also obtained. Also some grains which are moving are tracked and their instantaneous velocities are determined. The area of moving grains is also determined by the same technique. This helped to interpret the effect of unsteadiness on the bed-load inception and on the bed-load transport rate.

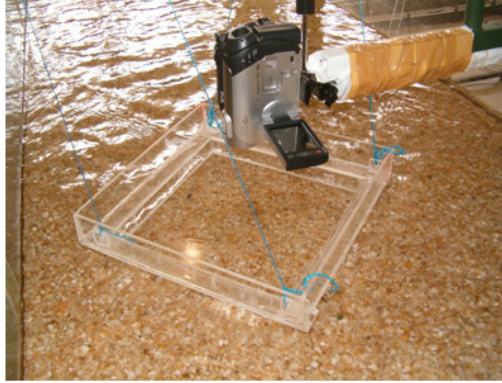


Figure 3.8 Configuration of camera and acrylic plate

3.3.2 Velocity Profile Determination and Bottom Elevation

The velocities are measured by using UVP given in figure 3.9.a (manufactured by Met-Flow SA). The velocity profile along the ultrasonic beam axis is measured by detecting the doppler shift frequency. The measurement principle is as follows; the UVP DUO transducer transmits a short emission of ultrasound, which travels along the measurement axis, and then switches over to receiving. When the ultrasound pulse hits a small particle in the liquid, part of the ultrasound energy scatters on the particle and echoes back. The echo reaches the transducer after a time delay. If the scattering particle is moving with a non-zero velocity component into the acoustic axis of the transducer, doppler shift of echoed frequency takes place, and received signal frequency becomes ‘doppler-shifted’. By using the time delay and doppler shift frequency, it is then possible to calculate both position and velocity of a particle on the measuring axis, i.e. velocity profile over the measuring axis, as depicted in figure 3.9.b (Met-Flow, 2002). A more comprehensive review is provided in Appendix III.

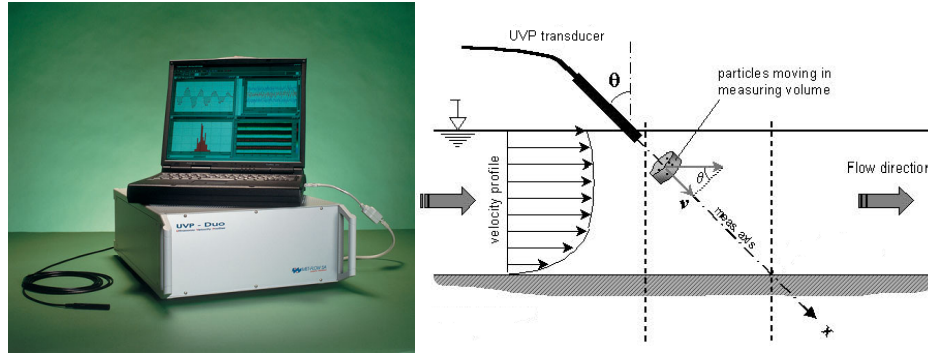


Figure 3.9 (a) Ultrasonic Velocity Profiler (UVP), (b) UVP working principle

The UVP is equipped with transducers having an emitting frequency of 2 MHz. The UVP transducers are placed at two sections of the channel. During the flood, the flow depth increases and decreases in the flume. Mobile transducer which is looking downwards and adaptor given in figure 3.10.a and 3.10.b, is manually increased and decreased in conjunction with the flow depth keeping the tip of the transducer in the water.



Figure 3.10 (a) and (b) Manually controlled mobile transducer

Like all the ultrasonic instruments, UVP needs seeding particles for the velocity measurements. The electrolysis is used for the generation of the hydrogen bubbles. The system working with direct current is presented in Fig. 3.11.a and 3.11.b.

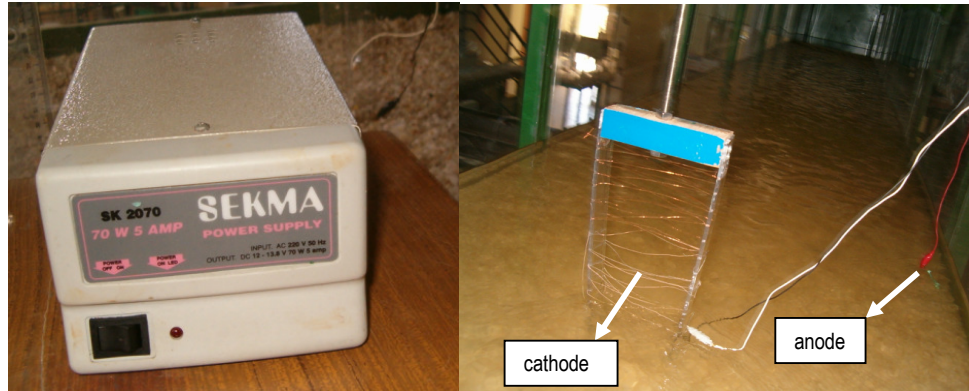


Figure 3.11 (a) Direct current generator, (b) anode and cathode locations

The 8 mm diameter UVP transducer of 4 cm length with an emitting sound frequency of 4 MHz with 2 cycles is used to obtain the bottom elevation in the flume.

3.3.3 Flow Tracker for Velocity Measurement

During steady and unsteady flow experiments at immobile bed, the velocity measurements are performed with Flow Tracker (manufactured by SonTek) given in figure 3.12.a. Flow tracker uses ultrasonic method as UVP does. It measures the point velocity in three directions. After measurements it is connected to a computer as given in figure 3.12.b and the data is transferred.



Figure 3.12 (a) Flow Tracker, (b) connection to a computer

3.3.4 Velocity measurement with VS100

The velocity meter measures the velocity by means of its transducer and sends the information to the multichannel data recorder (figure 3.13).

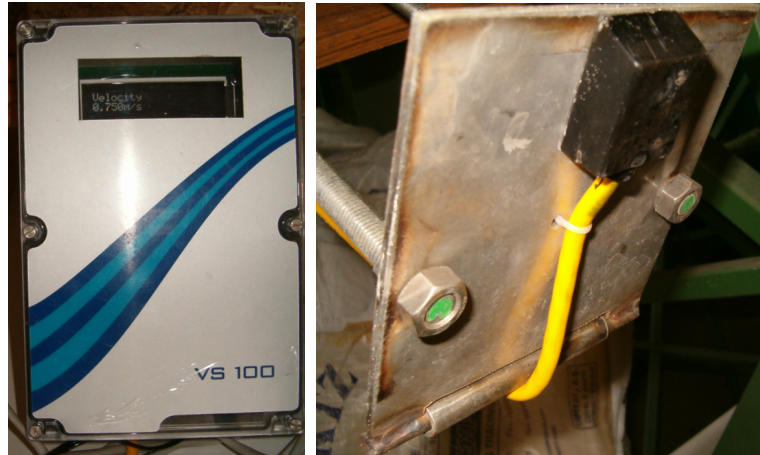


Figure 3.13 (a) The velocity meter, (b) transducer of the velocity meter

3.3.5 Flow meter

The OPTIFLUX 1000 (manufactured by Krohne) is an electromagnetic flow sensor which works according to the Faraday Law and is mounted on the pipe before the entrance of the channel (figure 3.14). It can measure both the steady and unsteady flow rates with a precision of 0.01 l/s. The measured data is sent to the data recorder, with 6 channels.



Figure 3.14 The flow meter

3.3.6 Level meter

The IMP+ level monitoring system (Pulsar Process Measurement Limited) is a highly developed ultrasonic level measurement system which provides non-contacting level measurement for a wide variety of applications in both liquids and solids (figure 3.15.a). It operates on the principle of timing the echo received from a measured pulse of sound transmitted in air and utilizes echo extraction technology. IMP 3 model has a range from 0.15m to 3.00m. The output voltage 4-20mA is transmitted by a RS232 connection to the data recorder. Whilst in the Run Mode, the 4 digit LCD can display the current level reading in mm. The mobile system for level meter is given in figure 3.15.b.



Figure 3.15 (a) IMP+ level meter (b) the mobile system for level meter

3.3.7 Data recorder

The data from the flow-meter and level-meter is recorded and stored by the data recorder as shown in figure 3.16. The data recorder has 6 channels which can acquire the data with a frequency of 1s. The data is both displayed on the screen and stored simultaneously and can be transferred to the computer by the help of the CF card after the experiments.



Figure 3.16 The data recorder

3.4 Experimental Procedure

The steady flow experiments are conducted both in the immobile bed with discharges below the threshold for bed particle motion and live bed with discharges above the threshold for bed particle motion.

The unsteady flow experiments are conducted with rough live bed with discharges above the threshold for bed particle motion.

The steady flow experiments with immobile bed are conducted in the flume with a bottom slope of 0.001.

In order to get the movement of the bed load, the channel slope is increased to 0.005. The steady immobile and mobile bed experiments and the unsteady flow experiments are conducted in the flume with a bottom slope of 0.005.

In unsteady flow experiments, the bed is fixed with small concrete blocks at the first 3m of the flume. The total length of the mobile bed is 15.6 m. The sediment layer thickness is 8 cm along the flume.

Before the unsteady flow experiments, the flume bed is mixed to achieve homogeneity through the vertical and stream-wise direction and the regular bed slope is formed by the mobile system shown in figure 3.17.a and 3.17.b. The bottom slope of 0.005 is verified by using both limnimeter and tripod. The measured bottom elevations are given in figure 3.18.



Figure 3.17 (a) and (b) System to provide the bed slope at a fixed value

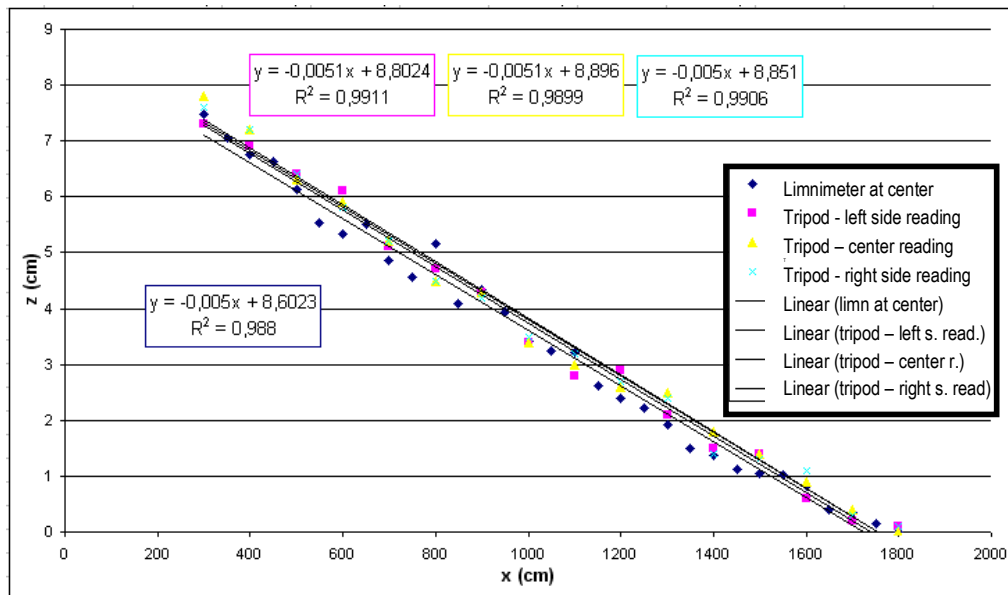


Figure 3.18 Bottom elevation obtained before experiments

No sediment is fed from the channel entrance during the first experiments. The flow rate at the beginning is slowly increased to the base value which is below the sediment inception threshold conditions in order not to disturb the sediments.

For the mobile bed conditions, the transported bed load is collected by sediment baskets located at the downstream part of the flume. Each basket collected bed load for 15 s, and then replaced with an empty new one. After a time required for the sediments to be dried, the bed material is weighed. In unsteady flows, the sieve analysis is performed for each group of sediments collected in the baskets in order to obtain the variation of the grain size distribution with respect to time.

In the cases of steady flow, the flow rate is measured by the rectangular Bazin weir located at the end of the flume and compared with the UVP data, and also flowmeter.

The sampling frequency is selected as 4 Hz and the total sampling time is specified according to hydrograph durations. The channel distance is 0.74 mm on the measuring axis. The sampling frequency of 4 Hz means 0.25 s between each profile. The emitting sound has 2 cycles and the number of repetitions is 180. The flow velocity resolution is 5,8 mm/s. Minimum on-axis velocity is -1.480,2 mm/s and maximum on-axis velocity 0 mm/s is taken. All the measurements with UVP are initiated 2 minutes before the hydrograph.

CHAPTER FOUR

EXPERIMENTS IN STEADY FLOW CONDITIONS

4.1 Steady Flow Experiments

Before the experiments in unsteady flow conditions, some steady flow experiments are conducted in order to find the flow depths, velocity distributions, mean cross-sectional velocities and flow rates at bed slope $S_0=0.005$. The inception parameters of sediment motion are determined and the bed load is experimentally obtained in the case of flows greater than the threshold value.

The local velocities are measured instantaneously and sectional velocity distributions are determined by UVP for eight different flow rates. The flow depths are obtained by taking the averages of the flow depths measured at several sections of the channel. The flow rates, Q, flow depths, H, mean cross-sectional velocities, V, flow area, A, wetted perimeter, P and hydraulic radius, R for the conducted experiments are given in Table 4.1.

In steady uniform flows the shear velocity, u_* is obtained from the equation (4.1).

$$u_* = \sqrt{gHS_0} \quad (4.1)$$

where g is the gravitational acceleration and S_0 is the channel bed slope.

Table 4.1 Hydraulic parameters related to experiments

Experiment no	Q (l/s)	H (cm)	V (cm/s)	A (m ²)	P (m)	R (cm)
1	12.0	4.0	37.5	0.032	0.880	3.6
2	24.7	5.9	52.3	0.047	0.918	5.1
3	36.0	7.2	62.5	0.058	0.944	6.1
4	46.7	8.3	70.3	0.066	0.966	6.9
5	56.3	9.3	75.7	0.074	0.986	7.5
6	68.0	10.2	83.3	0.082	1.004	8.1
7	79.2	11.1	89.2	0.0888	1.022	8.7
8	90.2	12.0	94.0	0.096	1.040	9.2

The longitudinal instantaneous velocity, u is expressed as the sum of the mean value, \bar{u} and the fluctuating component, u'

$$u = \bar{u} + u' \quad (4.2)$$

The longitudinal velocity in the inner region ($z/H < 0.2$), can be expressed by the universal law of the wall (Graf and Altınakar, 1998):

$$\frac{u}{u_*} = \frac{1}{\kappa} \ln \frac{z}{k_s} + B_r \quad (4.3)$$

where u_* =shear velocity, κ = von Karman constant (commonly equal to 0.40), k_s is the equivalent (Nikuradse) sand roughness for the rough bed and is taken as $2.5 D_{50}$, B_r = integration constant for rough beds which may be taken equal to $8.5 \pm 15\%$. It is possible to obtain the shear velocity, by applying least square fitting method in logarithmic coordinates.

The log law fit curves and the mean longitudinal velocity distributions for the experiments are given in figure 4.1 to figure 4.8.

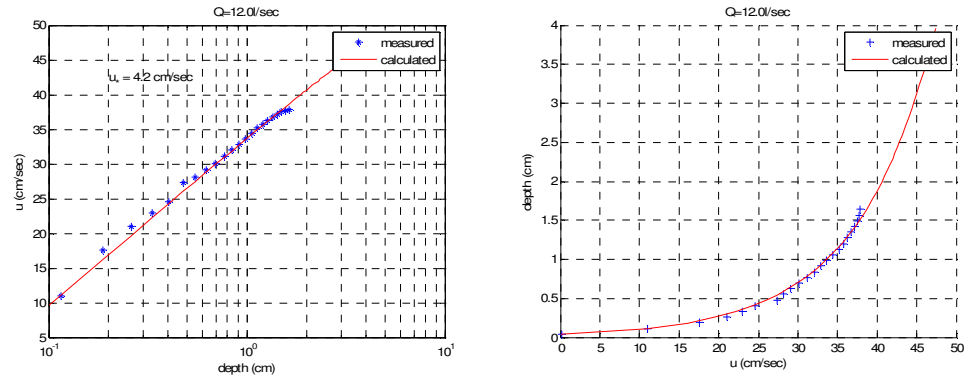


Figure 4.1 (a) determination of shear velocities by using least square fitting method for 12.0 l/s
(b) longitudinal velocity distribution

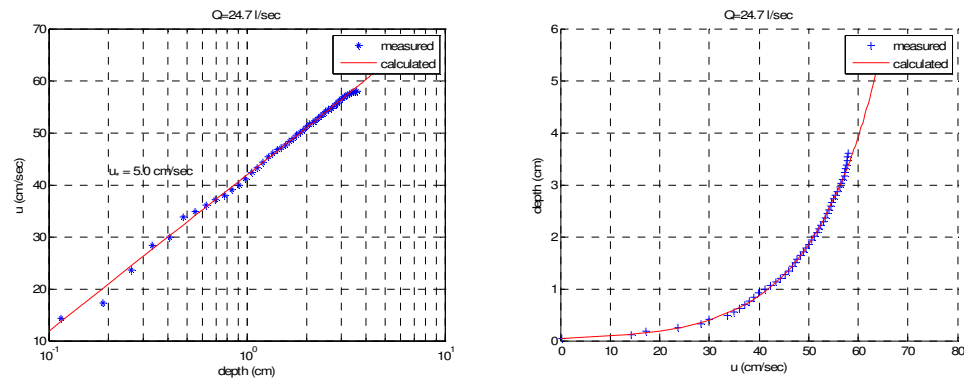


Figure 4.2 (a) determination of shear velocities by using least square fitting method for 24.7 l/s
(b) longitudinal velocity distribution

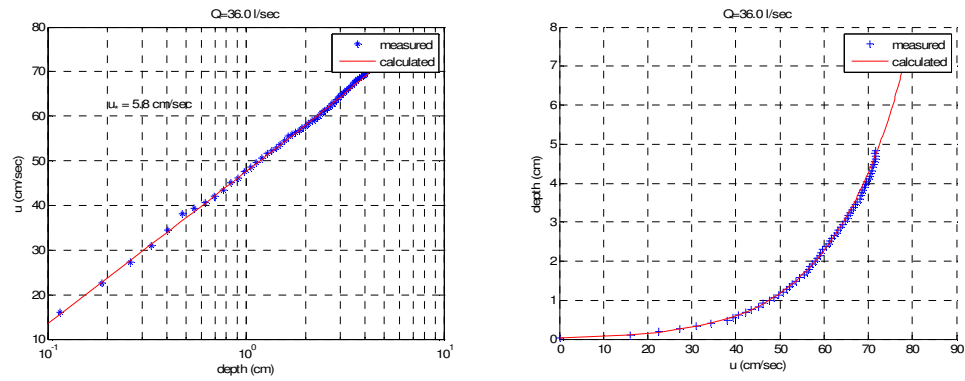


Figure 4.3 (a) determination of shear velocities by using least square fitting method for 36.0 l/s
(b) longitudinal velocity distribution

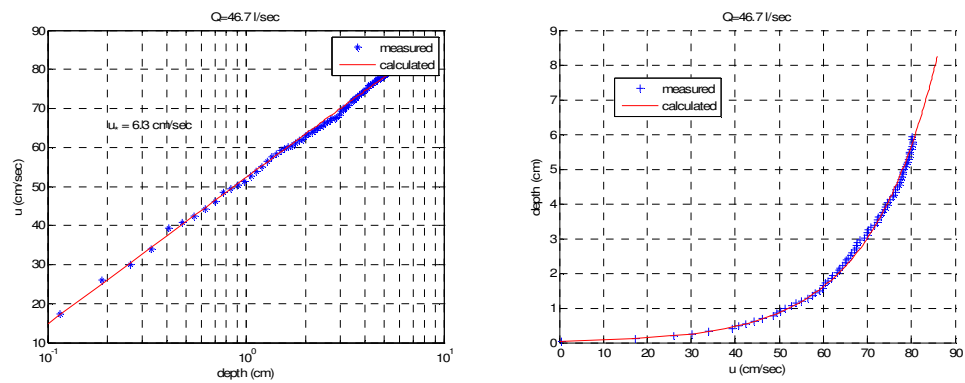


Figure 4.4 (a) determination of shear velocities by using least square fitting method for 46.7 l/s
(b) longitudinal velocity distribution

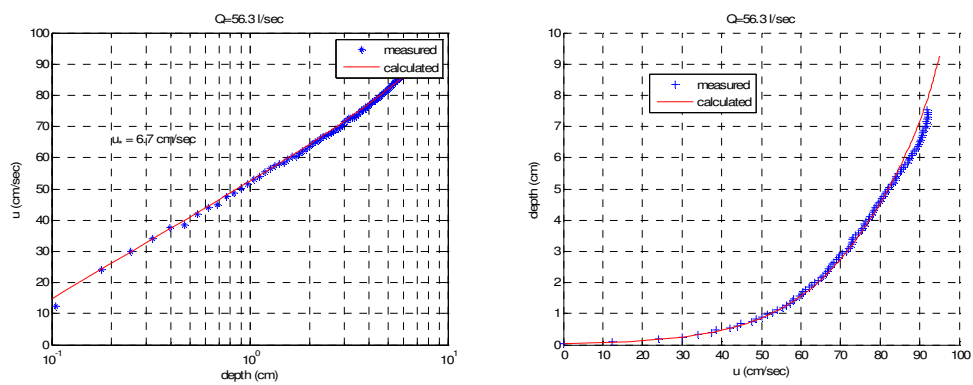


Figure 4.5 (a) determination of shear velocities by using least square fitting method for 56.3 l/s
(b) longitudinal velocity distribution

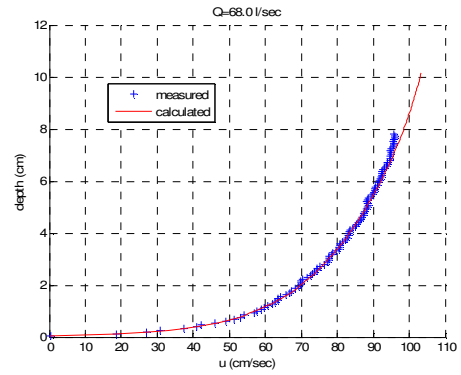
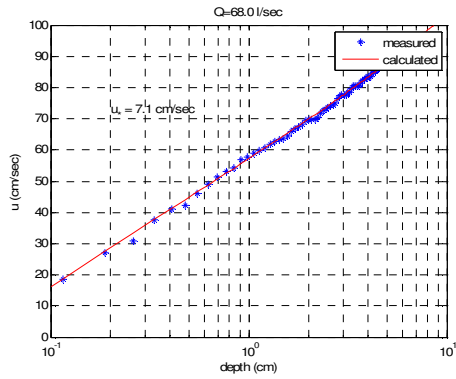


Figure 4.6 (a) determination of shear velocities by using least square fitting method for 68.0 l/s
(b) longitudinal velocity distribution

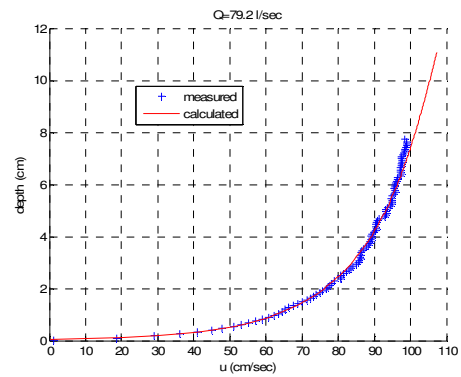
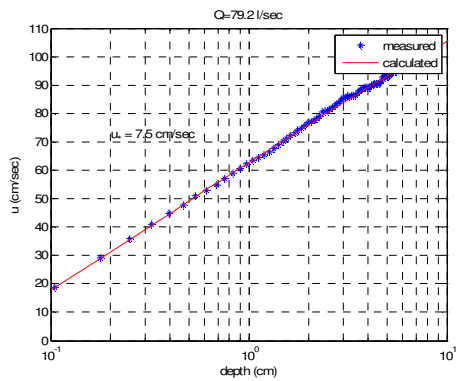


Figure 4.7 (a) determination of shear velocities by using least square fitting method for 79.2 l/s
(b) longitudinal velocity distribution

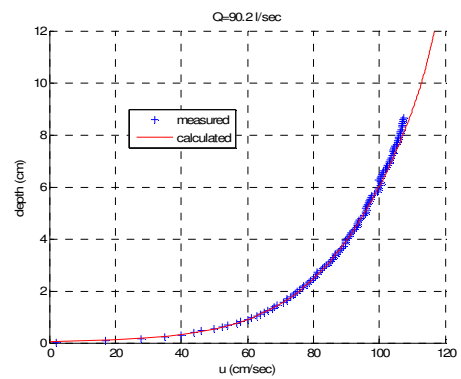
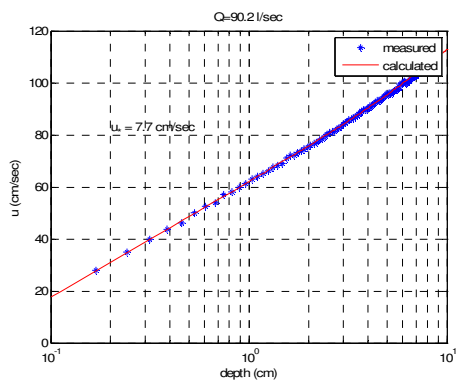


Figure 4.8 (a) determination of shear velocities by using least square fitting method for 90.2 l/s
(b) longitudinal velocity distribution

The shear velocities determined from equation (4.1) and log-law described by equation (4.3), are given in table 4.2.

Table 4.2 Hydraulic parameters related to experiments

Experiment no	Q (l/s)	u_* (cm/s) (Eq 4.1)	u_* (cm/s) (Eq. 4.3)
1	12.0	4.4	4.2
2	24.7	5.4	5.0
3	36.0	5.9	5.8
4	46.7	6.4	6.3
5	56.3	6.8	6.7
6	68.0	7.1	7.1
7	79.2	7.4	7.5
8	90.2	7.7	7.7

4.2 Threshold of Motion and Mobile Bed

At steady flow conditions with different flow rates, the inception of sediment motion is investigated and the bed load is measured by baskets for duration of 30 minutes, if there is any. The time increment for the bed load measurement is 15 seconds.

The parameters of bed load experiments are given in Table 4.3. Here Q is the flow rate, H is the flow depth, V is the cross-sectional mean velocity, Fr is the Froude number, Re is the Reynolds number, τ_{*cr} is the dimensionless critical shear stress, u_* is the shear velocity, τ_0 is the shear stress, Re_* is the dimensionless Reynolds number, τ_* is the dimensionless shear stress. The Re_* and τ_* are expressed in equations (4.4) and (4.5) respectively. τ_{*cr} and τ_{cr} are obtained from Shields curve given in Fig. 2.1.

$$\text{Re}_* = \frac{u_* D_{50}}{\nu} \quad (4.4)$$

$$\tau_* = \frac{u_*^2}{g\Delta D_{50}} \quad (4.5)$$

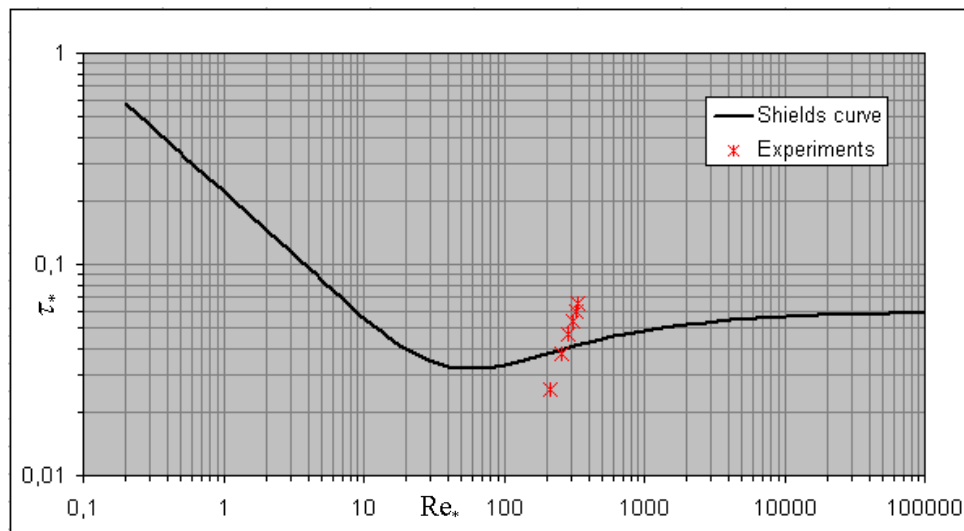
Table 4.3 The flow parameters of the experiments for the steady flow conditions

Experiment no	1	2	3	4	5	6
Q (l/s)	12.0	24.7	36.0	46.7	56.3	68.0
H (cm)	4.0	5.9	7.2	8.3	9.3	10.2
V (cm/s)	37.5	52.3	62.5	70.3	75.7	83.3
q (m ³ /s/m)	0.015	0.031	0.045	0.058	0.070	0.085
u_* (cm/s)	4.43	5.38	5.94	6.38	6.75	7.07
τ_0 (kg/m ²)	0.200	0.295	0.360	0.415	0.465	0.510
τ_*	0.026	0.038	0.046	0.053	0.060	0.066
Re_*	212	257	284	305	323	338
τ_{cr} (kg/m ²)	0.303	0.315	0.320	0.324	0.328	0.330
τ_{*cr}	0.0383	0.0397	0.0404	0.0409	0.0414	0.0417
$Fr = \frac{V}{\sqrt{gH}}$	0.60	0.69	0.74	0.78	0.79	0.83
$\text{Re} = \frac{V4R}{\nu} (10^6)$	0.05	0.11	0.15	0.19	0.23	0.27

The approaches for the critical point for inception of sediment motion are given in Table 4.4 together with the experimental observations. The sediment motion is denoted by (+) and no motion is denoted by (-). The experimental results are plotted on Shields curve and depicted in figure 4.9.

Table 4.4 Inception of sediment motion (+ : yes motion, - : no motion)

Experiment no	1	2	3	4	5	6
Q (l/s)	12.0	24.7	36.0	46.7	56.3	68.0
Experimental results	-	-	+	+	+	+
According to Shields approach Figure (2.1)	-	-	+	+	+	+
According to MPM approach Equation (2.6)	-	-	-	-	-	+
According to Yang's approach, $V_{cr}=0.47$ m/s Equation (2.7)	-	+	+	+	+	+

Figure 4.9 The Shields curve and the experimental values of Re_* and τ_*

The calculated bed load values from the empirical equations and measured ones are given in Table 4.5 and depicted in figure 4.10.

Table 4.5 The bed load values experimentally determined and the bed load values calculated from empirical equations

Experiment no	1	2	3	4	5	6
Q (l/s)	12.0	24.7	36.0	46.7	56.3	68.0
Experiment, g_b (gr/s/m)	-	-	0.2	7.8	25.1	40.7
Du Boys (1879) Equation (2.11)	-	-	-	-	3.5	15.3
Schoklitch (1934) Equation (2.12)	-	-	-	-	-	-
Schoklitch (1943) Equation (2.14)	-	-	-	-	-	-
Shields (1936) Equation (2.16)	-	-	6.9	20.2	36.7	58.5
Meyer, Peter (1948) Equation (2.17)	-	-	-	4.5	12.0	23.1
Meyer, Peter, Müller (1948) Equation (2.23)	-	-	-	13.2	42.0	74.3
Meyer, Peter, Müller (1948) Equation (2.24)	-	-	-	4.9	16.8	30.8
Meyer, Peter, Müller (1948) Equation (2.25)	-	-	-	2.9	15.1	29.8
Rottner (1959) Equation (2.26)	-	-	0.9	6.3	13.6	33.2
Ashida, Michue (1972) Equation (2.27)	-	-	-	1.5	12.4	30.6
Engelund, Fredsoe (1976) Equation (2.28)	-	-	-	16.7	57.3	103.1
Fernandez Luque, van Beek (1976) Equation (2.29) $\tau_{*cr} = 0.037$	-	0.6	18.1	42.3	69.6	97.7
Fernandez Luque, van Beek (1976) Equation (2.29) $\tau_{*cr} = 0.0455$	-	-	0.5	14.1	34.6	57.5
Parker (1979) fit to Einstein (1950) Equation (2.30)	-	0.1	1.0	3.4	7.1	12.0

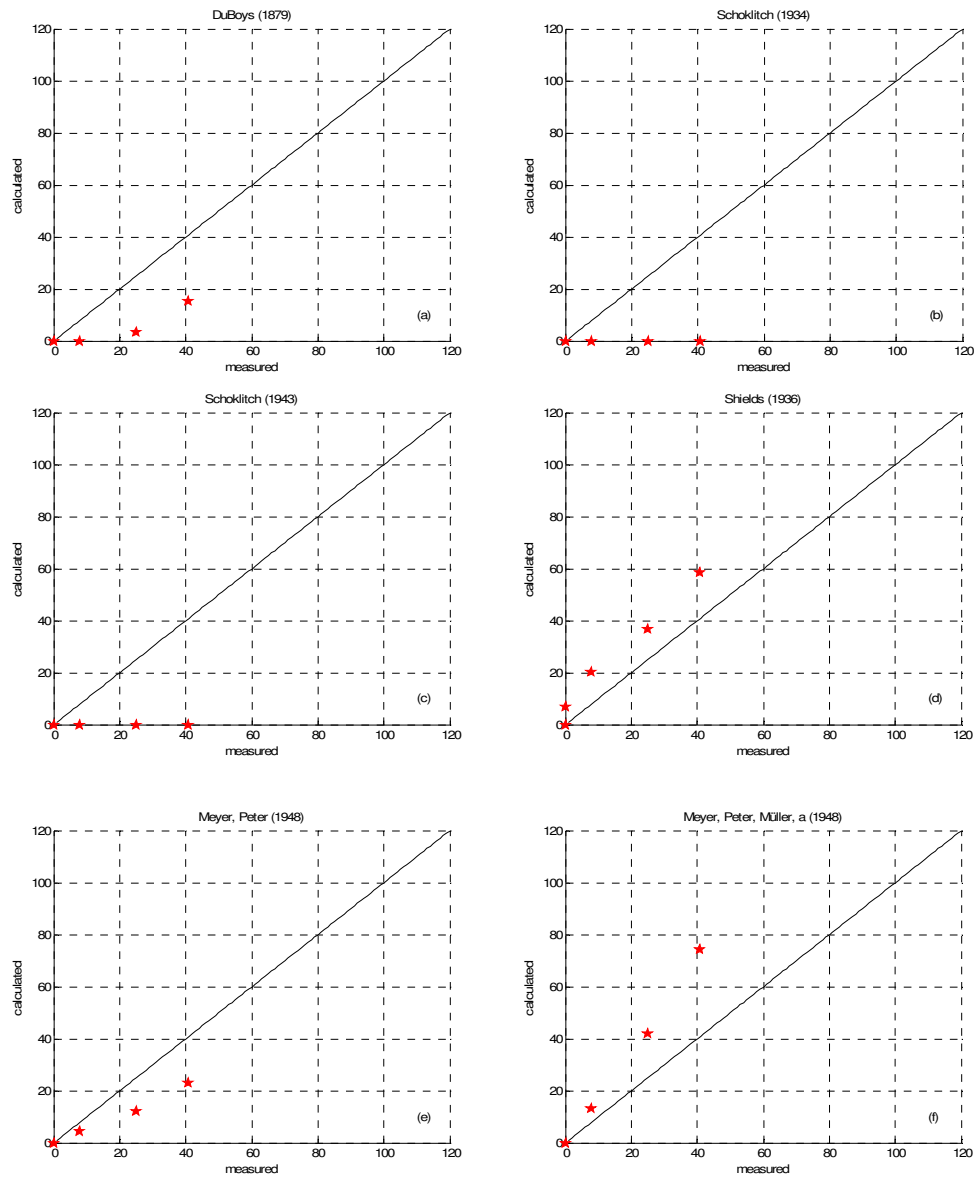


Figure 4.10 Comparison of measured and calculated bed load values (a) Du Boys (1879) Equation (2.11), (b) Schoklitch (1934) Equation (2.12), (b) Schoklitch (1943) Equation (2.13), (d) Shields (1936) Equation (2.16), (e) Meyer, Peter (1948) Equation (2.17), (f) Meyer, Peter, Müller (1948) Equation (2.23)

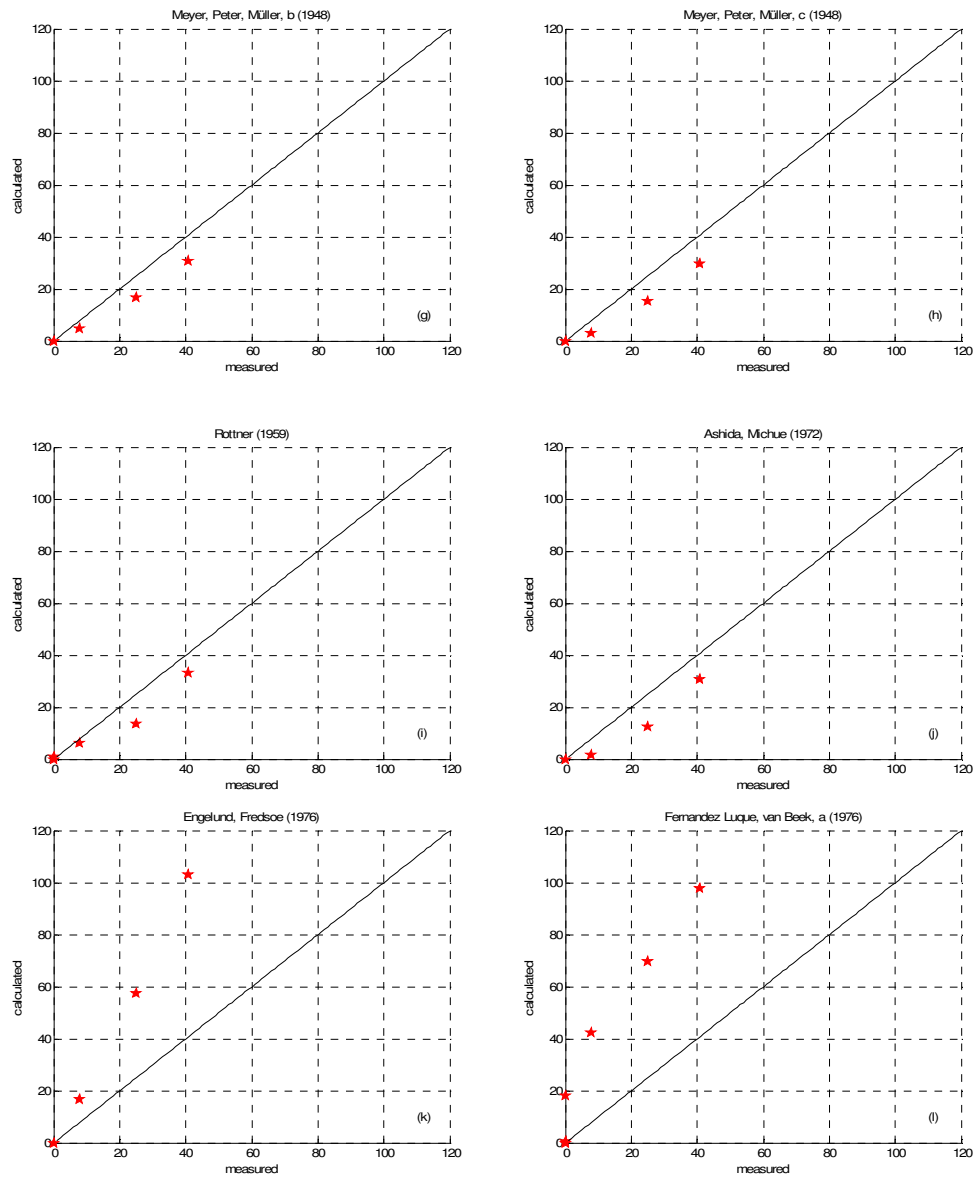


Figure 4.10 Comparison of measured and calculated bed load values (continued) (g) Meyer, Peter, Müller (1948) Equation (2.24), (h) Meyer, Peter, Müller (1948) Equation (2.25), (i) Rottner (1959) Equation (2.26), (j) Ashida, Michue (1972) Equation (2.27), (k) Englund, Fredsoe (1976) Equation (2.28), (l) Fernandez Luque, van Beek (1976) Equation (2.29)

$$\tau_{*cr} = 0.037$$

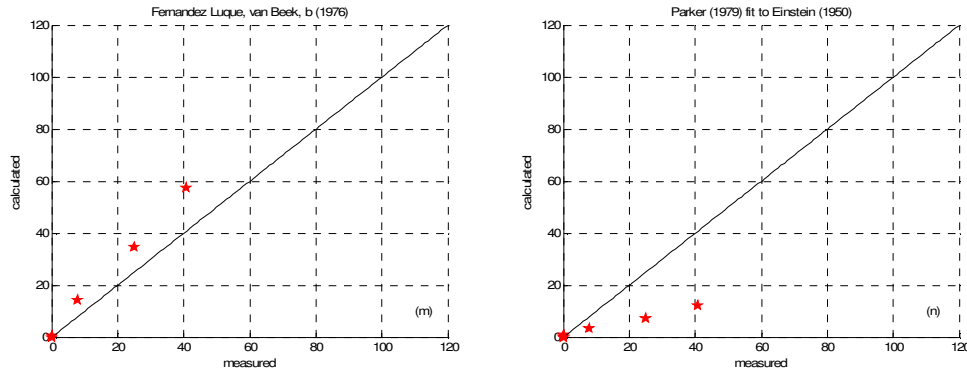


Figure 4.10 Comparison of measured and calculated bed load values (continued)

(m) Fernandez Luque, van Beek (1976) Equation (2.29) $\tau_{*cr} = 0.0455$, (n) Parker (1979) fit to Einstein (1950) Equation (2.30)

The measured bed load values are compared with those calculated from the empirical relations given in the relevant literature. It is found that the measured bed load values are better compatible with those calculated from the expressions given by Meyer, Peter and Müller (1948) and Rottner (1959).

4.3 Bed Forms

Alternate bars are observed along the channel in steady flow conditions performed with the discharge of 68.0 l/s. The maximum vertical difference of the alternate bars is 2.5 cm and the total length, Λ_a is approximately 5m. This is in accord with the well known relation given in equation (4.6) (Da Silva, 2006). In this relation B is the channel width which is 0.8m in our experiments

$$\frac{\Lambda_a}{B} \approx 6 \quad (4.6)$$

The alternate bars observed in this study are given in figure 4.11 and 4.12. The alternate bars observed in Tsukuba University laboratory in Japan and Rhine River, Lichtenstein, Switzerland are given in figure 4.13 and 4.14 respectively.

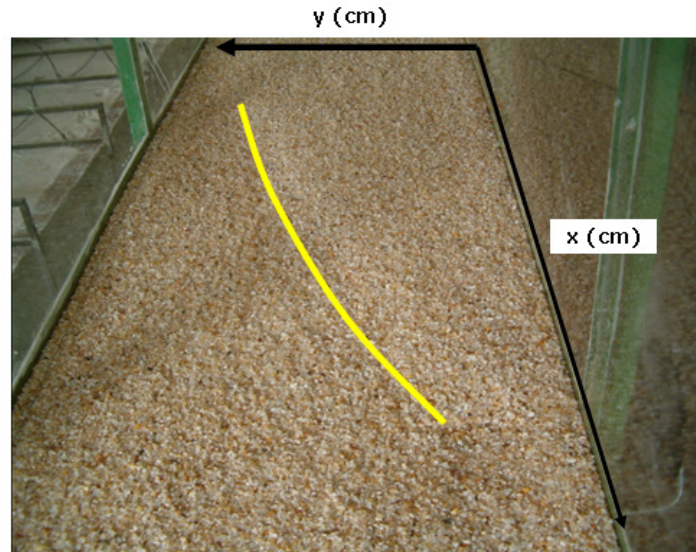


Figure 4.11 The alternate bars

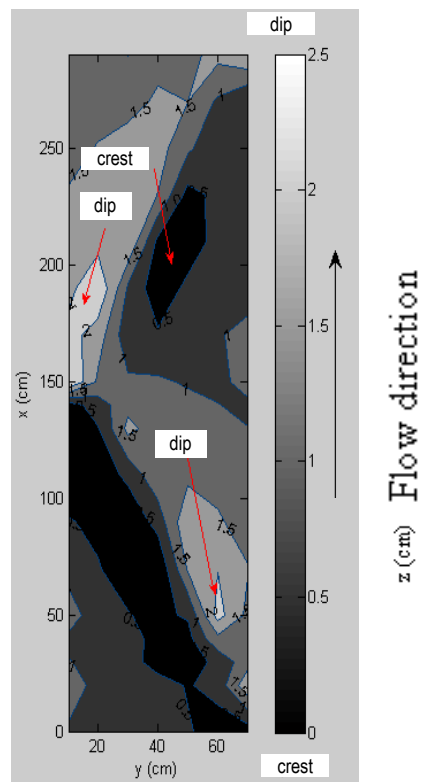


Figure 4.12 The elevations of alternate bars



Figure 4.13 The alternate bars in Tsukuba University laboratory in Japan, (Parker, 2006)



Figure 4.14 The alternate bars in Rhine River, Lichtenstein, Switzerland (Parker, 2006)

CHAPTER FIVE

EXPERIMENTS IN UNSTEADY FLOW CONDITIONS

5.1 Introduction

In open channel with mobile bed, there is a continuous interaction between flowing water and sediment particles. Up to now, several empirical formulae of transported suspended load, bed load and total load have been developed. Most of these formulas estimating bed load, have been proposed for uniform flow and uniform bed conditions. The aim of this study is to examine the effect of unsteadiness on the mechanism of sediment transport under unsteady flow conditions and on the functional relation between dimensionless sediment transport intensity q_* and dimensionless shear stress τ_* , and find the most suitable bed load transport equation for the unsteady flows.

Numerous flume experiments are conducted using different triangular shaped input hydrographs without sediment feeding at upstream. The hydrographs are generated by a regulation of rotational pump speed. The parameters defining the hydrographs are given in figure 5.1. F_b and F_p denote the frequency values corresponding to base discharge and peak discharge, respectively. The characteristics of the hydrographs used in this study are given in Table 5.1

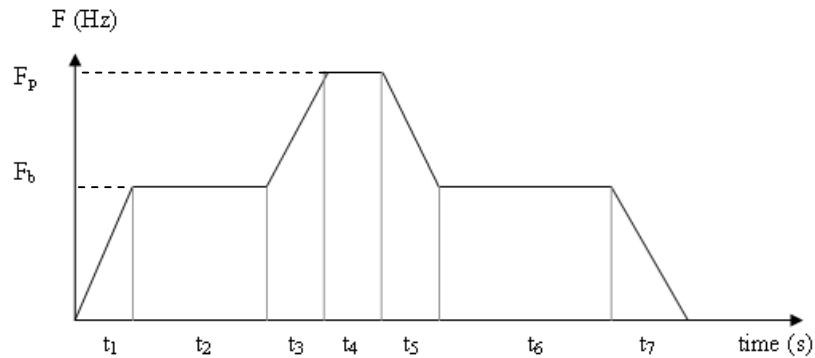


Figure 5.1 The parameters defining the hydrographs

Table 5.1 The properties of the hydrographs used in this study, times are in seconds

Nomination	F _b (Hz)	F _p (Hz)	t ₁	t ₂	t ₃	t ₅	t ₅	t ₆	t ₇
Hid_06	15	40	30	570	15	0	15	1005	9
Hid_04	15	40	30	570	45	0	45	990	18
Hid_05	15	40	30	570	90	0	90	960	45
Hid_07	15	40	30	570	120	0	120	930	54
Hid_20	23	40	30	570	31	0	31	1005	9
Hid_22	23	40	30	570	82	0	82	990	18
Hid_23	15	50	30	570	45	0	45	960	45
Hid_24	15	50	30	570	120	0	120	930	54

The hydrographs used in this study are given in figure 5.2 and the flow parameters for each experiment are given in table 5.2. These parameters are calculated by using the equations 5.1 ~ 5.4 given below.

$$\Delta H = H_p - H_b \quad (5.1)$$

$$\Delta T = T_r + T_f \quad (5.2)$$

$$\Delta Q = Q_p - Q_b \quad (5.3)$$

$$\bar{U}_c = \frac{(\bar{U}_b + \bar{U}_p)}{2} \quad (5.4)$$

where H_b, H_p denote the flow depths corresponding to base and peak flow-rates, T_r, T_f are the duration of the rising and falling limbs of the hydrograph for flow depth, Q_b, Q_p represent the base and peak flow rates, \bar{U}_b, \bar{U}_p are the mean velocities for base flow and peak flow conditions respectively.

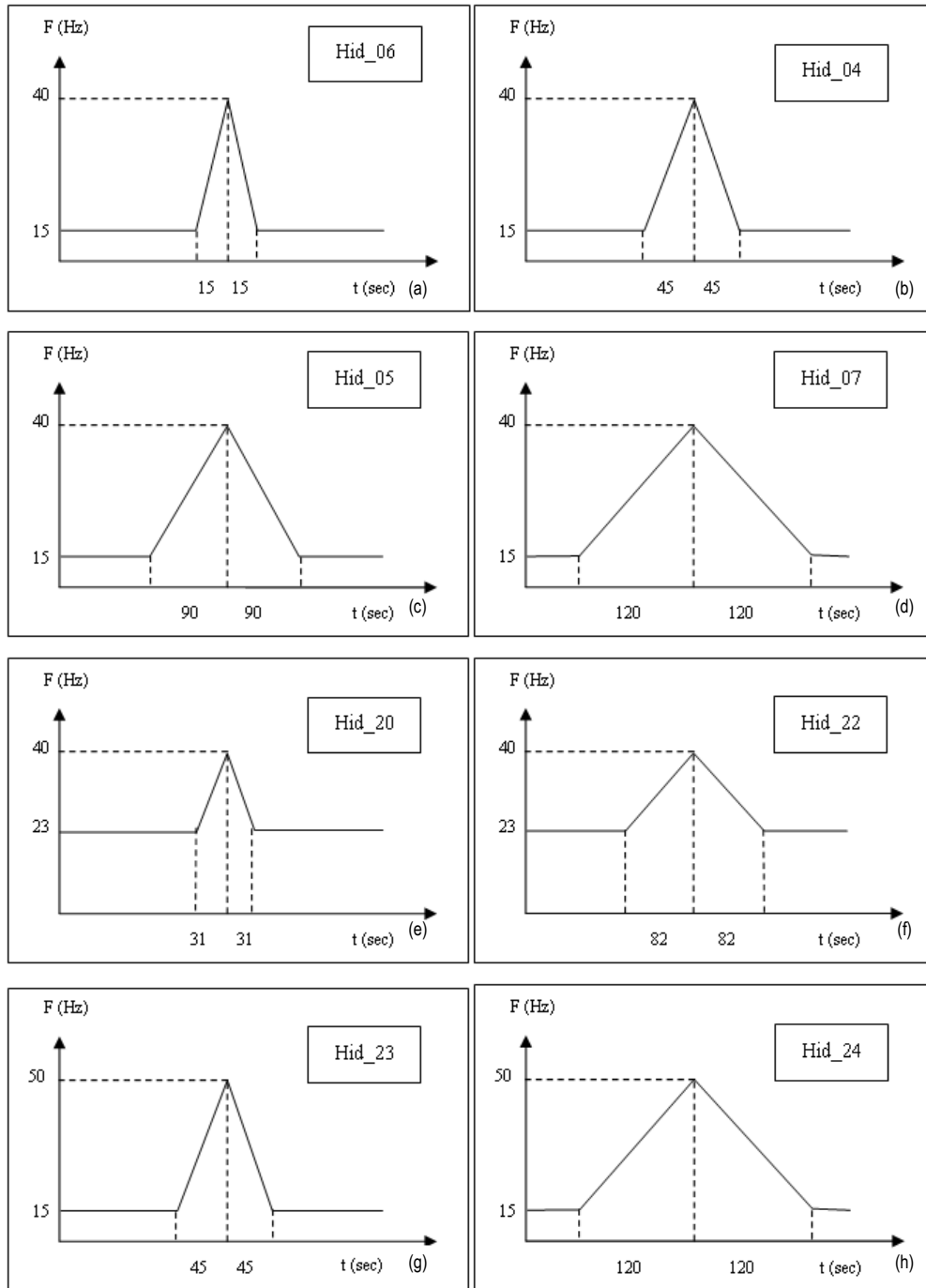


Figure 5.2 The hydrographs used in this study (a) Hid_06, (b) Hid_04, (c) Hid_05, (d) Hid_07, (e) Hid_20, (f) Hid_22, (g) Hid_23, (h) Hid_24

Table 5.2. The flow parameters of the hydrographs generated

Parameter	Exp1	Exp2	Exp3	Exp4	Exp5	Exp6	Exp7	Exp8
H_b (cm)	4.0	4.0	4.0	4.0	6.7	6.7	4.0	4.0
H_p (cm)	8.8	10.2	10.4	10.4	10.1	10.4	11.9	12.0
ΔH (cm)	4.8	6.2	6.4	6.4	3.4	3.7	7.9	8.0
T_r (s)	14	46	90	119	34	82	44	118
T_f (s)	53	104	118	148	65	105	92	152
ΔT (s)	67	150	208	267	99	187	136	270
Q_b (l/s)	12.0	12.0	12.0	12.0	30.3	30.3	12.0	12.0
Q_p (l/s)	53.5	63.0	66.4	68.3	63.7	68.7	85.2	86.3
ΔQ (l/s)	41.5	51.0	54.4	56.3	33.4	38.4	73.2	74.3
\bar{U}_b (cm/s)	37.5	37.5	37.5	37.5	56.5	56.5	37.5	37.5
\bar{U}_p (cm/s)	76.8	77.7	80.2	82.5	78.9	82.6	89.9	89.5
\bar{U}_c (cm/s)	57.2	57.6	58.9	60.0	67.7	69.6	63.7	63.5

5.2 Flow Depth

The flow depth variation is recorded by the camera at various sections of the flume and given in figure 5.3 to 5.10. The flow depth variation at $x=11\text{m}$, obtained by taking into consideration all hydrographs, is given in figure 5.11.

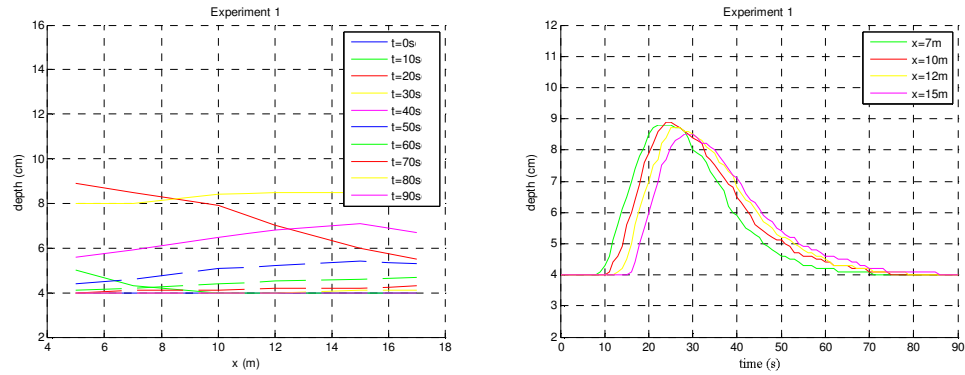


Figure 5.3 The flow depth variation (a) within the flume and (b) wrt time for the hydrograph experiment 1

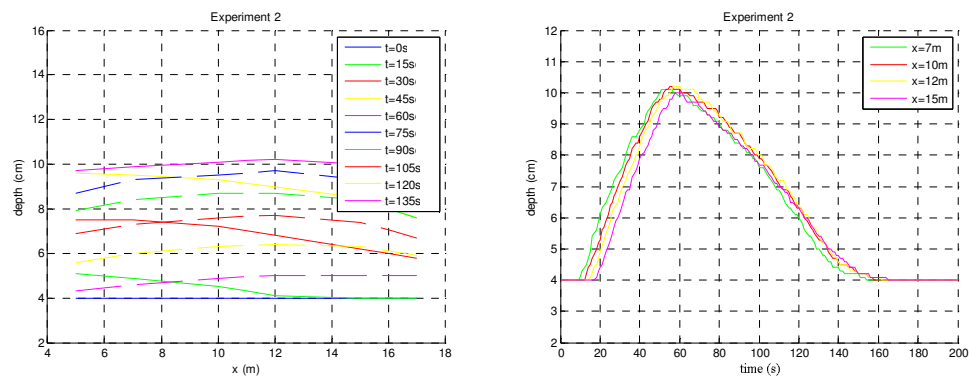


Figure 5.4 The flow depth variation (a) within the flume and (b) wrt time for the hydrograph experiment 2

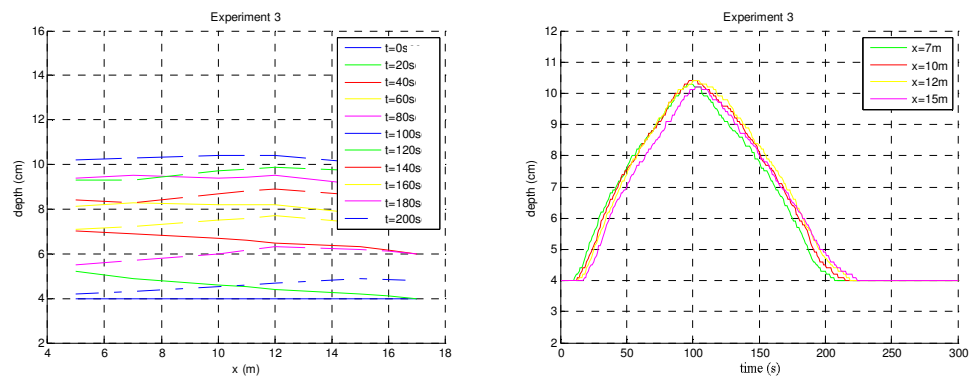


Figure 5.5 The flow depth variation (a) within the flume and (b) wrt time for the hydrograph experiment 3

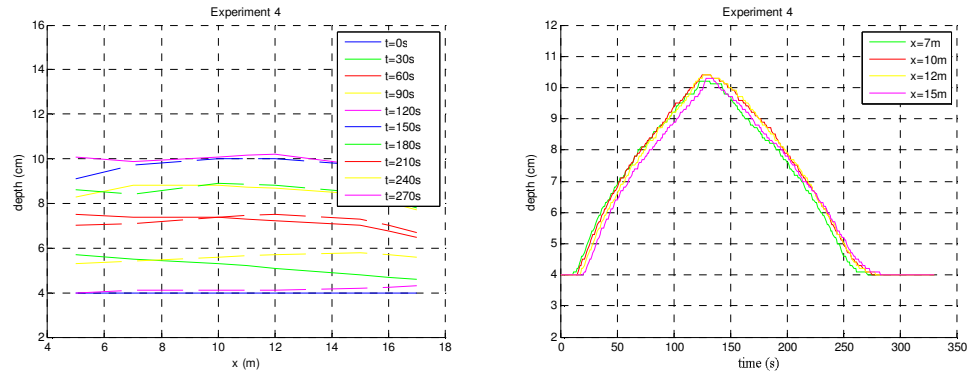


Figure 5.6 The flow depth variation (a) within the flume and (b) wrt time for the hydrograph experiment 4

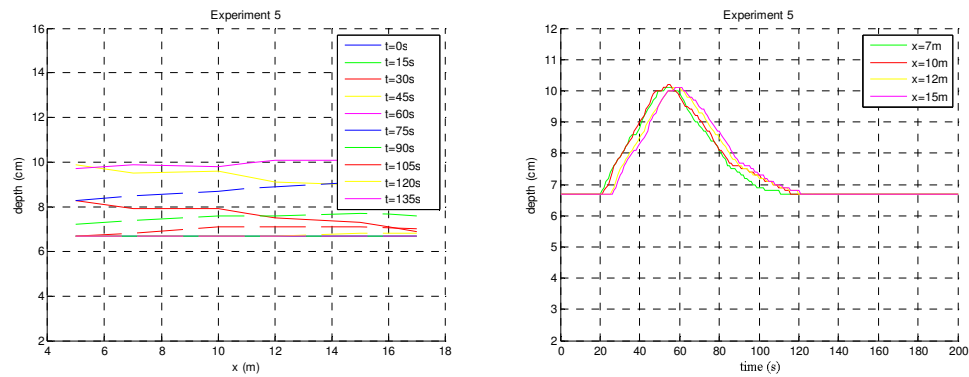


Figure 5.7 The flow depth variation (a) within the flume and (b) wrt time for the hydrograph experiment 5

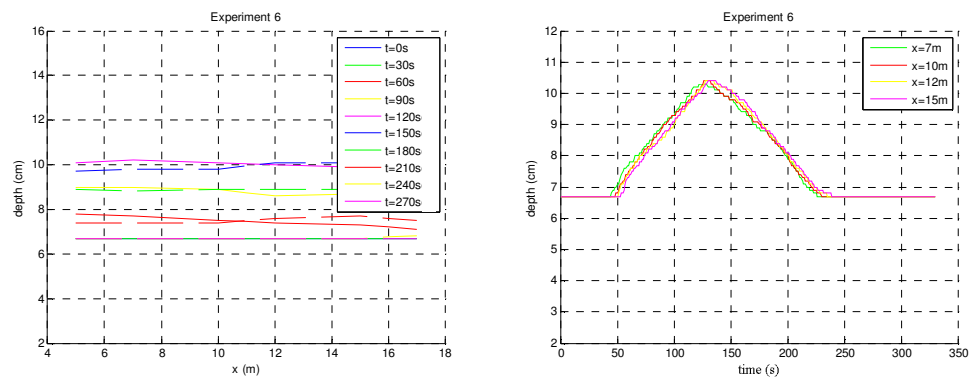


Figure 5.8 The flow depth variation (a) within the flume and (b) wrt time for the hydrograph experiment 6

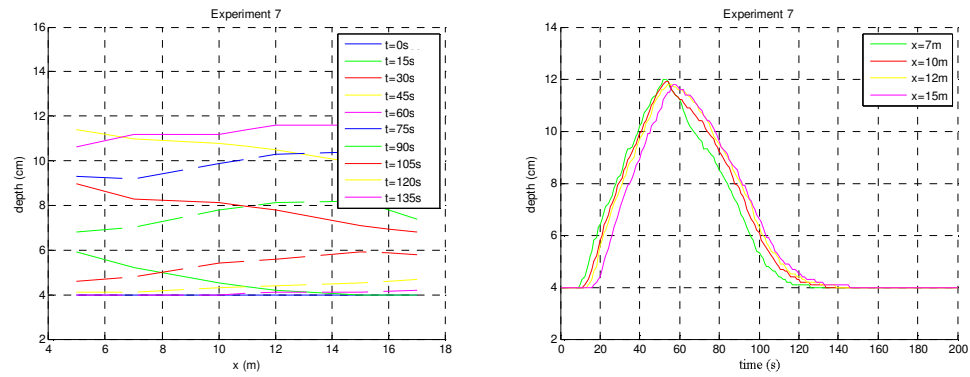


Figure 5.9 The flow depth variation (a) within the flume and (b) wrt time for the hydrograph experiment 7

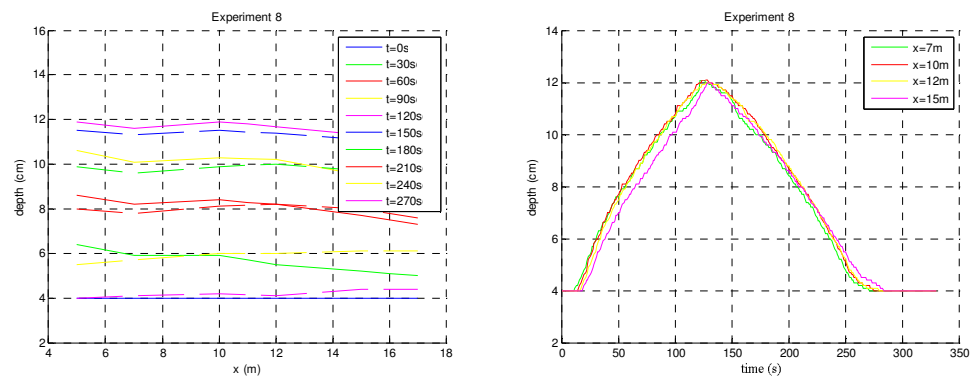


Figure 5.10 The flow depth variation (a) within the flume and (b) wrt time for the hydrograph experiment 8

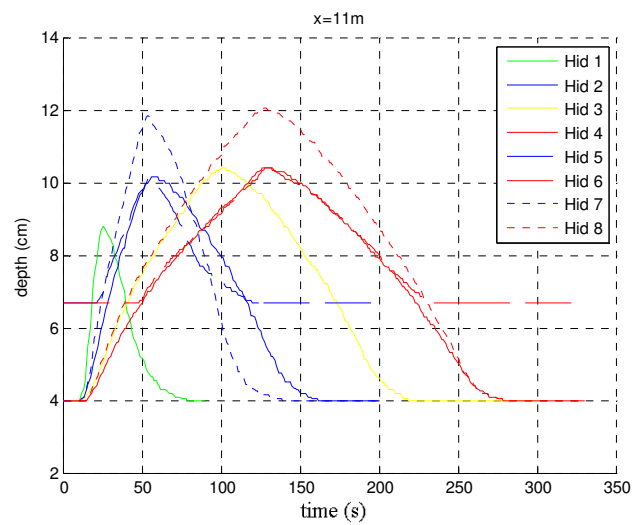


Figure 5.11 Flow depth variations at $x=11m$ corresponding to different hydrographs

5.3 Data Processing Approaches

The time varying velocity data obtained during experiments are analyzed by decomposing the instantaneous velocity values into time-varying mean value and a fluctuation. In the case of velocity measurements in steady flows, the time mean velocity, \bar{u} can be obtained easily by taking the average of the instantaneous velocity, u . In such a stationary process, it can be said that, \bar{u} is not a function of time. In the case of unsteady flows, there are several methods to obtain the time-varying mean velocity from the velocity records, such as the ensemble average, Fast Fourier Transform (FFT), smoothing algorithm, wavelet and the empirical mode decomposition (EMD) methods (Lin, 2005). Each signal analysis technique has advantages as well as disadvantages. The method to be used in a particular application must be carefully selected by taking account the nature of signals being studied (Qu, 2003).

The ensemble-averaged method is used to calculate the mean parameters for unsteady flows. Many experiments need to be repeated in order to apply this method. Most applications are performed in oscillatory flows (Qu, 2003). Qu (2003) repeated one of the experiments 10 times in order to apply the ensemble-averaged method in the area of signal treatment.

Fast Fourier Transform consists of breaking up a signal into sine waves of various frequencies. But the Fourier analysis has a serious drawback, namely when transforming to the frequency domain, time information is lost. When looking at a Fourier transform of a signal, it is impossible to tell when a particular event took place (Matlab, 2007c).

Smoothing algorithm takes the mean of the n previous data to obtain the value of $n+1^{\text{th}}$ value. This method was used by some researchers (Tu,1991 and Nezu et al, 1997). In Matlab, the command `Z = SMOOTH(X,Y,SPAN,METHOD)` smoothes data Y with specified `METHOD`. The “rloess”, “rlowess” or “move” smoothing

algorithms are used for the velocity data. “rlowess” is a robust version of local regression model that assigns lower weight to outliers in the regression using a 1st degree polynomial model (linear fit) while “rloess” is for quadratic fit. The method assigns zero weight to data outside six mean absolute deviations. $Z = \text{SMOOTH}(X, Y, 0.3, \text{'rloess'})$ uses the robust lowess method where span is 30% of the data. The algorithm takes number of elements of X, multiplies it by 0.30 and rounds it to the nearest integer. The span depends on the type of the hydrograph. “move” smoothes data Y using SPAN as the number of points to compute each element of Z (Matlab, 2007a).

A wavelet is a waveform of effectively limited duration that has an average value of zero. Similar to Fourier analysis, wavelet analysis is the breaking up of a signal into shifted and scaled versions of the original (or mother) wavelet. Several families of wavelet are included in the Matlab wavelet toolbox (Matlab, 2007c).

A new data processing method referred to as empirical mode decomposition (EMD) is recently developed to analyze the non-stationary time-series data (Huang and Shen, 2005), (Lin, 2005). To accommodate the inherent non-linearity and non-stationary of many natural time series, EMD provides an adaptive and efficient method (Rao and Hsu, 2008).

Güney et.al (2009) compared the methods for fixed bed for unsteady flows and found that the smoothing algorithm gives the best results.

5.4 Mean Point Velocity and Shear Velocity, Mean Cross-sectional Velocity, and Flowrate

In this study UVP transducers are used in a manner that the level of the transducer is manually operated keeping the tip of the transducer touching the surface of the water. The shear velocity, cross-sectional velocity and flow rate are determined from the UVP data.

The longitudinal velocity in the inner region ($z/h < 0.2$, z being the vertical distance from the bottom), can be expressed by the universal logarithmic law.

$$\frac{u}{u_*} = \frac{1}{\kappa} \ln \left(\frac{z + z_0}{k_s} \right) + B_r \quad (5.5)$$

where u_* =shear velocity from log-law, κ = von Karman constant (=0.40), k_s is the equivalent sand roughness for the rough bed and is taken $2.5 D_{50}=1.2$ cm, B_r is the integration constant for rough beds, z_0 is the reference level where the velocity is zero according to log-law and is equal to $k_s/30=0.04$ cm.

The curve fitting technique is applied by using 30% of the raw data in order to determine the values of u_* and B_r , in the inner region. Consequently the values of u_* are obtained.

The velocity profile deviates from the logarithmic distribution in the outer region ($z/h > 0.2$), where the Cole's Wake Law, given in equation (5.6), is valid:

$$\frac{u}{u_*} = \frac{1}{\kappa} \ln \left(\frac{z + z_0}{k_s} \right) + B_r + \frac{2\Pi}{\kappa} \sin^2 \left(\frac{\pi}{2} \frac{z + z_0}{h} \right) \quad (5.6)$$

Knowing the bed level and by using the values u_* and taking $B_r=8.5$, the parameter Π is calculated from the Cole's Wake Law (Nezu, 2005). The Cole's Wake Law is used to extrapolate the velocity profile towards the water surface provided that the u_* and Π are known.

The "rflowess" smoothing algorithm based on linear fitting in Matlab is used to evaluate the time varying mean velocity (Matlab, 2007c). The values measured during the 1st experiment and smoothed velocity data which belongs to the

instantaneous and the mean point velocity at points ($z=5.1\text{cm}$; $x=11\text{m}$) and ($z=3.7\text{cm}$; $x=16\text{m}$) are given in figure 5.12.a and 5.12.b, respectively.

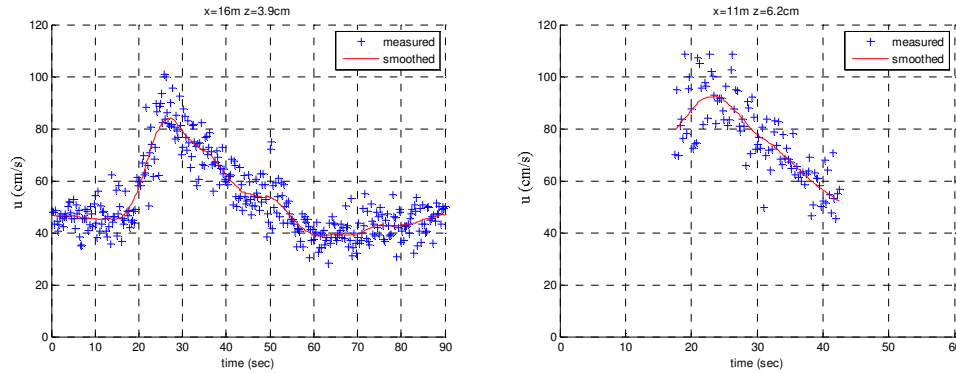


Figure 5.12 Instantaneous and mean point velocity at (a) $z=3.9\text{cm}$ at $x=16\text{m}$, (b) $z=6.2\text{cm}$ at $x=11\text{m}$ for experiment 1

The measured raw data and the final smoothed data at $x=11\text{m}$ in steady case part and at $t=32.5\text{ s}$ are given in figure 5.13.a and 5.13.b for experiment 1 (Exp 1 in Table 5.2).

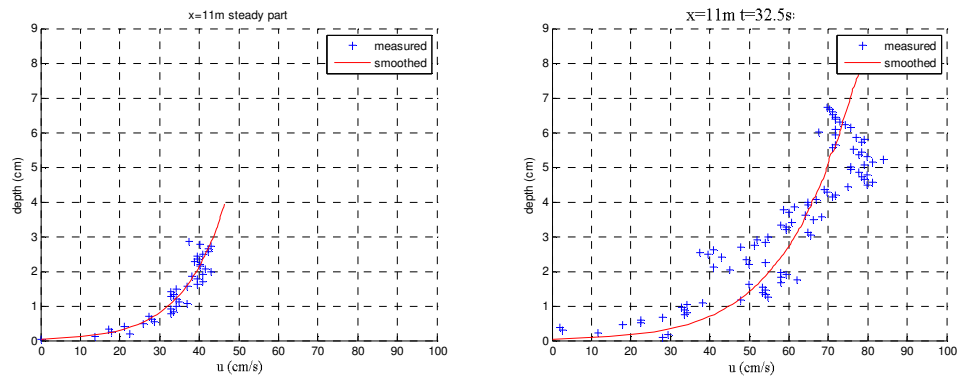


Figure 5.13 Measured and smoothed velocity profiles at $x=11\text{m}$ for experiment 1 (a) steady part case (b) $t=32.5\text{ s}$

The various velocity profiles related to rising and falling limbs for experiment 4 are given in figure 5.14.a and 5.14.b, respectively.

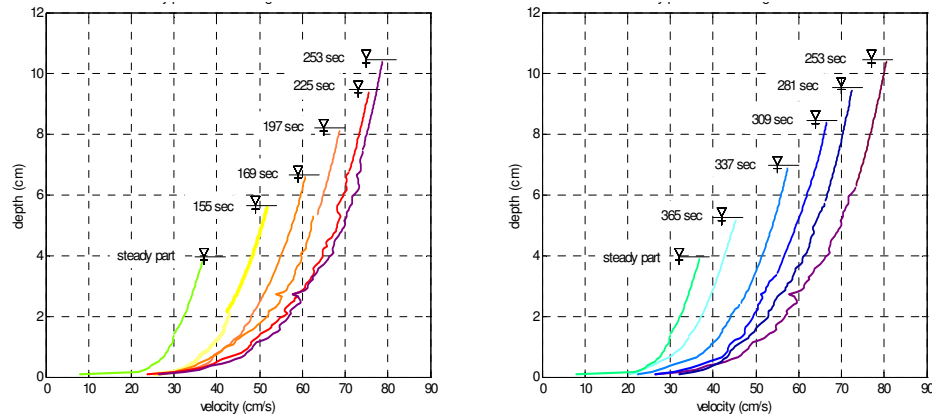


Figure 5.14 The velocity profiles at $x=10\text{m}$ for experiment 4 (a) rising limb and (b) falling limb

For steady uniform flow, the following equation (corresponding to Eq 4.1) is used to calculate the shear velocity, denoted by u_{*H} .

$$u_* = \sqrt{gHS_0} \quad (5.7)$$

The time variations of shear velocity denoted by u_{*LOG} (equation 5.5) and those of u_{*H} (equation 5.7) for all experiments are given in figure 5.15.

The unsteadiness of flow is parameterized by different researchers as follows:

$$\Omega = \frac{1}{B} \frac{\Delta Q}{u_{*b}^2 \Delta T} \quad (5.8)$$

$$\alpha = \frac{1}{U_c} \frac{\Delta H}{T_r} \quad (5.9)$$

Lee et.al. (2004) proposed an unsteadiness parameter P which is expressed as,

$$P = \frac{H_p - H_b}{\Delta T u_{*b}} \quad (5.10)$$

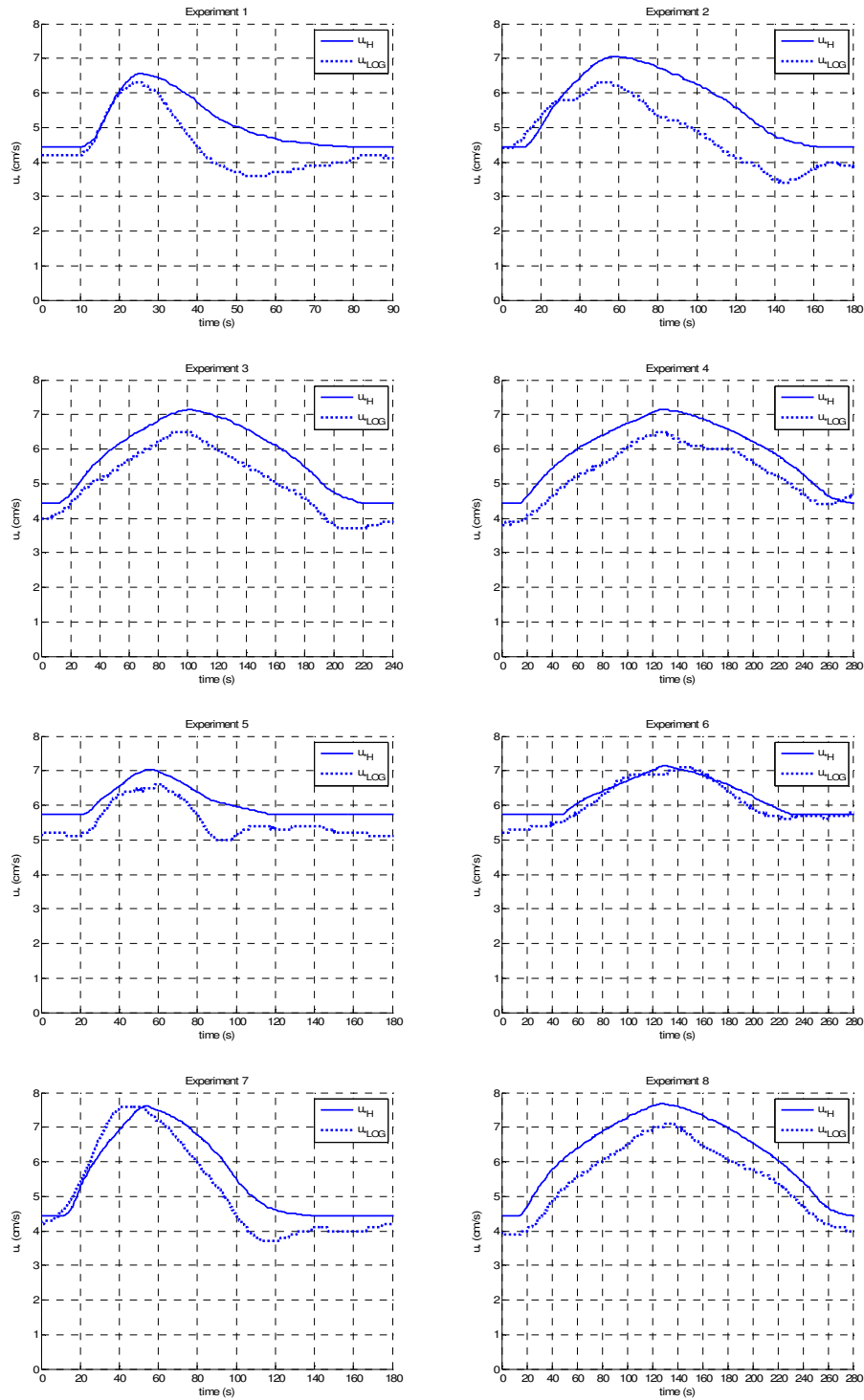


Figure 5.15 The time variation of u_{*LOG} and u_{*H} values for (a) experiment 1, (b) experiment 2, (c) experiment 3, (d) experiment 4, (e) experiment 5, (f) experiment 6, (g) experiment 7, (h) experiment 8

De Sutter and Verhoeven (2001) discussed the effectiveness of unsteadiness parameter and whether this parameter should be considered for both the rising and falling limbs. They stated that only the duration of the rising limb should be considered in the unsteadiness of the hydrograph and proposed the following parameter instead.

$$P_{\text{mod}} = \frac{H_p - H_b}{T_r} \frac{u_{*p}^2 - u_{*b}^2}{\bar{U}_c u_{*b}^2} \quad (5.11)$$

$$\bar{U}_c = 0.5(\bar{U}_b + \bar{U}_p) \quad (5.12)$$

where, $\Delta H = H_p - H_b$, H_b, H_p denote the base and peak flow depths, $\Delta T = T_r + T_f$, T_r, T_f are the duration of the rising and falling limbs of the hydrograph for flow depth, $\Delta Q = Q_p - Q_b$, Q_b, Q_p represent the base and peak flow rates, \bar{U}_b, \bar{U}_p are the mean velocities for base flow and peak flow conditions respectively, B is the flume width, u_{*b} is the shear velocity of the base flow, u_{*p} is the maximum shear velocity.

The various flow parameters together with unsteadiness parameters determined in the manner explained above, and the total amount of sediments collected in the baskets, W_T , are given in Table 5.3 for $x=11\text{m}$.

Table 5.3. The unsteadiness parameters of the hydrographs generated

Parameter	Exp1	Exp2	Exp3	Exp4	Exp5	Exp6	Exp7	Exp8
u_{*b} (cm/s)	4.4	4.4	4.4	4.4	5.7	5.7	4.4	4.4
u_{*p} (cm/s)	6.6	7.1	7.1	7.1	7.0	7.1	7.6	7.7
Ω	0.40	0.22	0.17	0.14	0.13	0.08	0.35	0.18
α	0.0060	0.0023	0.0012	0.0009	0.0015	0.0006	0.0028	0.0011
P	0.0163	0.0094	0.0070	0.0054	0.0060	0.0035	0.0132	0.0067
P_{mod}	0.0075	0.0038	0.0019	0.0014	0.0008	0.0004	0.0056	0.0022
W_T (kg)	0.75	2.88	3.95	5.25	2.00	4.34	4.29	9.60

5.5 Bed Load from Sediment Baskets

The bed load coming from the flume is collected in the sediment baskets located at the downstream part of the flume. Each basket collected bed load for 15 s, and replaced with an empty new one. After a time required for the sediments to be dried, the bed material is weighed and its uniformity is checked by sieve analysis. The hydrographs are repeated 10 times to have an average value. The average values of the time variation of the bed load are given in figure 5.16.

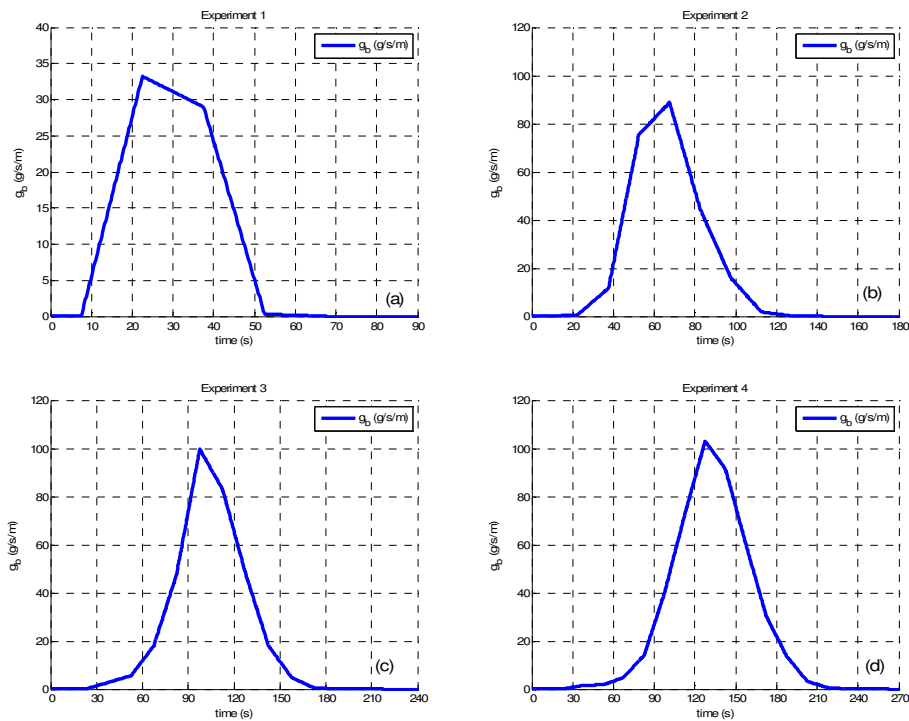


Figure 5.16 The time variation of average bed load for (a) experiment 1, (b) experiment 2, (c) experiment 3, (d) experiment 4

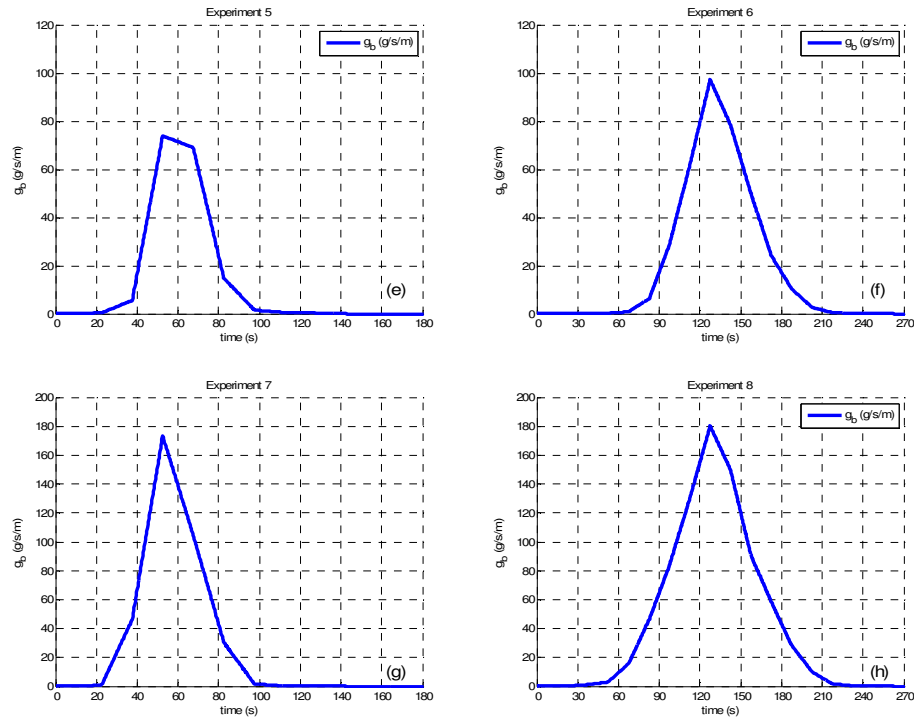


Figure 5.16 The time variation of average bed load (continued) for (e) experiment 5, (f) experiment 6, (g) experiment 7, (h) experiment 8

The flow rate Q is calculated by using the flow depth and cross-sectional mean velocity V data. The variations of H , V and Q at 11 m are illustrated in figure 5.17 – 5.24. There is not a distinguishable time lag between these parameters. But the sequence is V , H and Q .

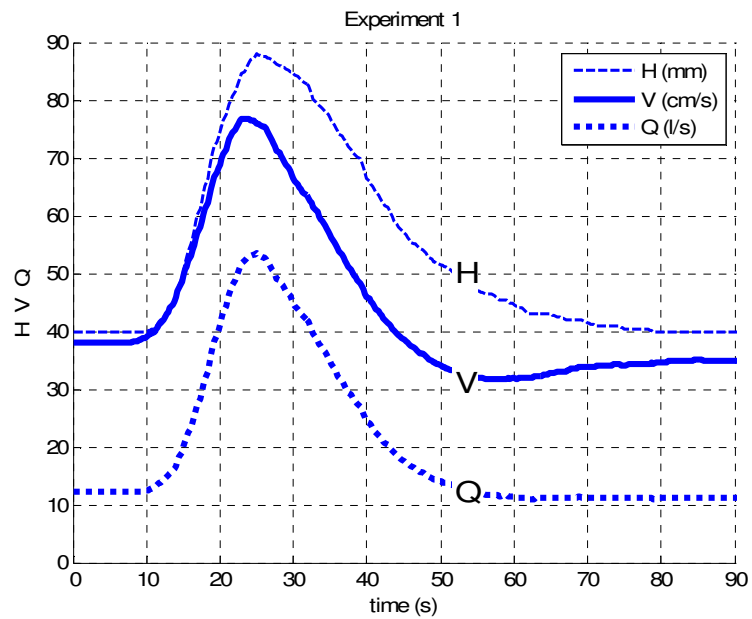


Figure 5.17 The variation of mean cross sectional velocity, flow depth and flow rate for experiment 1

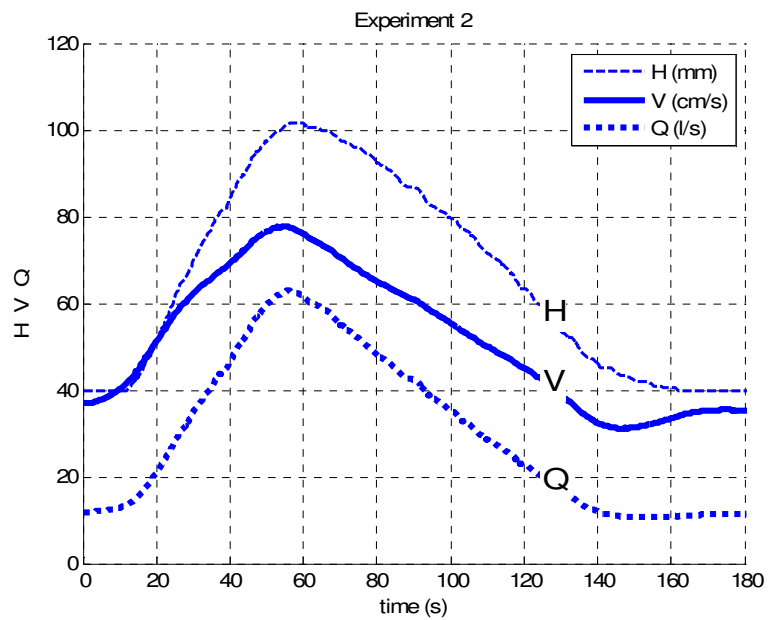


Figure 5.18 The variation of mean cross sectional velocity, flow depth and flow rate for experiment 2

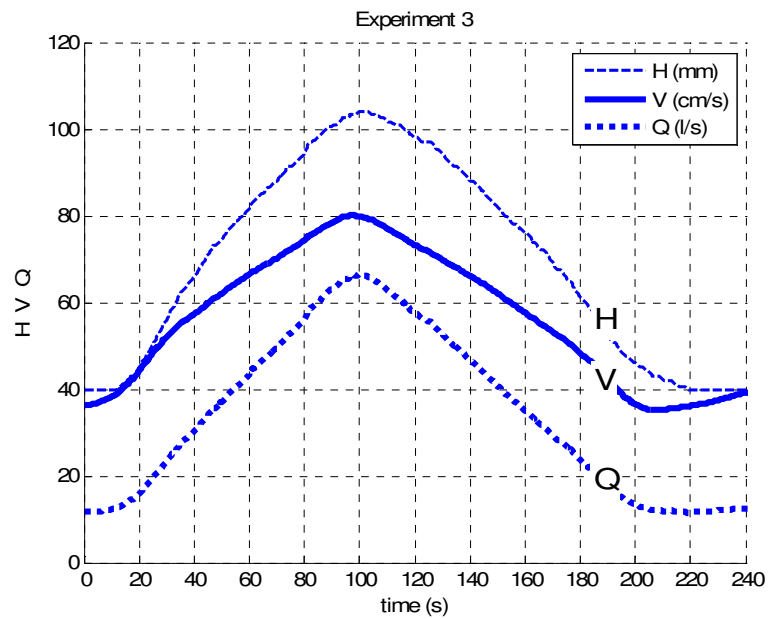


Figure 5.19 The variation of mean cross sectional velocity, flow depth and flow rate for experiment 3

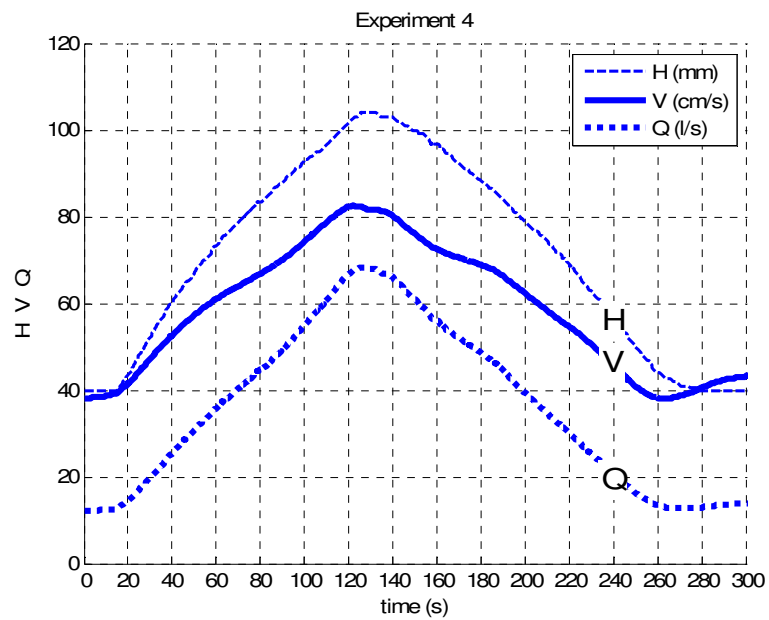


Figure 5.20 The variation of mean cross sectional velocity, flow depth and flow rate for experiment 4

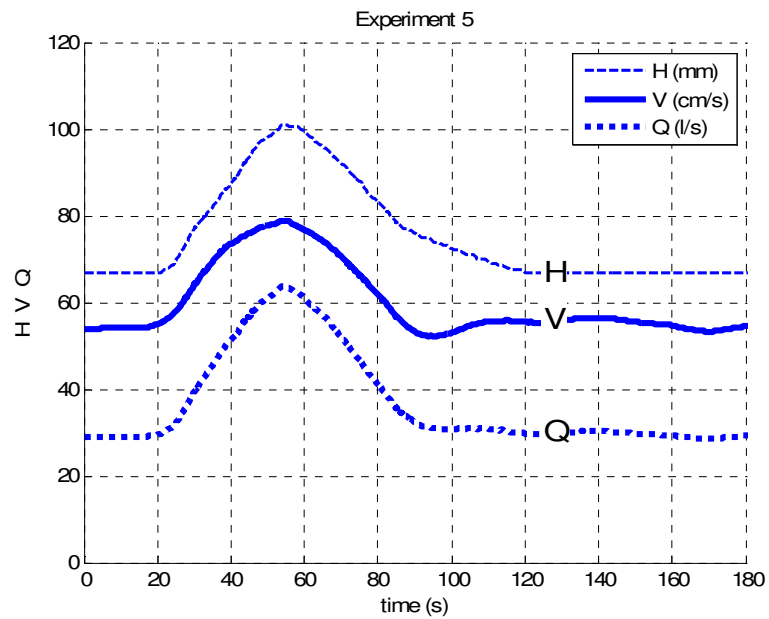


Figure 5.21 The variation of mean cross sectional velocity, flow depth and flow rate for experiment 5

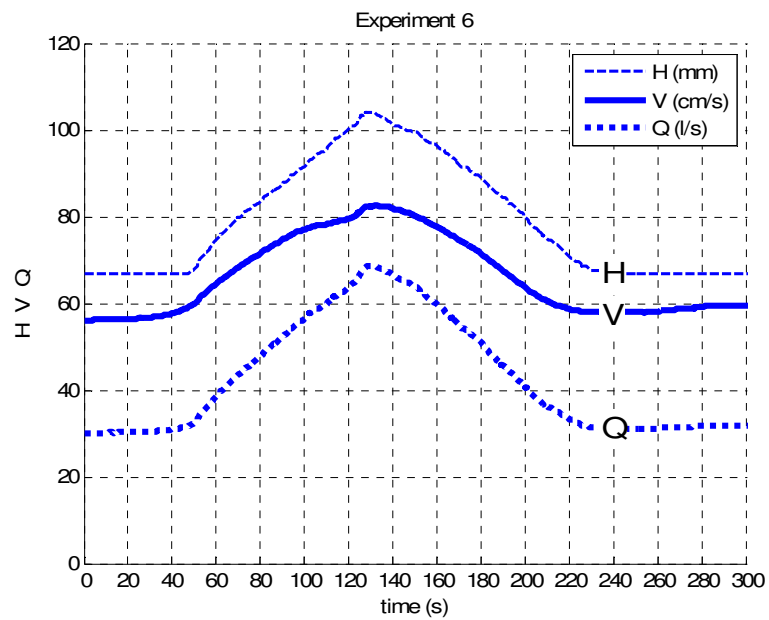


Figure 5.22 The variation of mean cross sectional velocity, flow depth and flow rate for experiment 6

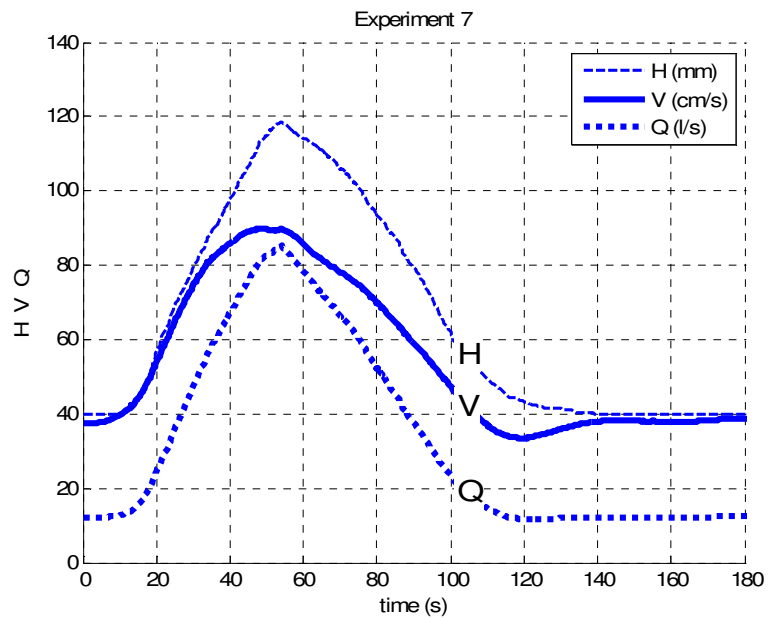


Figure 5.23 The variation of mean cross sectional velocity, flow depth and flow rate for experiment 7

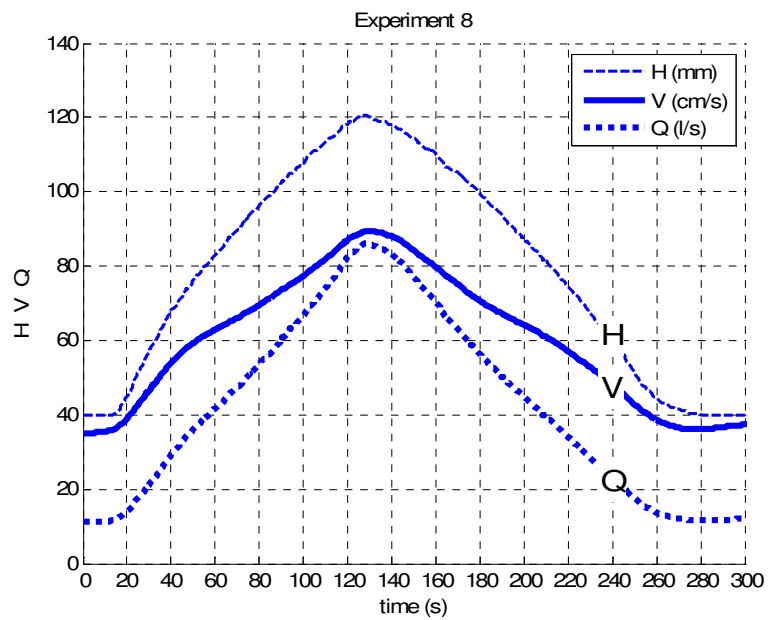


Figure 5.24 The variation of mean cross sectional velocity, flow depth and flow rate for experiment 8

Figure 5.25 and figure 5.26 represent the relation $H = f(Q)$ obtained from the second and fourth experiments, respectively.

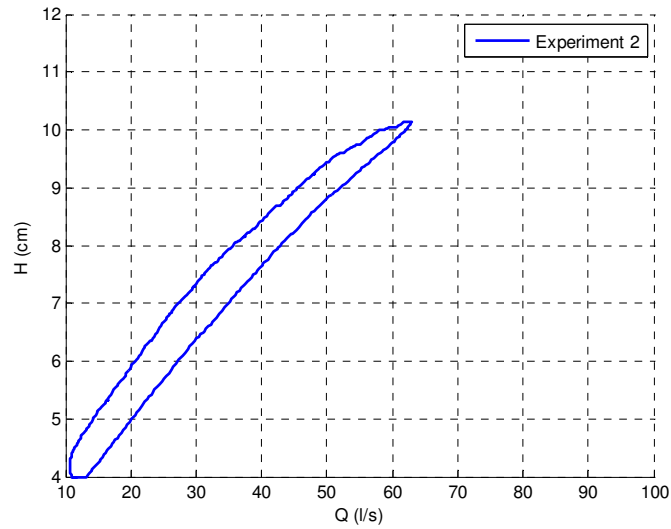


Figure 5.25 The relation $H=f(Q)$ for experiment 2

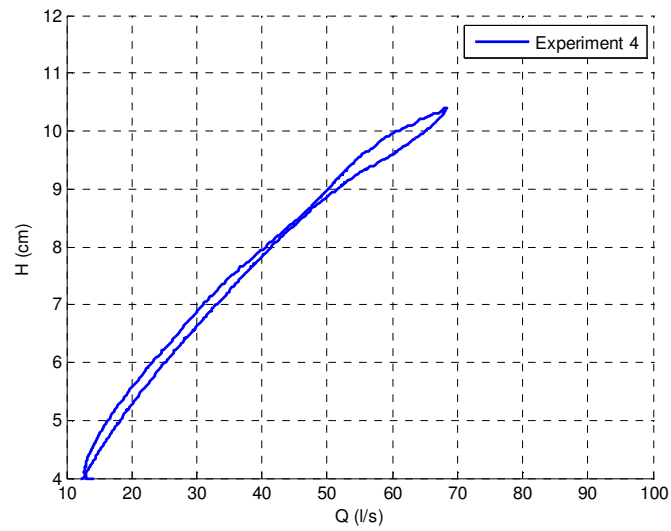


Figure 5.26 The relation $H=f(Q)$ for experiment 4

The bed load formulas given in chapter two are applied to the unsteady flow cases to determine the most appropriate formula. The error is calculated for each formula and the best two formulas in addition to the bed load obtained from sediment baskets are depicted in the figures 5.27. The formulas mentioned in the figures are summarized below. In these formulas $\gamma_s = 2.65 \times 10^{-6} \text{ gr/m}^3$, $\Delta = 1.65$, $g = 9.81 \text{ m/s}^2$, $D_{50} = 0.0048 \text{ m}$ and g_b is in gr/s/m .

Fernandez Luque and Van Beek Equation (1976)

$$g_b = 5.7 \gamma_s \sqrt{\Delta g D_{50}^3} \left(\frac{HS_0}{\Delta D_{50}} - 0.037 \right)^{3/2} \quad (5.13)$$

Engelund and Fredsoe Equation (1976)

$$g_b = 18.74 \gamma_s \sqrt{\Delta g D_{50}^3} \left(\frac{HS_0}{\Delta D_{50}} - 0.05 \right) \left(\sqrt{\frac{HS_0}{\Delta D_{50}}} - 0.7 \sqrt{0.05} \right) \quad (5.14)$$

For the experiment 1 and 2 the most suitable formula is found to be the Fernandez Luque and Van Beek (1976) formula given in equation 5.13, but for the rest that of Engelund and Fredsoe (1976), given in equation 5.14 is the most appropriate one. The measured and calculated bed load for the most suitable formula and the proposed formula in equation (4.6) are given in figure 5.28.

The relation between the dimensionless shear stress τ_* and dimensionless bed load q_* are given in figure 5.29.

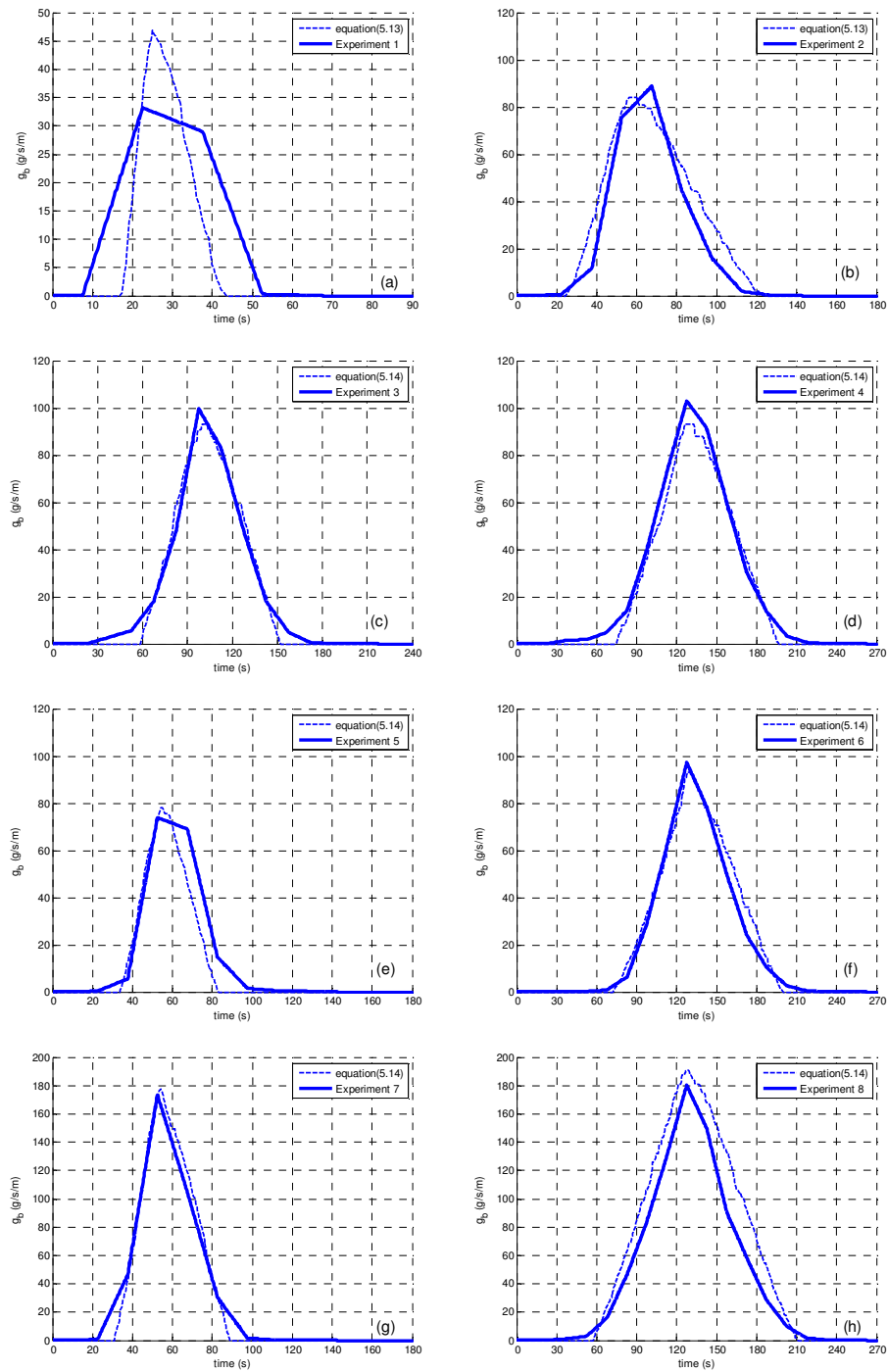


Figure 5.27 The bed load obtained from sediment baskets and calculated from formulas (a) experiment 1, (b) experiment 2, (c) experiment 3, (d) experiment 4, (e) experiment 5, (f) experiment 6, (g) experiment 7, (h) experiment 8

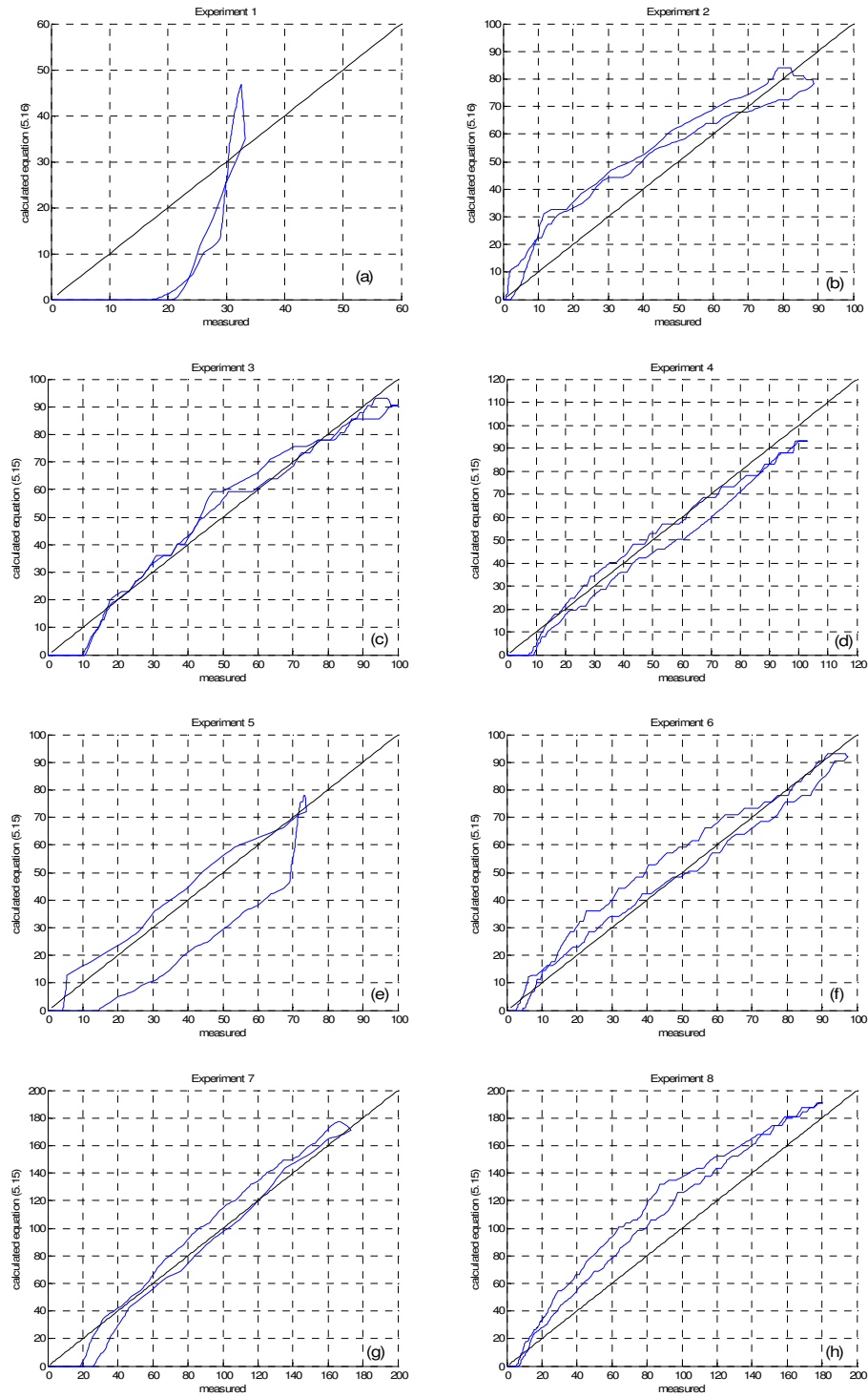


Figure 5.28 The measured and calculated bed load (a) experiment 1, (b) experiment 2, (c) experiment 3, (d) experiment 4, (e) experiment 5, (f) experiment 6, (g) experiment 7, (h) experiment 8

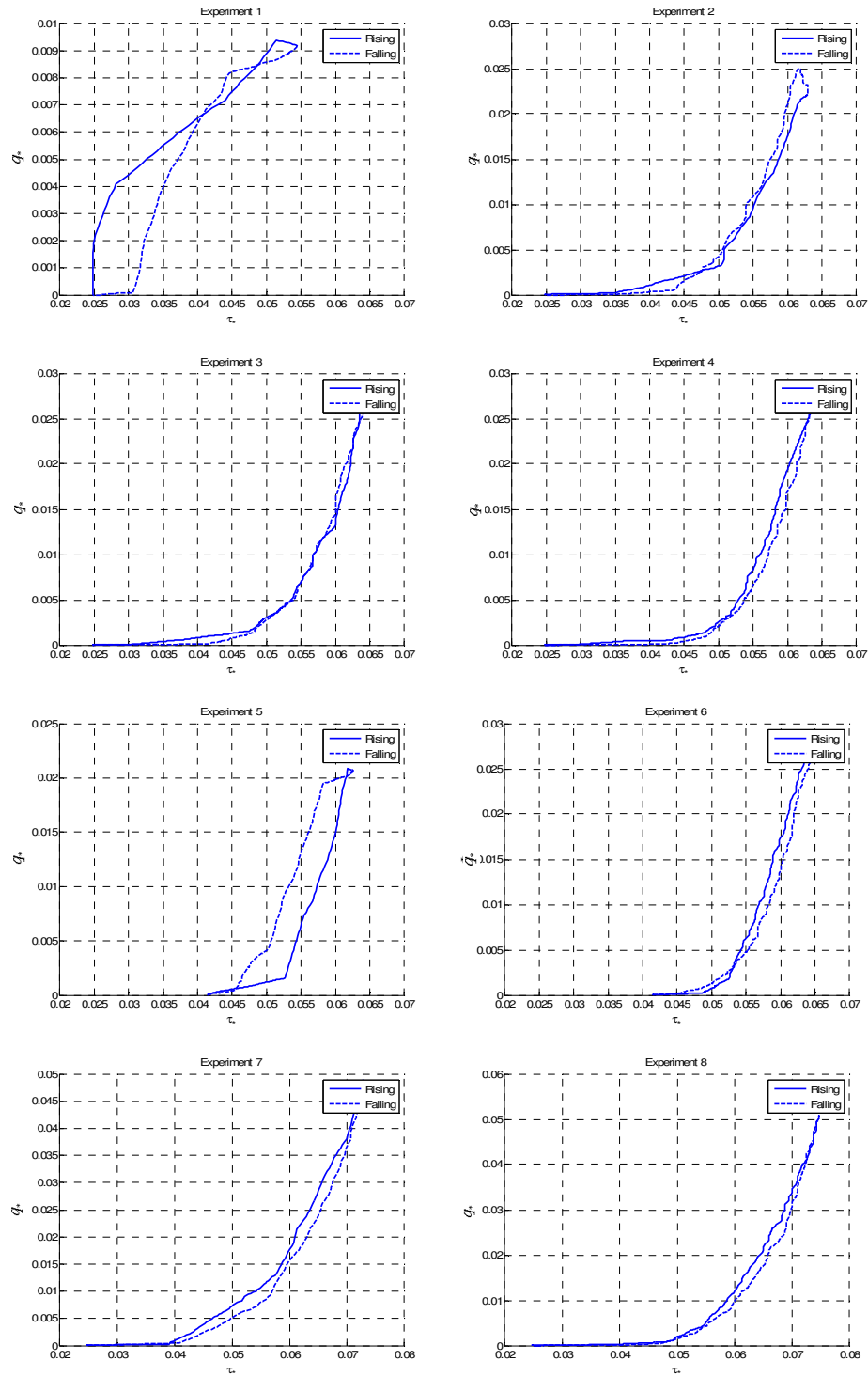


Figure 5.29 The relation between the dimensionless shear stress τ_* and dimensionless bed load q_* (a) experiment 1, (b) experiment 2, (c) experiment 3, (d) experiment 4, (e) experiment 5, (f) experiment 6, (g) experiment 7, (h) experiment 8

5.6 Bed Load from Image Processing Technique

The bed load obtained from experiment 1 is investigated by image processing technique. While the bed load is determined by the sediment baskets, a camera is used at $x=11\text{m}$ and $x=16\text{ m}$ to visualize and calculate the amount of the sediment in motion.

Image processing technique is a promising technique to investigate the bed load movement by many researchers (Papanicolaou et. al., 1999, Jamieson et. al., 2008, Malavasi et.al., 2006, Keshavarzy and Ball, (1999)).

Totally there exist 600 frames and 631 frames which have a total duration of approximately 25 s at both $x=11\text{m}$ and $x=16\text{m}$, respectively.

In order to determine the motion of sediments, one should define the subsequent frame numbers. Various frame intervals are studied. It is observed that the most of the moving sediments are rolling and saltating. Consequently, the area of the sediment changes and it is difficult to capture the sediment in two frames having more than 2 frame intervals. Therefore 1 frame interval is selected for the investigation.

In the image processing part of the study, the average velocity of the grains in two consecutive frames is obtained. The pixel values of the two subsequent images of gray scale (Figure 5.30.a and 5.30.b) are subtracted and two images are obtained. The initial and final positions of the sediments are obtained as shown in figure 5.30.c and figure 5.30.d. For $x=11\text{m}$ 2×25 and for $x=16\text{m}$ 2×60 frames are manually examined at various times. It is observed that some of the sediments are just fluctuating and do not move afterwards. Also because of the variable lightening conditions some shades appear which result in white areas in binary image although there is no movement. This introduces noise and requires careful detection of the sediments. Therefore, for each consecutive frame, a variable threshold value is used to convert the gray scale image into the binary image. A median filter in Matlab is

used to eliminate the noise from the binary images (Matlab, 2007b). The final binary images are given in figure 5.30.e and 5.30.f. The small white areas in the binary image allow us to determine the extent of the movement as well as the velocity of sediments. Then the average velocity of the sediments is calculated by knowing the horizontal and vertical displacement and the time interval as given in figure 5.31.a and figure 5.31.b.

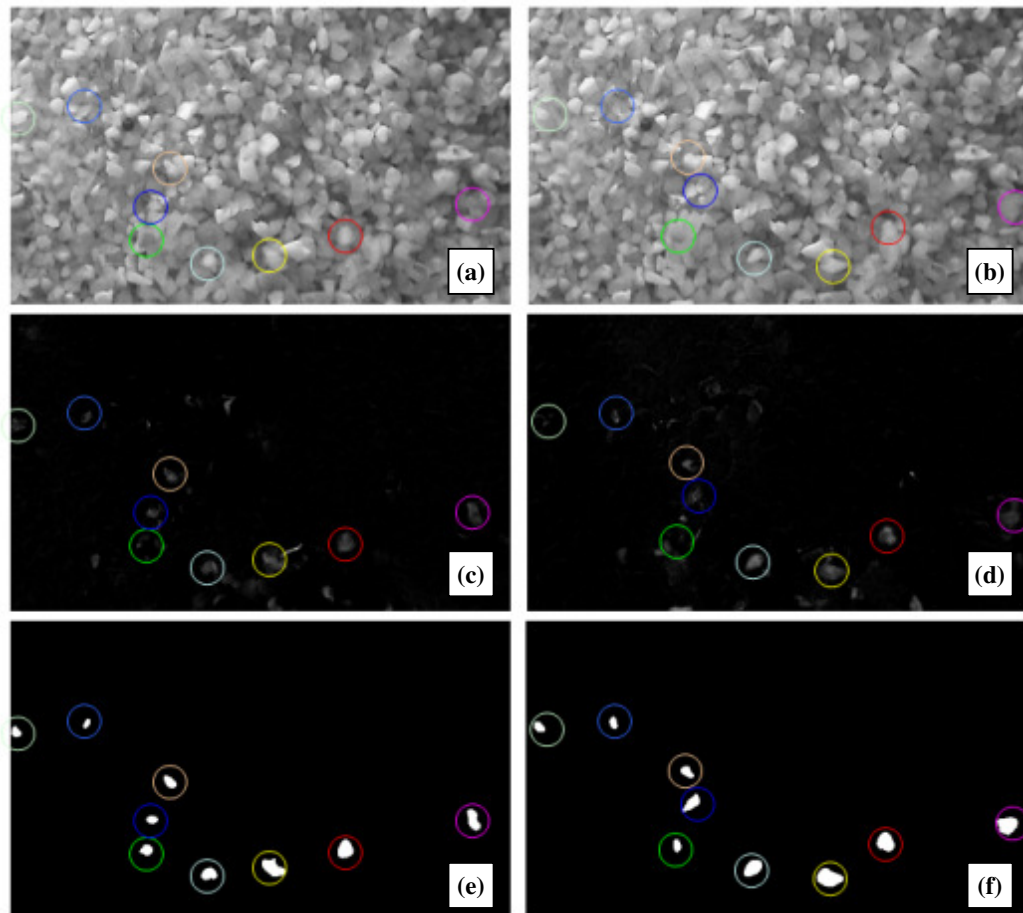


Figure 5.30 a,b,c,d Movement of sediment and the processing procedure between frame 100 and frame 101, for $t=21.8s$, at $x=16m$

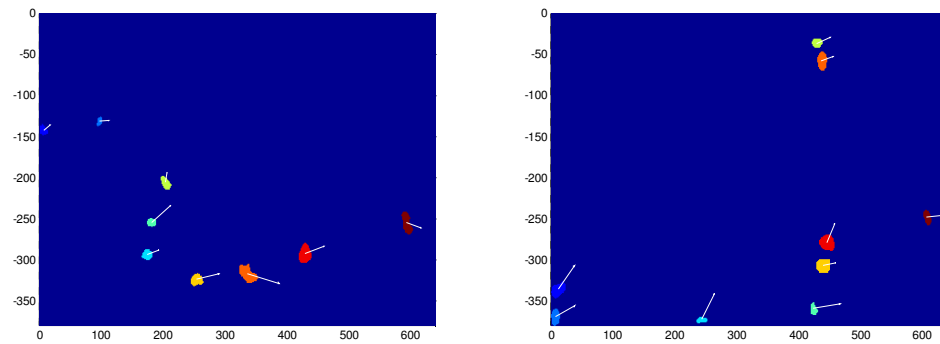


Figure 5.31 Sediment velocities in two consecutive frames, (a) at $t=10$ s (frame 60), (b) at $t=26$ s (frame 200) at $x=16$ m.

In order to obtain the individual grain velocity, 39 grains at various frames are tracked and their instantaneous velocities are determined and compared with the velocities averaged by frame as given in figure 5.32. It is seen that the frame velocity is nearly constant and equal to the average value of 17.8 cm/s at $x=16$ m throughout the hydrograph, whereas the individual velocities fluctuate around this value. It is revealed that the two ways of velocity determination is in accord. For the case at $x=11$ m the average frame velocity is 15.8 cm/s. During the proceeding calculations, the average frame velocity is considered.

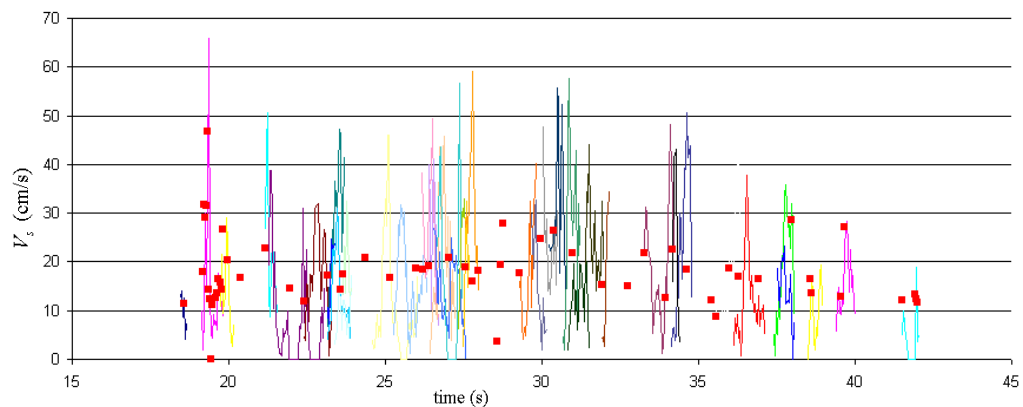


Figure 5.32 Time variation of the sediment velocities averaged by frame and instantaneous individual sediment velocities at $x=16$ m

The records are analyzed by image processing technique to determine the number and area of active grains moving at any instant. In literature it is advised to make a

manual calibration for the determination of the moving area and the total number of active sediments moving at any instant. A constant threshold of 0.130 and filter of 8 is used for area which makes the best fit as given in figure 5.33.a and a constant threshold of 0.190 and filter of 8 is used for number of grains which makes the best fit as given in figure 5.33.b for the recordings at x=16m. At x=11m, the values are 0.072 and filter of 8 is used for area and a constant threshold of 0.107 and filter of 8 is used for number of grains. The noise is due to the shades and fluctuating sediments and results in a deviation for both number of grains and the area. The sediments are rolling, sliding and saltating through the observation period. Therefore the area of the specific sediment in one frame may not have the same shape and size at the proceeding frame.

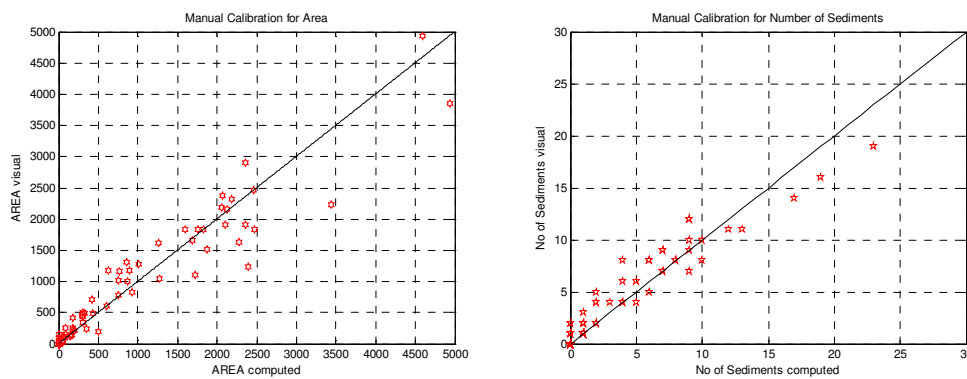


Figure 5.33 (a) for moving area in pixel², (b) for the number of grains at x=16m

The area in pixel² is converted into cm² by knowing the frame limits i.e. aspect ratio in pixels and cm which was previously determined by a ruler. The average diameter of the moving sediments is determined by using the following equation,

$$D = \sqrt{\frac{4}{\pi} \frac{A}{N}} \quad (5.15)$$

where the area A is in cm², N is the number of active grains and D is the average moving sediment diameter in cm. The time variation of the diameter of the moving sediment is given in figure 5.34. It is revealed that the average diameter of the moving sediment fluctuates around the D_{50} of the bed material (=4.8mm).

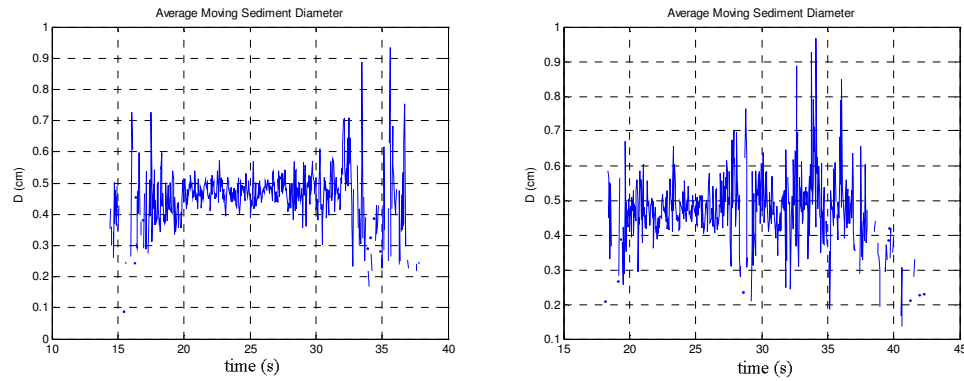


Figure 5.34 Time variation of average diameter of moving sediment (a) at $x=11$ m, (b) at $x=16$ m

The average velocity is calculated by considering both horizontal and vertical component of the sediment velocities in the frames. The average velocity of the frame, the diameter and number of active sediments at each frame is used to find the bed load per unit width by using the equation 5.16.

$$g_{bA} = N \left(\frac{\pi}{6} D^3 \right) \gamma_s \frac{1}{\Delta x \Delta y} V_s \quad (5.16)$$

where g_{bA} is the bed load calculated from the image processing technique, D is the diameter of active grains, V_s is the average velocity at each consecutive frame, Δx and Δy are the horizontal and vertical length reaches of the frame. The bed load per unit width obtained at $x=16$ m by using equation 5.16 and that measured by sediment baskets are given in figure 5.35. It is observed that, the local bed load motion is not continuous, but sporadic, having a pulsing nature.

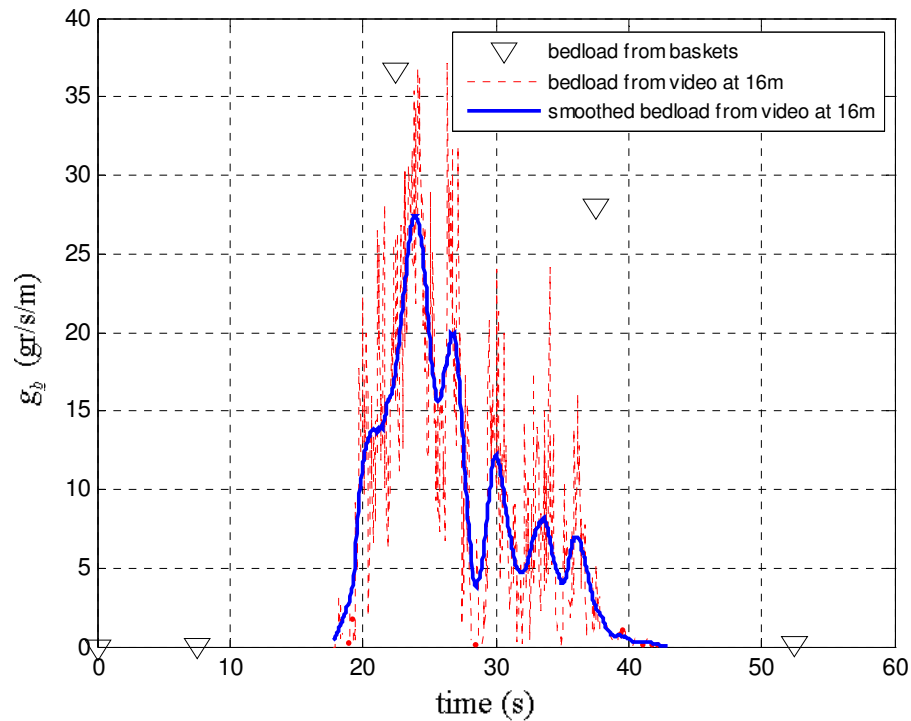


Figure 5.35 The bed load obtained by the image processing technique at $x=16\text{m}$ and the bed load measured at the sediment baskets

The two bed load measurement techniques are relatively in accord. The difference may arise from the small area visualized by the camera. The camera being located 2.6m before the downstream end where the sediments are collected influences the amount of collected sediments.

The smoothed bed load per unit width obtained at $x=11\text{ m}$ and $x=16\text{ m}$ are given in figure 5.36. The time at which the motion starts is 14.0 s and the time at which the motion terminates is 37.2 s, at $x=11\text{m}$. The time at which the motion starts is 17.8 s and the time at which the motion terminates is 43.0 s, at $x=16\text{m}$.

According to these timings, these correspond to shear velocities of 4.7 cm/s and 4.8 cm/s for 11m and 4.6 cm/s and 5.2 cm/s for 16 m. They also correspond to flow depths of 4.6 cm and 7.3 cm for 11m and 4.5 cm and 6.3 cm for 16 m. The steady flow experiments conducted in the same flume with same bed material showed that

the threshold value of flow depth for inception of motion is 7.1 cm. This reveals that the bed motion starts before the critical conditions are reached for steady case. The finalization of motion is at depths more close to the critical conditions for steady case.

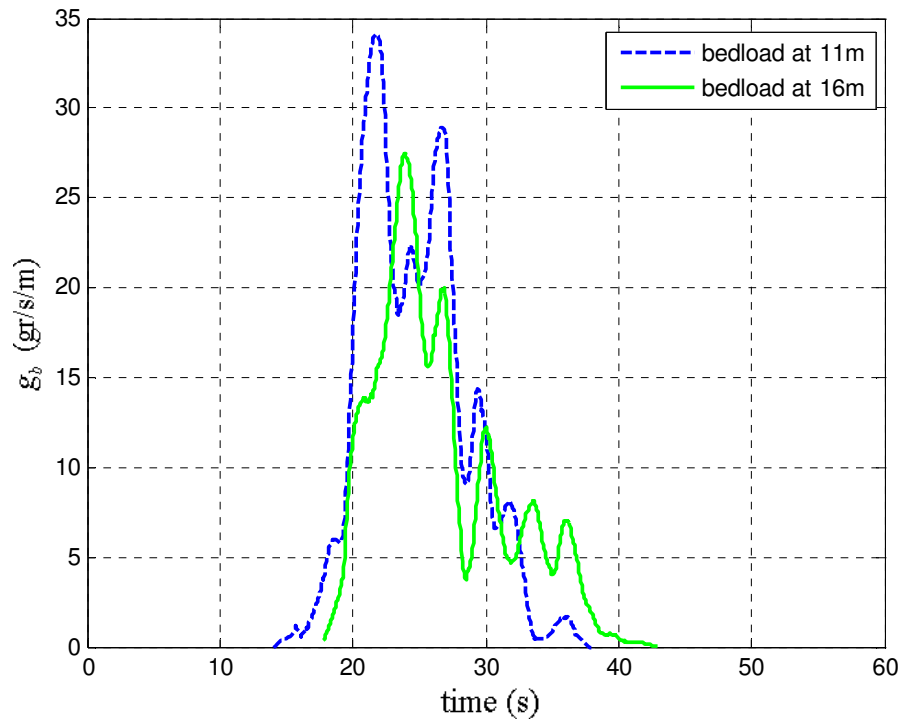


Figure 5.36 The bed load obtained by the image processing technique at $x=11\text{m}$ and $x=16\text{m}$

The pulsing nature of the continuous bed load transport is explicitly seen in figure 5.36 where the pulse interval is approximately 3 seconds. It is worth to discuss the reason of the fluctuations or the pulse waves obtained in continuous bed load transport measurements by video image processing technique which is not visible in the sediment basket collection method where the fluctuations are suppressed by the collection with baskets because of the long collection duration, i.e. 15 seconds. The fluctuations obtained in image processing technique are reported by many researchers who conducted continuous bed load measurements in both field and laboratory measurements (Emmett, (1975), Einstein (1937), Reid et.al. (1985), Govi et.al. (1993), Banzinger and Burch (1990), Lee et. al (2004)).

In this study, since in the steady flow experiments at high discharges some alternate bars are observed, the pulsing nature is attributed to the arrangement of the bed itself to the formation of alternate bars. In the case of hydrograph; as the peak flow duration is relatively short, alternate bars have not enough time to occur.

5.7 Relation Between Dimensionless Shear Stress and Dimensionless Bed Load

In steady flows, there is a unique relation between dimensionless shear stress τ_* and dimensionless bed load q_* where $\tau_* = u_*^2 / g\Delta D_{50}$ and $q_* = q_b / \sqrt{\Delta g D_{50}^3}$. Here, g is the gravitational acceleration, $\Delta = (\rho_s - \rho_w) / \rho_w$, ρ_s and ρ_w are the density of sediment and water respectively, q_b is the volumetric unit width bed load. The unit width bed load g_b can be expressed as $g_b = \gamma_s q_b$, where γ_s is the specific weight of sediment.

Figure 5.37.a illustrates the relation between the q_* obtained from the video recordings and the τ_* obtained from the UVP measurements at 11 m. It is observed that there is not a hysteresis between τ_* and q_* . Measurement of the shear velocity and bed load at the same section of the flume give rise to this relation at $x= 11\text{m}$ even if the high unsteadiness conditions.

Figure 5.37.b based on the q_* obtained from the bed load collected in baskets and the τ_* obtained from the UVP measurements at 11 m, reveals that there is a hysteresis between τ_* and q_* . There is a counter-clock-wise relation between them which also confirms that the bed load is greater in the falling limb than in the rising limb for the same τ_* . This confirms the related study of Qu (2003).

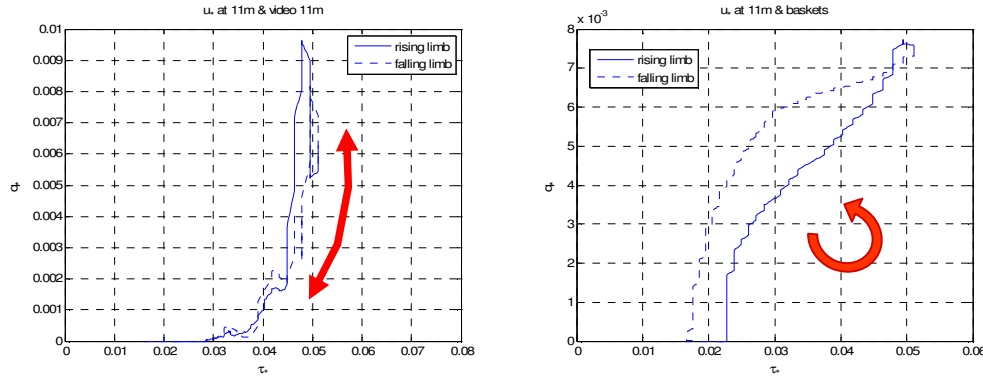


Figure 5.37 The relation between τ_* and q_* where u_* is obtained from universal log law and (a) where q_* is obtained from the image processing and τ_* is obtained at $x=11\text{m}$ and (b) where q_* is obtained from the sediment baskets

The behavior of the sediments at 11m is similar to the ephemeral streams where there is no armor layer. This is due to the initial conditions. The bed is made with constant slope and the sediments are randomly distributed. However for natural bed surface many particles rest in orientations that give them best protection against disturbance (Matin, 1994). The time lag in perennial streams is different from the one in this study. For the laboratory experiments given in literature this difference is thought to be mostly due to the different places of measurement locations of the flow parameter and bed load.

5.8 Bottom Elevation

The bed elevations are measured at every 10 cm in stream wise direction at the center of the flume by 4 MHz UVP transducer, mounted vertically. The zero velocity point with a zero standard deviation is taken as the bed surface. The precision of the measurement is 0.37 mm. The measured bed elevations are depicted in figure 5.38. There is a small local scour at the entrance of the flume. In other places the bed elevations are not changed significantly. The fluctuations are nearly at the same order of magnitude of the grains' median diameter.

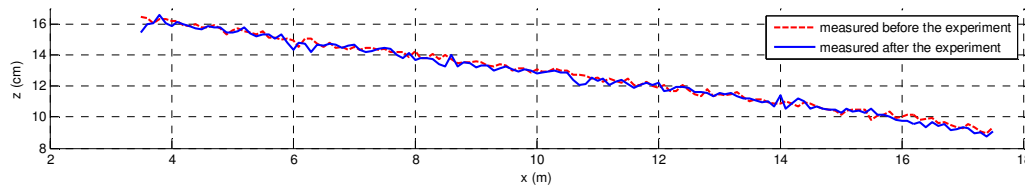


Figure 5.38 The bottom elevations before and after the hydrograph passage for Experiment 4

After the unsteady flow experiments, bed form occurrences like ripples, dunes, alternate bars etc. are not visually observed.

5.9 Spatial and Temporal Distribution of Painted Sediments after Hydrograph

The spatial and temporal distribution of the sediments for the experiment 4 (rising limb duration=120 s, falling limb duration=120 s, base flow=12 l/s and peak flow=68 l/s) is determined. Originally white sediments are painted to green, red, blue and yellow and laid on the bed within a zone 12 cm by 12 cm, along the axis of the flume, at $x=4\text{m}$, 6m , 11m and 16m , respectively (Figure 5.39). Once the hydrograph passed, the dispersed colored sediments are collected at each segment of 25 cm (Figure 5.40.a and figure 5.40.b).



Figure 5.39 The travelled distances of the painted sediments

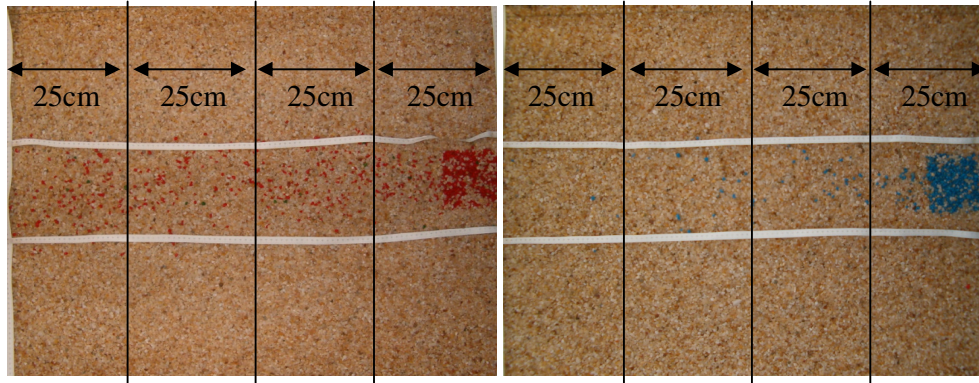


Figure 5.40 The dispersed colored sediments (a) red sediments, (b) blue sediments

The collected colored sediments are weighed. The amount of the painted sediments displaced along the channel is given in figure 5.41. It seems that, only the sediments near the downstream end attain the baskets. It is also observed that during the hydrograph, the previously painted regions are covered by white sediments in a decreasing order in stream wise. The sediments entrained into the flow in the first part of the channel travel more distances than those in the end part of the channel later. The green, red and blue sediments were absent in the baskets. This fact reveals that the bed load collected in the sediment baskets come from the last few meters, and probably from the non-painted zone.

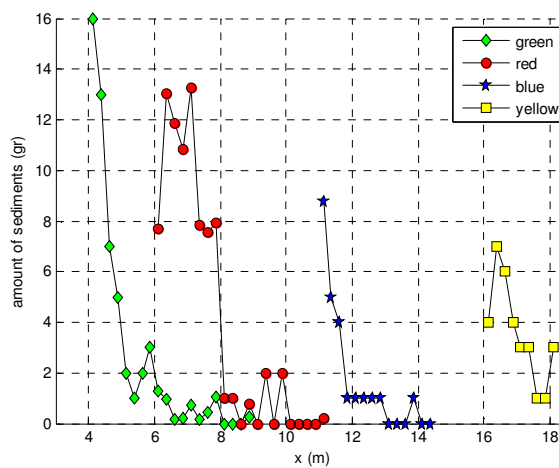


Figure 5.41 The travelled distances of the painted sediments

CHAPTER SIX

GOVERNING EQUATIONS OF SEDIMENT TRANSPORT

The phenomena of flow and sediment transport in rivers are characterized by turbulence, free surface variation, bed change, phase interaction, etc. It is very difficult to include all of these effects accurately in a model for solving practical engineering problems. Therefore, generally sediment transport models adopt the following assumptions (Wu and Wang, 2005) :

(a) Sediment concentration is low enough so that the hydrodynamics of the flow is not affected by the sediment movements. Therefore, the clear-water flow and the sediment advection-diffusion equations are solved separately or decoupled.

(b) The time scale of bed change is much larger than that of flow movement. Therefore, at each time step the flow is calculated assuming a “fixed” bed.

(c) Interactions among different size classes of moving sediment are ignored. Thus the transport of each size class of sediment is handled individually. However, the hiding and exposure mechanism in nonuniform bed material is considered through the introduction of correction factors in the nonuniform sediment transport capacity formulas.

(d) Empirical functions for sediment transport capacities, channel roughness coefficients, constants in the turbulence models, etc. are adopted to close the mathematical model into numerical empirical model to conduct computational simulation.

6.1 Differential Equations of One Dimensional Bed Load Transport

The differential equation for the continuity of water is given in equation (6.1) (Tayfur and Singh, 2006).

$$\frac{\partial h}{\partial t} + \frac{\partial hu}{\partial x} + p \frac{\partial z}{\partial t} = 0 \quad (6.1)$$

where,

x = independent variable representing the coordinate in the longitudinal direction (L)

t = independent variable of time (T)

u = flow velocity (L/T)

h = flow depth (L)

z = mobile bed layer elevation (L)

p = porosity of the bed layer (L^3 / L^3)

The continuity equation for sediment may be expressed as follows (Tayfur and Singh, 2006):

$$\frac{\partial h}{\partial t} + \frac{\partial hu}{\partial x} + (1 - p) \frac{\partial z}{\partial t} + \frac{\partial q_b}{\partial x} = 0 \quad (6.2)$$

where,

q_b = the sediment flux in the movable bed layer (L^2 / T)

The one dimensional partial differential momentum equation of unsteady flow with dynamic wave assumption is;

$$\frac{\partial u}{\partial t} + u \frac{\partial u}{\partial x} + g \frac{\partial h}{\partial x} + g \frac{\partial z}{\partial x} = -gS_f \quad (6.3)$$

If the diffusion wave model which neglects the local acceleration, $\partial u/\partial t$ and convective acceleration, $\partial u/\partial x$ is used, then the momentum equation for flow in a rectangular channel may be simulated as:

$$g \frac{\partial h}{\partial x} + g \frac{\partial z}{\partial x} = -gS_f \quad (6.4)$$

In equations (6.1), (6.2) and (6.4) the unknown parameters are h , u , z , q_b and S_f . It means that there must be two additional equations. One equation may be obtained from Manning equation as given in equation (6.5)

$$u = \frac{1}{n} \left(\frac{B h}{B + 2h} \right)^{2/3} S_f^{1/2} \quad (6.5)$$

For compound channels, the Manning roughness coefficient, n may be calculated according to the equation (6.6) proposed by Lotter (Güney, 2006).

$$n = \frac{2h + B}{\left(\frac{2h}{n_1} + \frac{B}{n_2} \right)} \quad (6.6)$$

where n_1 is the Manning roughness coefficient of the side walls, n_2 is the Manning roughness coefficient of the bottom, h is the flow depth and B is the channel width.

The equation (6.2) requires a relation for the sediment flux in the movable bed layer. The q_b in this equation can be obtained from various empirical equations given by different researchers such as Meyer, Peter and Müller (1948) as in equation (6.7), suggestion of Wong (2003) to Meyer Peter Müller equation as given in equation (6.8), Fernandez Luque and van Beek (1976) as given in equation (6.9) and Engelund and Fredsoe (1976) as given in equation (6.10),...etc.

$$q_b = 8 \sqrt{\Delta g D_{50}^3} (\tau_* - \tau_{*cr})^{3/2} \quad (6.7)$$

$$q_b = 3.97 \sqrt{\Delta g D_{50}^3} (\tau_* - \tau_{*cr})^{3/2} \quad (6.8)$$

$$q_b = 5.7 \sqrt{\Delta g D_{50}^3} (\tau_* - \tau_{*cr})^{3/2} \quad (6.9)$$

$$q_b = 18.74 \sqrt{\Delta g D_{50}^3} (\tau_* - \tau_{*cr}) \left(\sqrt{\tau_*} - 0.7 \sqrt{\tau_{*cr}} \right) \quad (6.10)$$

6.2 Differential Equations of Two Dimensional Bed Load Transport

The two dimensional basic differential equations (continuity and momentum equations) for water are given below (Wu, Wang, 2005):

$$\frac{\partial h}{\partial t} + \frac{\partial hu}{\partial x} + \frac{\partial hv}{\partial y} = 0 \quad (6.11)$$

$$\begin{aligned} \frac{\partial hu}{\partial t} + \frac{\partial(huu)}{\partial x} + \frac{\partial(hvu)}{\partial y} = & -gh \frac{\partial z_s}{\partial x} + \frac{1}{\rho} \frac{\partial(hT_{xx})}{\partial x} + \frac{1}{\rho} \frac{\partial(hT_{yy})}{\partial y} \\ & + \frac{\partial D_{xx}}{\partial x} + \frac{\partial D_{xy}}{\partial y} + \frac{1}{\rho} (\tau_{sx} - \tau_{bx}) + f_c hv \end{aligned} \quad (6.12)$$

$$\begin{aligned} \frac{\partial hv}{\partial t} + \frac{\partial(huv)}{\partial x} + \frac{\partial(hvv)}{\partial y} = & -gh \frac{\partial z_s}{\partial y} + \frac{1}{\rho} \frac{\partial(hT_{yx})}{\partial x} + \frac{1}{\rho} \frac{\partial(hT_{yy})}{\partial y} \\ & + \frac{\partial D_{yx}}{\partial x} + \frac{\partial D_{yy}}{\partial y} + \frac{1}{\rho} (\tau_{sy} - \tau_{by}) + f_c hu \end{aligned} \quad (6.13)$$

where x and y are the horizontal Cartesian coordinates; h is the flow depth; u and v are the depth averaged flow velocities in x - and y -directions; z_s is the water surface

elevation; g is the gravitational acceleration; T_{xx} , T_{xy} , T_{yx} and T_{yy} are the depth-averaged turbulent stresses; D_{xx} , D_{xy} , D_{yx} and D_{yy} are the dispersion terms due to the nonuniformity of flow velocity and the effect of secondary flow, which are important in the situation of curved channels; ρ is the density of water; τ_{bx} and τ_{by} are the bed shear stresses and determined by equations (6.14) and (6.15).

$$\tau_{bx} = \rho c_f u \sqrt{u^2 + v^2} \quad (6.14)$$

$$\tau_{by} = \rho c_f v \sqrt{u^2 + v^2} \quad (6.15)$$

The c_f in these equations is calculated by equation (6.16).

$$c_f = \frac{gn^2}{\sqrt[3]{h}} \quad (6.16)$$

where n is Manning's roughness coefficient; τ_{sx} and τ_{sy} represent the shear forces acting on the water surface, usually caused by wind driving; and f_c is the Coriolis coefficient (Wu, Wang, 2005).

The bed-load transport due to size class k is determined by equation (6.17)

$$\frac{\partial(\delta_b \bar{c}_{bk})}{\partial t} + \frac{\partial(\alpha_{bx} q_{bk})}{\partial x} + \frac{\partial(\alpha_{by} q_{bk})}{\partial y} + \frac{1}{L_s} (q_{bk} - q_{b^*k}) = 0 \quad (k = 1, 2, \dots, N) \quad (6.17)$$

where \bar{c}_{bk} is the average concentration of bed load at the bed-load zone; q_{bk} is the bed-load transport rate of size class k ; q_{b^*k} is the corresponding bed-load transport capacity or bed-load transport rate at the equilibrium state; and α_{bx} and α_{by} are the direction cosine components of bed load movement, which is assumed to be along the direction of bed shear.

The bed deformation due to size class k is calculated by

$$(1-p)\left(\frac{\partial A_b}{\partial t}\right)_k = \frac{1}{L_s}(Q_{tk} - Q_{t^*k}) \quad (k=1,2,\dots,N) \quad (6.18)$$

where p is the bed material porosity; A_b is the cross-sectional area of the bed above a reference datum; and $(\partial A_b / \partial t)_k$ is the bed deformation rate caused by size class k , L_s is the nonequilibrium adaptation length of sediment transport; Q_{tk} is the actual sediment transport rate; Q_{t^*k} is the sediment transport capacity or the so-called equilibrium transport rate. The sediment transport capacity is determined by several well-tested empirical formulas which are written in a general form as in equation (6.19).

$$Q_{t^*k} = p_{bk} Q_{tk}^* \quad (k=1,2,\dots,N) \quad (6.19)$$

where p_{bk} is the availability factor of the k^{th} size class of sediment, which is defined here as the percentage of size class k in the mixing layer of bed material; and Q_{tk}^* is the potential sediment transport capacity of size class k .

CHAPTER SEVEN

NUMERICAL SOLUTION

In the scope of this thesis only one dimensional transport with diffusion wave model is studied numerically.

7.1 Numerical Model

In this study, a finite difference scheme developed by Lax (1954) is used. This scheme is also successfully used by Bor (2008) for unsteady flows and sediment transport. The Lax scheme is an explicit scheme and with notations shown in figure 7.1, the partial derivatives and other variables are approximated as follows (Bor, 2008):

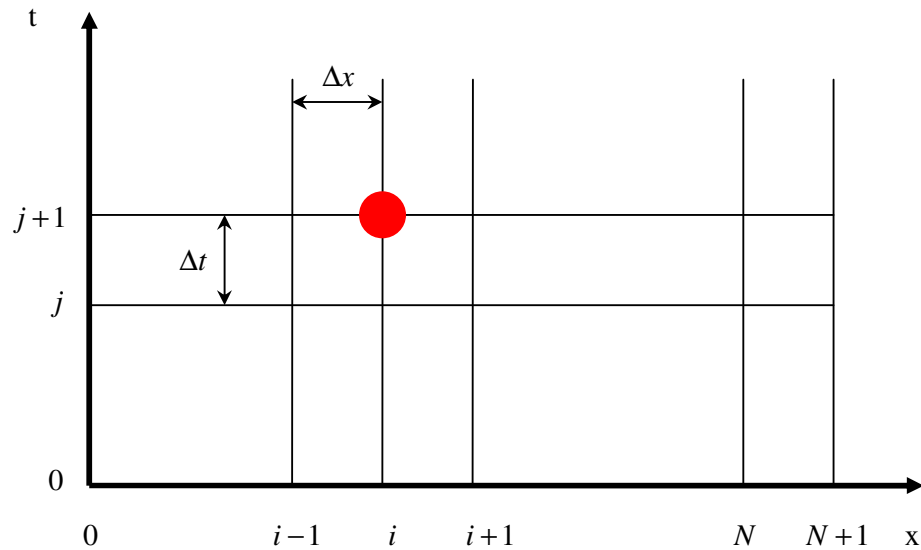


Figure 7.1 Finite – difference grid

$$\frac{\partial f}{\partial t} = \frac{f_i^{j+1} - 0.5(f_{i+1}^j + f_{i-1}^j)}{\Delta t} \quad (7.1)$$

$$\frac{\partial f}{\partial x} = \frac{f_{i+1}^j - f_{i-1}^j}{2\Delta x} \quad (7.2)$$

where,

i = the node number (index) in space

j = the node number (index) in time

Δx and Δt = the distance and time steps, respectively.

The statements so obtained for h_i^{j+1} , u_i^{j+1} , $S_{f_i}^{j+1}$, z_i^{j+1} and q_{bi}^{j+1} , by using the bed load empirical formulas (6.7) to (6.9), are presented by equations (7.3) to (7.7).

$$S_{f_i}^{j+1} = -\frac{(h_{i+1}^j - h_{i-1}^j)}{2\Delta x} - \frac{(z_{i+1}^j - z_{i-1}^j)}{2\Delta x} \quad (7.3)$$

$$z_i^{j+1} = -A\sqrt{\Delta g D_{50}^3} \frac{3}{2} \left(\frac{h_i^j S_{f_i}^{j+1}}{\Delta D_{50}} - \tau_{cr}^* \right)^{1/2} \left(\frac{S_{f_i}^{j+1}}{\Delta D_{50}} \right) \left(\frac{h_{i+1}^j - h_{i-1}^j}{2\Delta x} \right) \frac{\Delta t}{(1-p)} + \frac{(z_{i+1}^j - z_{i-1}^j)}{2} \quad (7.4)$$

$$h_i^{j+1} = -\frac{2}{3n} \left(\frac{b + 2h_i^j}{b(h_i^j)^{5/2}} \right)^{1/3} \left[\frac{-2b(h_i^j)^{5/2}}{(b + 2h_i^j)^2} + \frac{5b(h_i^j)^{3/2}}{2(b + 2h_i^j)} \right] (S_{f_i}^{j+1})^{1/2} \left(\frac{h_{i+1}^j - h_{i-1}^j}{2\Delta x} \right) \Delta t \\ - p [z_i^{j+1} + 0.5(z_{i+1}^j + z_{i-1}^j)] + 0.5[h_{i+1}^j + h_{i-1}^j] \quad (7.5)$$

$$u_i^{j+1} = \frac{1}{n} \left(\frac{bh_i^{j+1}}{b + 2h_i^{j+1}} \right)^{2/3} (S_{f_i}^{j+1})^{1/2} \quad (7.6)$$

$$q_{bi}^{j+1} = -A\sqrt{\Delta g D_{50}^3} \left(\frac{h_i^{j+1} S_{f_i}^{j+1}}{\Delta D_{50}} - \tau_{cr}^* \right)^{3/2} \quad (7.7)$$

where A denotes the factor in equations (6.7), (6.8) and (6.9) which takes the value of 8, 3.97 and 5.7, respectively.

If the empirical relation (6.10) given by Engelund and Fredsoe (1976) is used, The expressions of z_i^{j+1} and q_{bi}^{j+1} become:

$$z_i^{j+1} = -18.74\sqrt{\Delta g D_{50}^3} \left\{ \frac{3}{2} \left(\frac{h_i^j S_{fi}^{j+1}}{\Delta D_{50}} - \tau_{cr}^* \right)^{1/2} - \tau_{cr}^* \left(\frac{\Delta D_{50}}{4h_i^j S_{fi}^{j+1}} \right)^{1/2} - 0.7\sqrt{\tau_{cr}^*} \right\} \\ * \left(\frac{S_{fi}^{j+1}}{\Delta D_{50}} \right) \left(\frac{h_{i+1}^j - h_{i-1}^j}{2\Delta x} \right) \frac{\Delta t}{(1-p)} + \frac{(z_{i+1}^j - z_{i-1}^j)}{2} \quad (7.8)$$

$$q_{bi}^{j+1} = 18.74\sqrt{\Delta g D_{50}^3} \left(\frac{h_i^{j+1} S_{fi}^{j+1}}{\Delta D_{50}} - \tau_{cr}^* \right) \left[\left(\frac{h_i^{j+1} S_{fi}^{j+1}}{\Delta D_{50}} \right)^{1/2} - 0.7(\tau_{cr}^*)^{1/2} \right] \quad (7.9)$$

The channel length L is divided into N parts. The length reach becomes $\Delta x = L/N$. The subscripts of nodes vary from 1 to $N+1$ (figure 7.1).

Δt is selected so that the Courant condition

$$\Delta t \leq \Delta x / (c + a) \quad (7.10)$$

is satisfied to get a stable numerical solution. In this equation c denotes wave celerity whose expression for shallow water case is

$$c = \sqrt{gh} \quad (7.11)$$

One begins to calculate the unknown values at $t = \Delta t$ by using the initial values which correspond to $t = 0$. As the parameters corresponding to time $t = \Delta t$ become known, the values for $t = 2\Delta t$ can be easily determined from the values of time $t = \Delta t$. The procedure continues similarly until the desired time limit is attained.

First S_{fi}^{j+1} and z_i^{j+1} are calculated from equations 7.3 and 7.4, respectively. The other unknowns are found by substituting these values in related equations.

Initial conditions can be specified as:

$$h(x,0) = h_o \quad (7.12.a)$$

$$z(x,0) = z_o \quad (7.12.b)$$

$$u(x,0) = u_o \quad (7.12.c)$$

$$q_b(x,0) = q_{bo} \quad (7.12.d)$$

$$S_f(x,0) = S_{fo} \quad (7.12.e)$$

where, the subscript (o) denotes the values at time $t=0$.

The upstream boundary conditions can be specified as inflow hydrograph.

$$h(0,t) = h(t) \quad (7.13.a) \text{ or}$$

$$Q(0,t) = Q_o(t) \quad (7.13.b)$$

The downstream boundary conditions can be specified as:

$$\frac{\partial h(L,t)}{\partial x} = 0 \quad (h_{N+1}^{j+1} = h_N^{j+1}) \quad t > 0.0 \quad (7.14)$$

or by assuming free fall described by the following equation which is similar to Toricelli formula:

$$u = C\sqrt{h} \quad (u_{N+1}^{j+1} = C\sqrt{h_{N+1}^{j+1}}) \quad t > 0.0 \quad (7.15)$$

at which C is a constant.

7.2 Comparison of Numerical and Experimental Results

The experiment corresponding to the triangle shaped hydrograph given as experiment 4 (rising limb duration=120 s, falling limb duration=120 s, base flow=12 l/s and peak flow=68 l/s) is taken, as illustrative example, for the comparison of the experimental findings with the numerical model solutions. This hydrograph constitute the upstream boundary condition.

The initial conditions are $h_o = 0.04$ m, the bed depth is 0.08 m, $u_o = 0.38$ m/s, $q_{bo} = 0$, $S_{fo} = S_o = 0.005$. The relation given by equation 7.14 is taken as downstream boundary condition.

The manning coefficient, n is calculated for compound channels according to the equation (6.6) where n_1 is the Manning roughness coefficient of the side walls and taken as 0.009, n_2 is the Manning roughness coefficient of the sediment layer at bottom and it is taken equal to 0.025.

The channel is divided into 20 parts which gives $\Delta x = 1$ m.

The maximum water depth is considered as

$$h_{\max} = 0.105 \text{ m}$$

which gives for the maximum celerity

$$c_{\max} = \sqrt{981(10.5)} = 101 \text{ cm/s}$$

By taking the maximum flow velocity $u_{\max} = 80$ cm/s, the Courrant condition becomes

$$\Delta t \leq \frac{100}{101 + 80} = 0.55 \text{ s}$$

In the numerical solution Δt is selected as 0.1 s which satisfies the Courant condition.

All the empirical formulas (equations 6.7 to 6.10) related to bed load are used. The obtained numerical results and the experimental ones are presented in the same figure.

Figure 7.2 represents the experimental bed elevations along the channel before and at the end of the experiments and the theoretical ones.

The velocity variations with time at section $x=11\text{m}$ from the entrance are given in figure 7.3.

The flow depth variations versus time at section $x=11\text{m}$ from the entrance are illustrated in figure 7.4.

The bed loads collected in baskets during the experiment and the theoretical ones are depicted in figure 7.6.

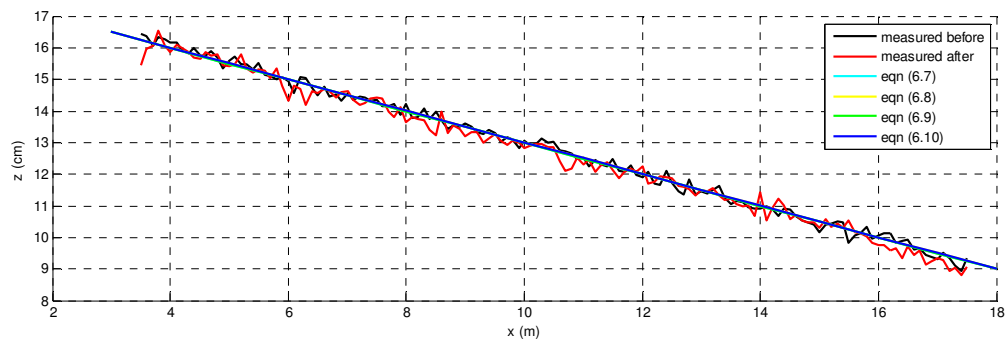


Figure 7.2 Experimental bed elevations along the channel before and at the end of the experiments and the theoretical ones by using for bed load equations (6.7) to (6.10)

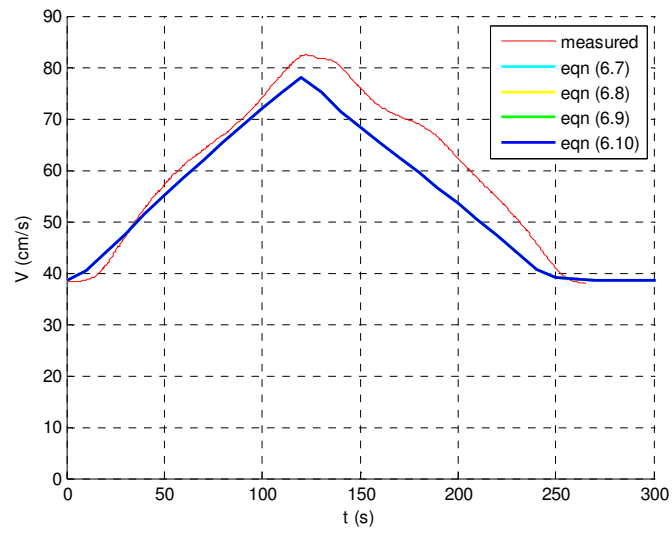


Figure 7.3 Experimental and theoretical velocity variations with time at section $x=11\text{m}$ from the entrance by using for bed load equations (6.7) to (6.10)

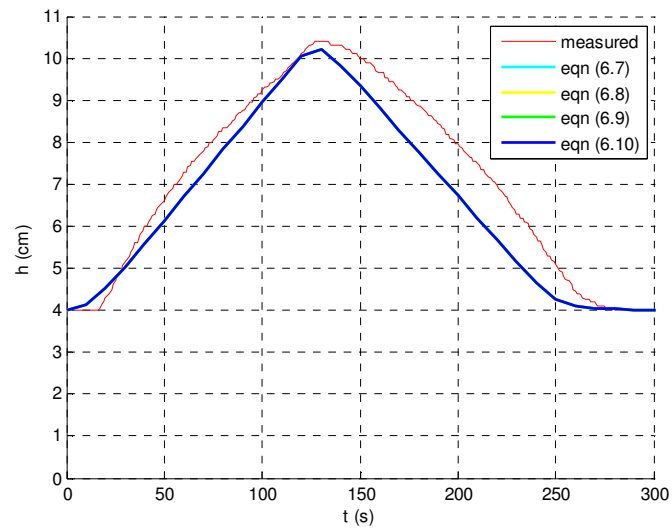


Figure 7.4 The experimental and theoretical flow depth variations versus time at section $x=11\text{m}$ by using for bed load equations (6.7) to (6.10)

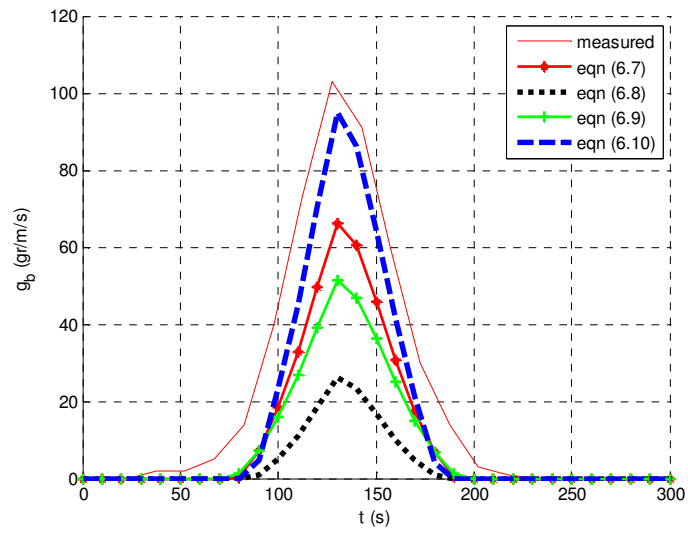


Figure 7.5 The bed loads collected in baskets during the experiment and the theoretical ones obtained at downstream end by using the bed load equations (6.7) to (6.10)

CHAPTER EIGHT

CONCLUSION

The aim of this experimental study is to investigate the mechanism of the inception of bed material and its transport in steady as well as unsteady flow. Numerous flume experiments are conducted using different triangular shaped input hydrographs.

The steady flow experiments are done with immobile and mobile bed by using elaborate devices giving the opportunity of recording during the experiments. The unsteady flow experiments are conducted with hydrographs having rising and falling durations of 15 seconds to 120 seconds, from the steady state value of 12.0 l/s and 30.3 l/s to the peak value of 53.5 l/s and 89.9 l/s.

The velocity values are measured precisely by using UVP. The level meters provided accurate measurements of water depths. The magnetic flow meter allowed to measure flow rates correctly.

The Shields approach (1936) as given in figure 2.1, Meyer Peter Müller (1948) approach given by equation (2.6) and Yang's approach (1973) given by equation (2.7) for the critical point for inception of sediment motion are investigated and compared with the experimentally obtained results. It is found that Shields approach is the best one that is in accord with the experimental results.

The measured bed load values are compared with those calculated from the empirical relations given in the relevant literature. It is found that the measured bed load values are better compatible with those calculated from the expressions given by Meyer, Peter and Müller (1948) in equations (2.24) and (2.25) and that given by Rottner (1959) in equation (2.26).

In unsteady flow conditions, the best formula concerning the bed load for experiment 1 and 2 seems to be that of Fernandez Luque and van Beek (1976) given in equation (5.16). For the rest of the experiments the Engelund and Fredsoe (1976) formula given in equation (5.15) is the most compatible with experimental data.

In image processing analysis, the average grain velocity is investigated throughout the hydrograph for experiment 1 (rising limb duration=15 s, falling limb duration=15 s, base flow=12 l/s and peak flow=53.5 l/s). Although the individual sediment velocities fluctuate too much, the average velocity of each frame revealed that as soon as the sediment start their motion, their velocity is approximately constant till nearly the end of the hydrograph.

The hysteresis phenomenon is investigated in detail for experiment 1. In the time lag analysis, the q_* obtained from the video recordings and the τ_* obtained from the UVP measurements at 11 m are used. It is observed that there is not a hysteresis between τ_* and q_* . The shear velocity and bed load measured at the same section of the flume give rise to this behavior at $x= 11\text{m}$. When the q_* obtained from the bed load collected in baskets and the τ_* obtained from the UVP measurements at 11 m are used, a hysteresis between τ_* and q_* is observed. This hysteresis of a counter-clock-wise sense indicates that the bed load is greater in the falling limb than in the rising limb for the same τ_* . In the laboratory experiments, some researchers found that there exists a hysteresis on the functional relation between q_* and τ_* , implying that the bed load is generally greater in the falling limb than in the rising limb for the same shear stress. This fact is due to the time history of the sediments in motion or the movement of bed forms. The field studies show that the existence of the hysteresis is due to the availability of the sediment supply and the existence of armor. In the ephemeral streams, the abundant supply of sediment and lack of armoring makes the response of bed load as soon as possible to the change in flow conditions. The non hysteric behavior of the bed load in this study at 11 m, is attributed to the randomly distributed protruding grains which are ready to move. Therefore it is

thought that, the lag of the bed load depends particularly on the location of the measured parameter.

From the camera records, it is revealed that the bed load motion is not continuous, but sporadic, which results in fluctuating character. The pulsing nature of the bed load obtained by video recordings is attributed to the arrangement of the bed itself for the formation of alternate bars. Some researchers who observed this phenomenon attributed this to migrating bed forms (Lee et. al, 2004), kinematic wave theory (Reid et.al., 1985) and stream-wise sediment sorting (Iseya and Ikeda, 1987). Since the peak flow duration is nearly instantaneous, on the contrary of steady flow of long durations, alternate bars could not find enough time to be formed.

The one dimensional partial differential equations for the continuity of water and for sediment and the differential momentum equation with diffusive wave assumption is numerically solved by using a finite difference scheme developed by Lax (1954). The manning coefficient, n is calculated according to the equation for compound channels, proposed by Lotter (Güney, 2006). The bed load is obtained from various empirical relations given by different researchers. The experiment corresponding to the triangle shaped hydrograph given as experiment 4 (rising limb duration=120 s, falling limb duration=120 s, base flow=12 l/s and peak flow=68 l/s) is taken, as illustrative example. The bed elevations along the channel, the velocity and flow depth variations with time and the bed loads collected in baskets during the experiment are compared with the numerical model solutions.

In the numerical solution, it is revealed that the formula of Engelund and Fredsoe (1976) given in equation (6.10) is the best formula related to the bed load transport.

The one dimensional sediment transport equations are not sufficient to study bed deformations accurately. The numerical solutions need to be performed by using two dimensional equations. Additionally a more elaborate measuring system is required to determine bed configurations precisely.

The compaction of the sediment is very crucial for the sediment transport especially in the experimental studies in flumes. In the future studies, the different input hydrographs in channels containing differently compacted bed material may be performed to investigate the effect of compaction.

In the further studies:

- New formulas about the inception of motion and the amount of bed load can be developed by performing extensive experiments
- The new hydrographs with different shapes, (trapezoidal, bell shaped etc..) may be generated and their effects on the results can be investigated
- The experiments with sedimentograph (by feeding with sediment) may be realized in order to study the circumstances encountered in nature
- The differential equations for two dimensional transport can be handled by using more elaborate numerical methods in order to study the bed forms and to compare with those encountered in real life
- The experiments with non uniform bed material can be carried out
- The effects of the thickness and compaction of the bed layer on the sediment transport phenomenon can be investigated
- The effects of sediment transport on the efficiency of hydraulic structures (bridge piers, reservoirs,..) worth to be studying.

REFERENCES

- Ardıçlıođlu, M., (1994), *Pürüzsüz açık kanal akımlarında türbülanslı hız dağılımının lazer doppler anemometresi ile incelenmesi*, doktora tezi, Çukurova Üniversitesi
- Ashida, K. and Michiue M., (1972), Study on hydraulic resistance and bedload transport rate in alluvial streams, *Transactions, Japan Society of Civil Engineering*, 206, pp 59-69
- Banzinger, R., Burch, H., (1990), *Acoustic sensors (hydrophones) as indicators for bed load transport in a mountain torrent*, Hydrology in Mountainous Regions, Proc. Lausanne Symp., August 1990, 207-214. IAHS Publ. no. 193
- Bell, R.G., Sutherland, A.J., (1983), Non-equilibrium bed load transport by steady flows, *A.S.C.E. Journal of Hydraulics Division*, Vol 109, pp 351-365
- Billi, P., Tacconi, P., (1987), Bed load transport processes monitored at Virginio creek measuring station, Italy, *International Geomorphology 1986, Proc. 1st International Conference on Geomorphology, Manchester*, September 1985, ed. V. Gardiner, 549-559, Wiley & Sons, Chichester, UK
- Bor (2008), *Numerical modeling of unsteady and non-equilibrium sediment transport in rivers*, Master thesis, IYTE, İzmir
- Çokgör, Ş., Diplas, P., (2001), Bed load transport in gravel streams during floods, *Bridging the Gap: Meeting the World's Water and Environmental Resources Challenges, Proceedings of World Water and Environmental Resources Congress*, 2001, ASCE, section 1, chapter 47

- Da Silva, A.M.F., (2006), On the initiation of meandering and subsequent plan-development of meander loops, *The 7th International Conference on Hydroscience and Engineering (ICHE-2006)*, Sep 10 – Sep 13, Philadelphia, USA
- De Sutter, R., Verhoeven, R., (2001), Simulation of sediment transport during flood events: laboratory work and field experiments, *Hydrological Sciences—Journal—des Sciences Hydrologiques*, 46(4) August 2001, pp. 599–610.
- DuBoys (1879), Le Rhone et les Rivieres a Lit affouillable, *Annales de Ponts et Chaussées*.5, Vol. 18, pp. 141-195
- Einstein, H.A. (1937), Die Eichung des im Rhein verwendeten Geschiebefangers, *Schweizer, Bauzeitung*, 110, 29-32
- Einstein, H.A. (1950), *The Bed Load Function for Sediment Transportation in Open Channel Flows*, Technical Bulletin no. 1026, U.S. Department of Agriculture, Washington, D.C.
- Emmett, W.W., (1975), The channels and waters of the upper Salmon River area, Idaho, *US Geol. Surv. Prof. Pap.*, 870-A
- Engelund, F. and J. Fredsoe, (1976), A sediment transport model for straight alluvial channels, *Nordic Hydrology*, 7, pp 293-306.
- Ergenzinger, P., (1988), The nature of coarse material bed load transport, Sediment Budgets, *Proceedings of the Porto Alegre Symposium*, December 1988, IAHS Publ no 174
- Fernandez Luque, R. and R. van Beek, (1976), Erosion and transport of bedload sediment, *Journal of Hydraulic Research*, 14(2), pp 127-144.

- Govi, M., Maraga, F., Moia, F., (1993), Seismic detectors for continuous bed load monitoring in a gravel stream, *Hydrological Sciences*, 38, 2, 4/1993, 123-132
- Graf, W. H., Altınakar, M. S., (1998), *Fluvial Hydraulics – Flow and transport process in channels of simple geometry*, John Wiley & Sons Inc, 1998
- Graf, W.H., Suszka, L., (1985), Unsteady flow and its effect on sediment transport, *Proceedings, 21st IAHR Congress*, August 1985, Melbourne, Australia, pp 540-544
- Graf, (1971), *Hydraulics of sediment transport*, McGraw-Hill Inc, USA
- Griffiths, G.A., Sutherland, A.J., (1977), Bedload transport by translation waves, *A.S.C.E. Journal of Hydraulics Division*, Vol 103, pp 1279-1291
- Güney, M.Ş., (2006), *Laboratuvar Uygulamalı Hidrolik*, Dokuz Eylül Üniversitesi Mühendislik Fakültesi Basım Ünitesi, İzmir
- Güney, M.Ş., Bombar G., Tayfur, G., Elçi, Ş., (2009) Calculation of the Time-varying Mean Velocity by Ensemble Average, FFT, Smoothing Algorithm, Wavelet and the EMD Methods and Determination of the Turbulence Intensities, *8th International Congress on Civil Engineering*, May 11-13, 2009, Shiraz University, Shiraz, Iran
- Huang, N.E., Shen, S.S.P., (2005) *Hilbert-Huang Transform and Its Applications*, Interdisciplinary Mathematical Sciences.
- Hubbell, D. W., Stewens, H.H., Skinner, J.V., Beverage, J.P., (1987), Laboratory data on coarse-sediment transport for bed load-sampler calibrations, *USGS Wat. Supply Pap. 2299*

- Iseya, F., Ikeda, H., (1987), Pulsations in bedload transport rates induced by a longitudinal sediment sorting: a flume study using sand and gravel mixtures, *Geogr. Ann.* 69 A (1): 15-27
- Jamieson, E., Rennie, C.D., Ramooz, R., (2008), Validation of aDcp bedload transport measurements, *Proceedings of River Flow 2008*, vol 3, pp 2343-2351
- Jong C.D., Ergenzinger, P., (1994), Interpreting the temporal and spatial dynamics of bed load transport phases according to FAST (Fluid and Sediment Transfer Model), *Variability in Stream Erosion and Sediment Transport, Proceedings of the Canberra Symposium*, December 1994, IAHS Publ. no. 224, pp 25-31
- Keshavarzy, A., Ball, J.E., (1999), An application of image processing in the study of sediment motion, *Journal of Hydraulic Research*, Vol 37, No 4, pp 559-576
- Klingeman, P.C., Emmett, W.W., (1982), *Gravel bed load transport process*, in Hey, R.D., Bathrust, J.C., and Thorne, C.R. (Eds), *Gravel-bed Rivers*, Wiley, Chicago, 77-2509, 27 pp.
- Kuhnle, R.A., (1992), Bedload transport during rising and falling stages on two small streams, *Earth Surface Processes and Landforms*, Vol 17, pp 191-197
- Langbein, W.B., Leopolds, L.B., (1968), River channel bars and dunes – theory of kinematic waves, *US Geol. Surv. Prof. Pap.*, 422-L, 20 pp
- Lax, P.D.(1954), Weak solutions of nonlinear hyperbolic equations and their numerical computation, *Commun. Pure and Appl. Math.* 7, 159
- Lee, Tun Lee, Liu, Yi-Liang, Cheng, Kai-Hung, (2004), Experimental Investigation of Bedload Transport Processes under Unsteady Flow Condition, *Hydrological Processes*, 18, 2439-2454

- Lin, Y.T., (2005), *Decomposing non-stationary turbulent velocity in open channel flow*, Final Project
- Malavasi, S., Radice, A., Ballio, F., (2004), Study of sediment motion in local scour hole through an image processing technique, *Proceedings of River Flow 2004*, vol 2, pp 535-542
- Matin, H., (1994), *Incipient motion and particle transport in gravel-bed streams*, Doctoral Dissertation, Department of Civil Engineering, Corvallis, OR, Oregon State University, 268 p.
- The Mathwork Inc. (1994) *Curve Fitting Toolbox User's Guide*, Matlab2007a, from <http://www.mathworks.com/access/helpdesk/help/toolbox/curvefit/bqswfbh-1.html>
- The Mathwork Inc. (1994) *Image Processing Toolbox User's Guide*, Matlab2007b, from <http://www.mathworks.com/access/helpdesk/help/toolbox/images/bqj5b2j.html>
- The Mathwork Inc. (1994) *Wavelet Toolbox User's Guide*, Matlab2007c, from <http://www.mathworks.com/access/helpdesk/help/toolbox/wavelet/waveleta.html>
- Meade, R.H., Emmett, W.W., Myrick, R.M., (1981), *Movement and storage of bed material during 1979 in East Fork River, Wyoming, USA*, in Davies, T.R.H. and Pearce, A.J. (Eds), *Erosion and Sediment Transport in Pacific Rim Steeplands*. Int. Assoc. Hydrological Sci. Publ., 132, 225-235
- Met-flow, (2002), *UVP Monitor Model UVP-DUO with Software Version 3, User's Guide*, Lausanne, Switzerland
- Meyer Peter, E., Favre, H., Einstein, A., (1934), Neuere Versuchsergebnisse über den Geschiebetrieb, *Schweiz Bauzeitung*, 103 (13)

- Meyer Peter, E., Müller, R., (1948), *Formulas for bed load transport*, Report on second meeting of international association for Hydraulics Research, Stockholm, Sweden, 1948, pp. 39-64
- Milhous, R.T., Klingeman, P.C., (1973), Sediment transport system in a gravel-bottomed stream, in *Hydraulic Engineering and the Environment Proc. 21st Ann. Hydraulics Div. Spec. Conf. Am. Soc. Civ. Engineers*, Boseman, Montana, 293-303
- Nanson, G.C., (1974), Bed load and suspended load transport in a small, steep, mountain stream, *Am. J. Sci.*, 274, 471-486
- Nezu, I., 2005. Open Channel Flow Turbulence and Its Research Prospect in the 21st Century, *Journal of Hydraulic Engineering*, ASCE, Vol April 2005, 229-246
- Nezu, I., Kadota, A., Nakagawa, H., (1997), Turbulent Structure in Unsteady Depth-Varying Open-Channel Flows, *Journal of Hydraulic Engineering*, 123 (9), pp 752–763.
- Nezu, I., Nakagawa, H., (1993), *Turbulence in open-channel flows*, IAHR Monograph Series, A.A. Balkema Publishers, Rotterdam, The Netherlands
- Papanicolaou, A.N., Diplas, P., Balakrishnan, M., Dancey, C., (1999), Computer vision technique for tracking bed load movement, *Journal of Computing in Civil Engineering*, Vol 13, No 2, pp 71-79
- Parker, G., (1979), Hydraulic geometry of active gravel rivers, *Journal of Hydraulic Engineering*, 105(9), pp 1185-1201.

- Parker, G., (2006), *1D sediment transport morphodynamics with applications to rivers and turbidity currents*, November 14, 2006, from http://vtchl.uiuc.edu/people/parkerg/morphodynamics_e-book.htm
- Plate, E.J., (1994), The need to consider non-stationary sediment transport, *International Journal of Sediment Research*, Vol 9, pp 117-123
- Qu, Z., (2003), *Unsteady Open-Channel Flow over a Mobile Bed*, École Polytechnique Fédérale de Lausanne, Thèse no 2688
- Rao, A.R., E.C.,Hsu, (2008), *Hilbert-Huang Transform Analysis of Hydrological and Environmental Time Series*, Water Science and Technology Library
- Reid, I., Frostick, L., Layman, J.T., (1985), The incidence and nature of bedload transport during flood flows in coarse grained alluvial channels, *Earth Surface Processes and Landforms*, Vol.10, 33-44
- Reid, I., Laronne, B., Powell, D.M., (1995), The Nahal Yatir Bed load database: Sediment dynamics in a gravel-bed ephemeral stream, *Earth Surface Processes and Landforms*, Vol.20, 845-857
- Reid, I., Powell, D.M., Laronne, B., (1996), Prediction of bed-load transport by desert flash floods, *Journal of Hydraulic Engineering*, Vol. 122, No.3, 170-173
- Reid, I., Laronne, J.B., Powell, D.M., (1998), Flash-flood and bedload dynamics of desert gravel-bed streams, *Hydrological Processes*, 12, 543-557
- Rottner, J., (1959), A formula for bed load transportation, *La Houille Blanche*, vol. 14 no 3, pp. 285-307
- Schoklitsch, A., (1935), *Stauraumverlandung und Kolkabwehr*, Julius Springer, Wien

- Shields, A., (1936), *Anwendung der Aenlichkeitsmechanik und der Turbulenzforschung auf die Geschiebebewegung*, Mitteilungen der Preussischen Versuchsanstalt fur Wasserbau und Schiffbau, Berlin, Germany, translated to English by W.P.Ott and J.C. van Uchelen, California Institute of Techonolgy, Pasadena, Calif.,
- Simons D. B., Şentürk F., (1992), *Sediment Transport Technology*, Water Resources Publications, USA
- Tacconi, P., Billi, P., (1987), *Bed load transport measurements by the vortex-tube trap on Virginio Creek, Italy*, In: *Sediment transport in Gravel-Bed Rivers*, (ed. By C. Thorne, J. Bathurst and R. Hey) 583-616. John Wiley, Chichester, UK.
- Tayfur, G., Singh, V.P., (2006), Kinematic wave model of bed profiles in alluvial channels, *Water Resources Research*, 42, W06414
- Tazioli, G.S., (1989), The instrumented basins of Esino and Musone rivers in the Marche regions, Italy, *Proc. 2nd ERB General Meeting*, Perugia, October 1988, Associazione Italiana di Idronomia
- Tsujimoto, T., Mori., A., Okabe. T, Ohmoto, T., (1990), Non-equilibrium sediment transport: a generalized model, *Journal of Hyroscience and Hydraulic Engineering*, 7 (2), 1-25
- Tu, H., (1991), *Velocity distribution in unsteady flow over gravel beds*, École Polytechnique Fédérale de Lausanne, Thèse no 911
- Vanoni, A.V., (2006), *Sedimentation Engineering*, ASCE Manulas and Reports on Engineering Practice No.54, ASCE

- Wong, M., (2003), Does the bed load equation of Meyer-Peter and Müller fit its own data, *Proceedings, 30th Congress, International Association of Hydraulic Research*, Thessaloniki, J.F.K. Competition Volume: 73-80
- Wu, W., Altınakar, M., Wang, S.S.Y., (2006), Depth-average analysis of hysteresis between flow and sediment transport under unsteady conditions, *International Journal of Sediment Research*, Vol 21, No 2, pp 101-112
- Wu, W., Wang, S.S.Y., (2005), Development and Application of NCCHE'S Sediment Transport Models, *US-CHINE Workshop on advanced computational modeling in hydroscience and engineering*, September 19-21, Oxford, Mississippi, USA
- Yang, C.T., (1973), Incipient motion and sediment transport, *Journal of Hyd. Div.*, ASCE, Vol 99, No HY10, Proceeding pp 10067,1679-1704.
- Yang, C.T., (1996), *Sediment Transport*, McGraw-Hill Series in Water Resources and Environmental Engineering, ISBN 0-07-114882-5, Singapore

APPENDIX I

THE DESIGN AND CONSTRUCTION STAGES OF THE SYSTEM

The experimental system consists of

- Rectangular flume of 80 cm width, 75 cm height 18.6 m length, involving a tailgate, stilling basin, Bazin weir and supports at two ends.
- Water supply reservoir (main tank) with a volume of 27 m³ (3mx6mx1.5m).
- Hydrograph tanks (upper and lower hydrograph tanks) involving two engines and propellers, valves and a ladder
- Sediment feeding unit involving a spiral and a motor.
- Line 1 involving pump 1 and valve. The pipe is made of HDPE pipe with a diameter of 160 mm and contains a short metallic part.
- Line 2 involving pump 2, pump speed control unit, flow meter, manometer and valve. The pipe is made of HDPE pipe with a diameter of 160 mm and contains a short metallic part on which the flow meter is mounted.
- Sediment collection system involving sediment baskets and shelves for baskets
- Platform which is 1m wide and 1.8m height with a ladder

A.1 Design and Construction of the System

The rectangular flume is designed as arch type (radius of 25.9 m and angle of 38.3°) with two supports at each end (figure A.1). The skeleton of the flume is made of U140 profiles. The stilling reservoir placed at upstream end has a cross-section of 1.5m x 0.8m and has three layers of perforated metal sheets serving to calm the water.

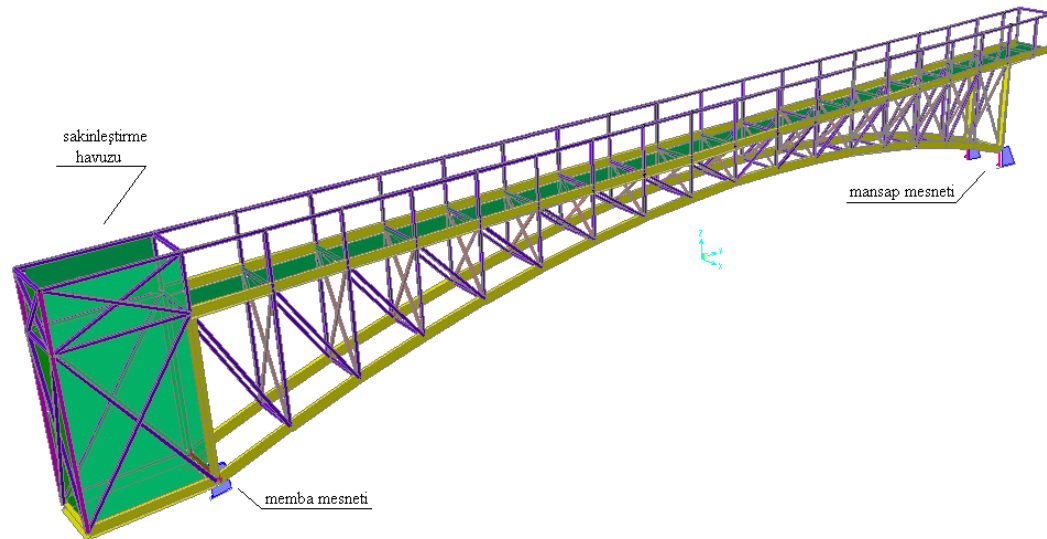


Figure A.1 Rectangular channel

The static calculations are done by SAP2000 program aiming the minimization of the strains as given in figure A.2. The forces at the joint supports are also calculated as given in figure A.3.

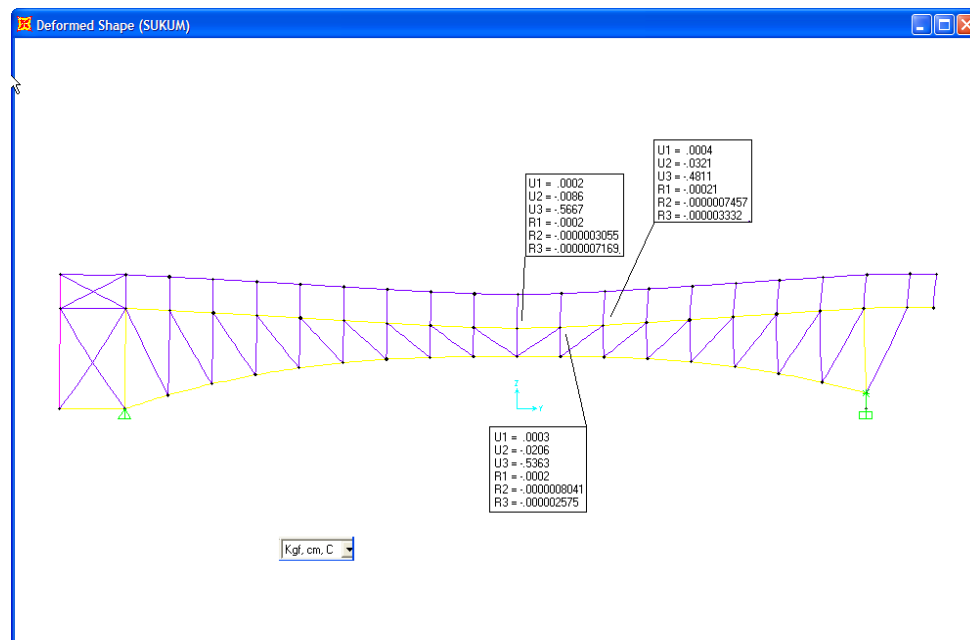


Figure A.2 Strains at the middle of the flume

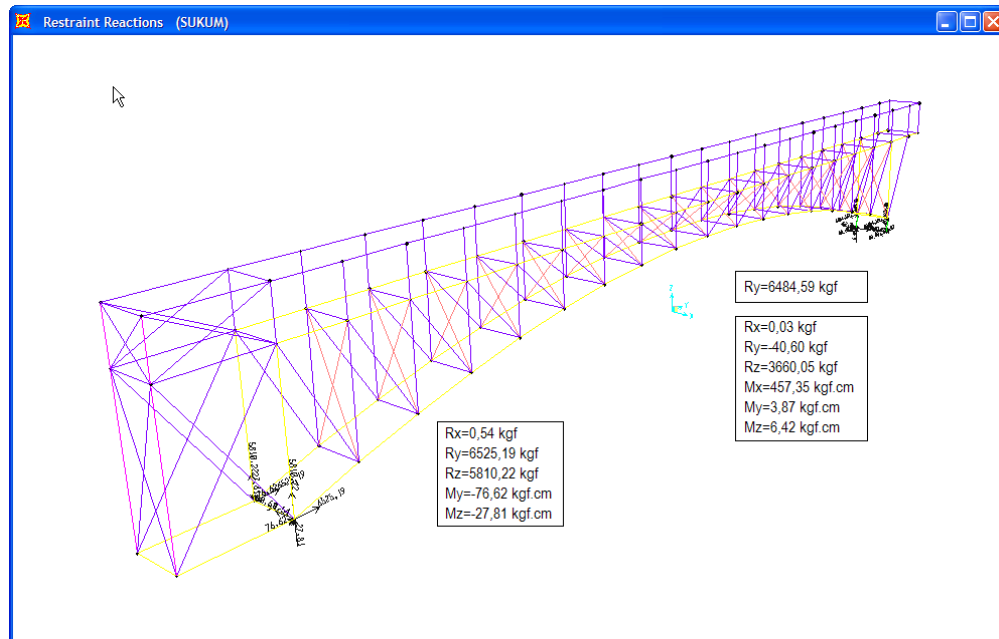


Figure A.3 Forces at the supports of the flume

General layout of the system is given in figure A.4. The design details of the rectangular channel and the main tank are illustrated in figure A.5 and A.6, respectively. The profile types used in the construction of the main tank are given in figure A.7. The design details of the downstream support and upstream support are given in figure A.8 and A.9 respectively. The design details of the Bazin weir and the sediment baskets are illustrated in figure A.10 and A.11, respectively.

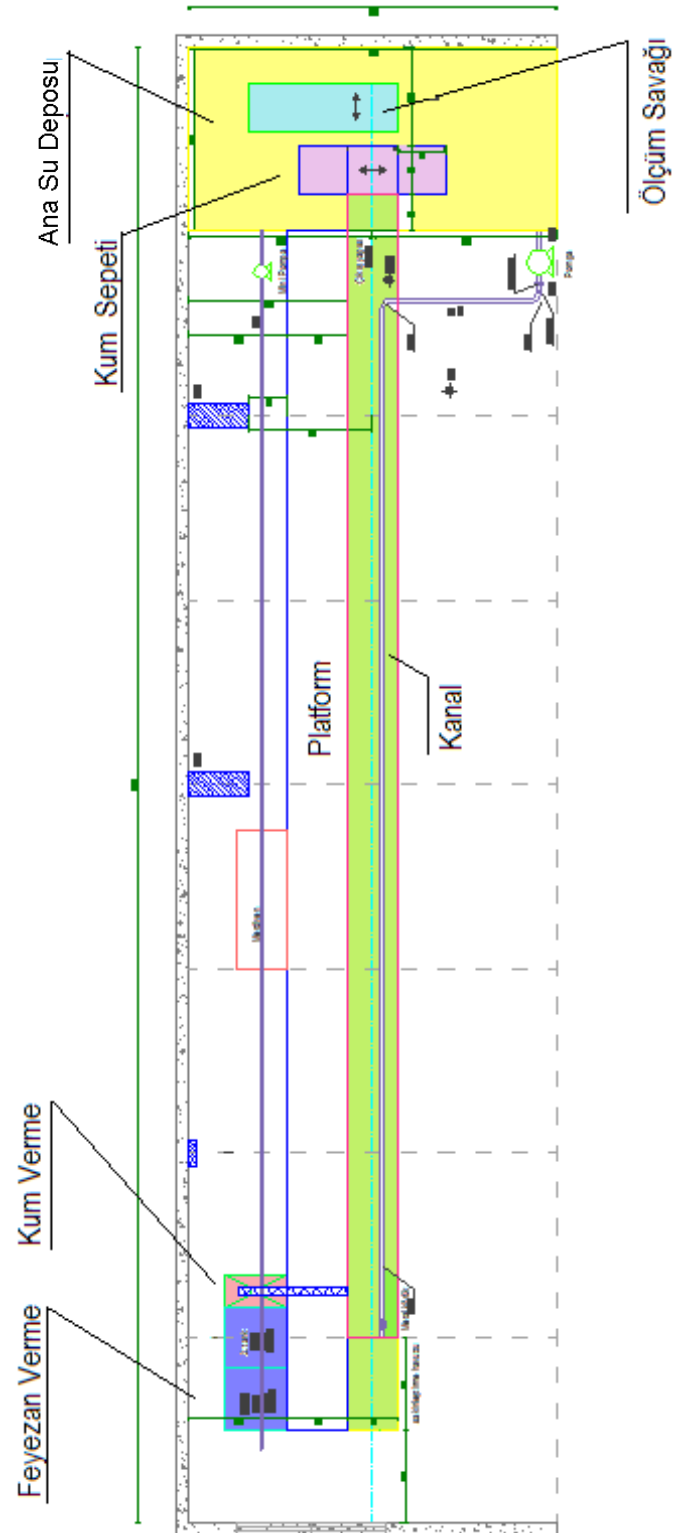


Figure A.4 General layout of the system

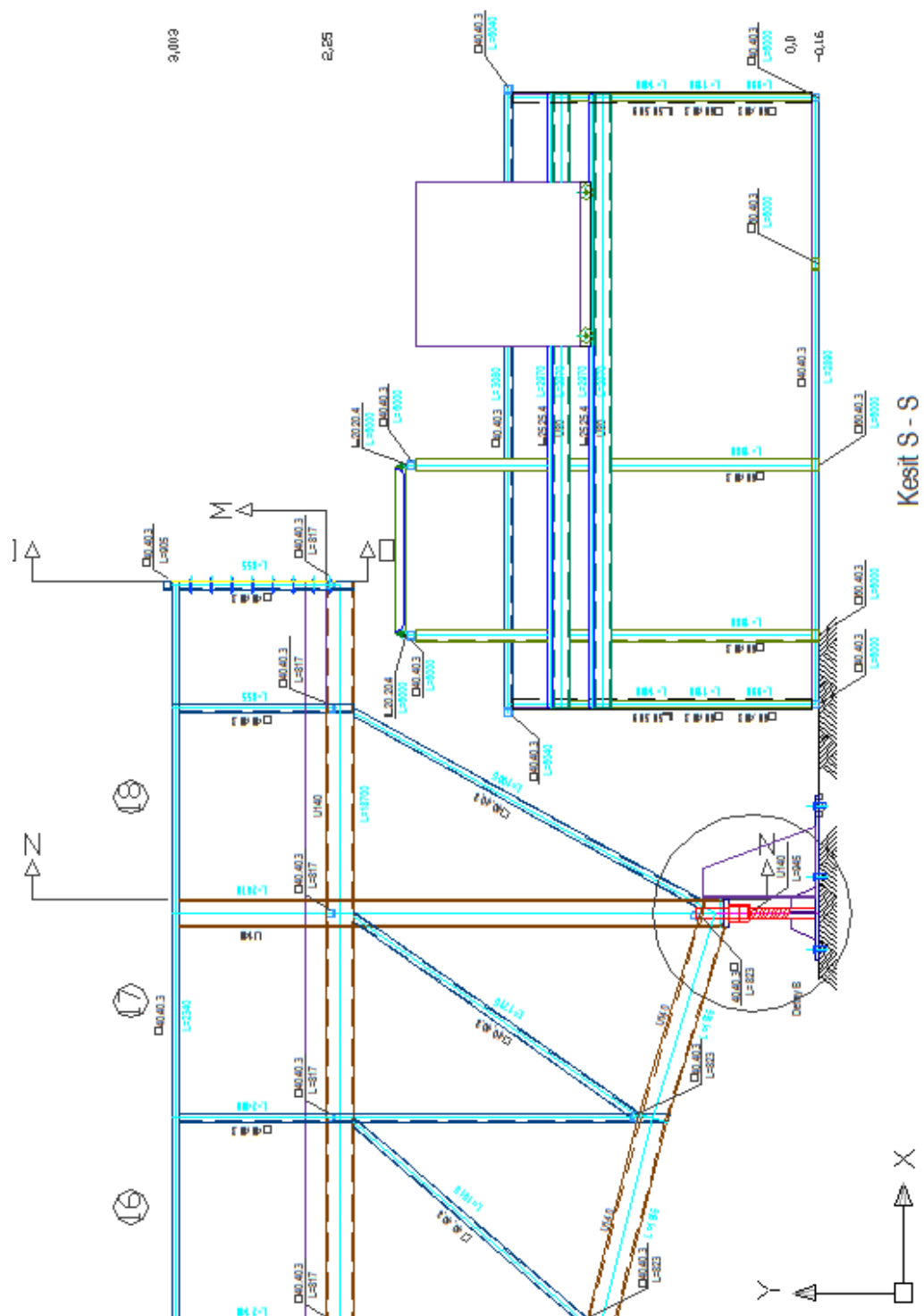


Figure A.5 Design details of the rectangular channel

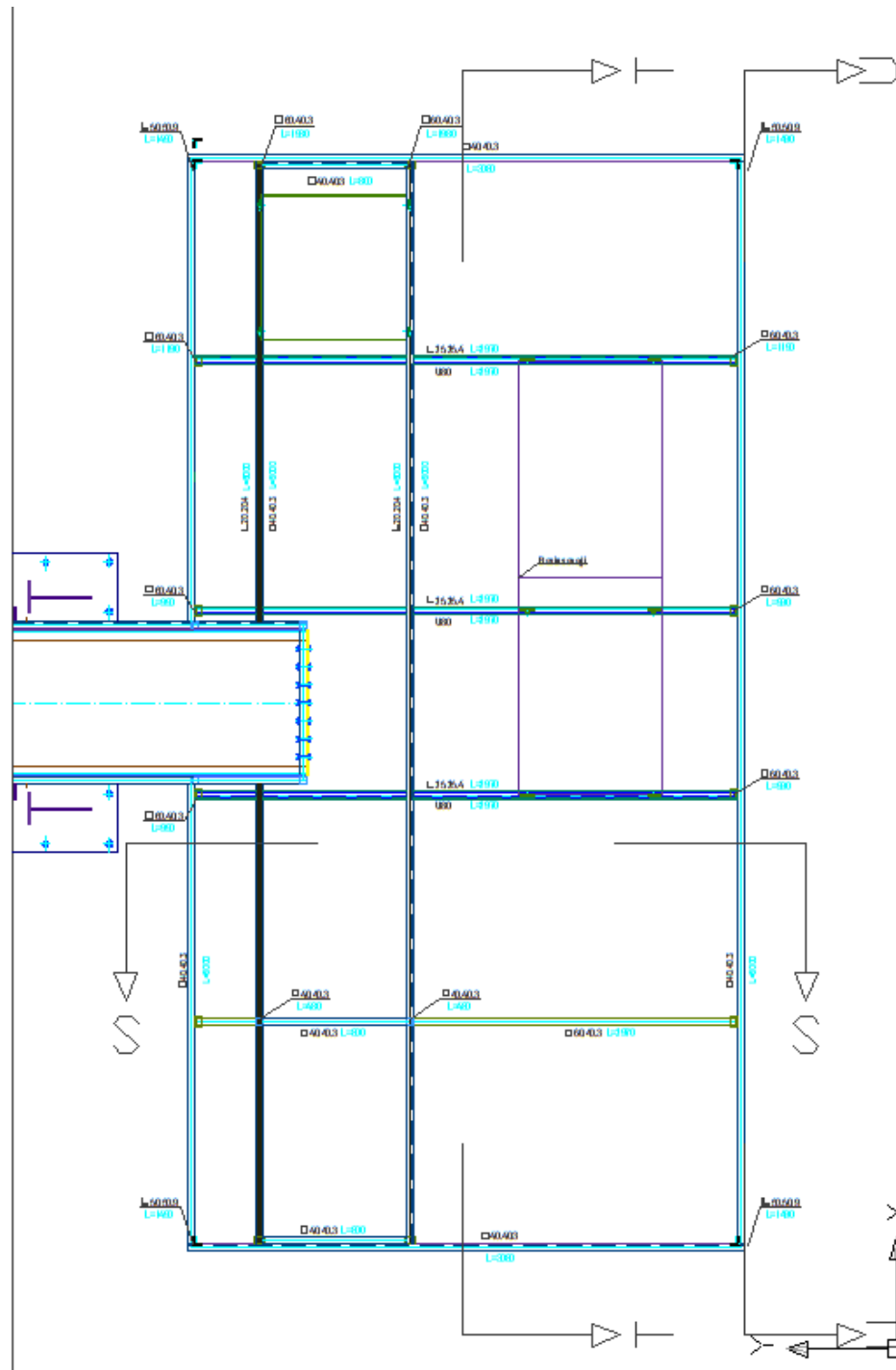


Figure A.6 Design details of the rectangular main tank

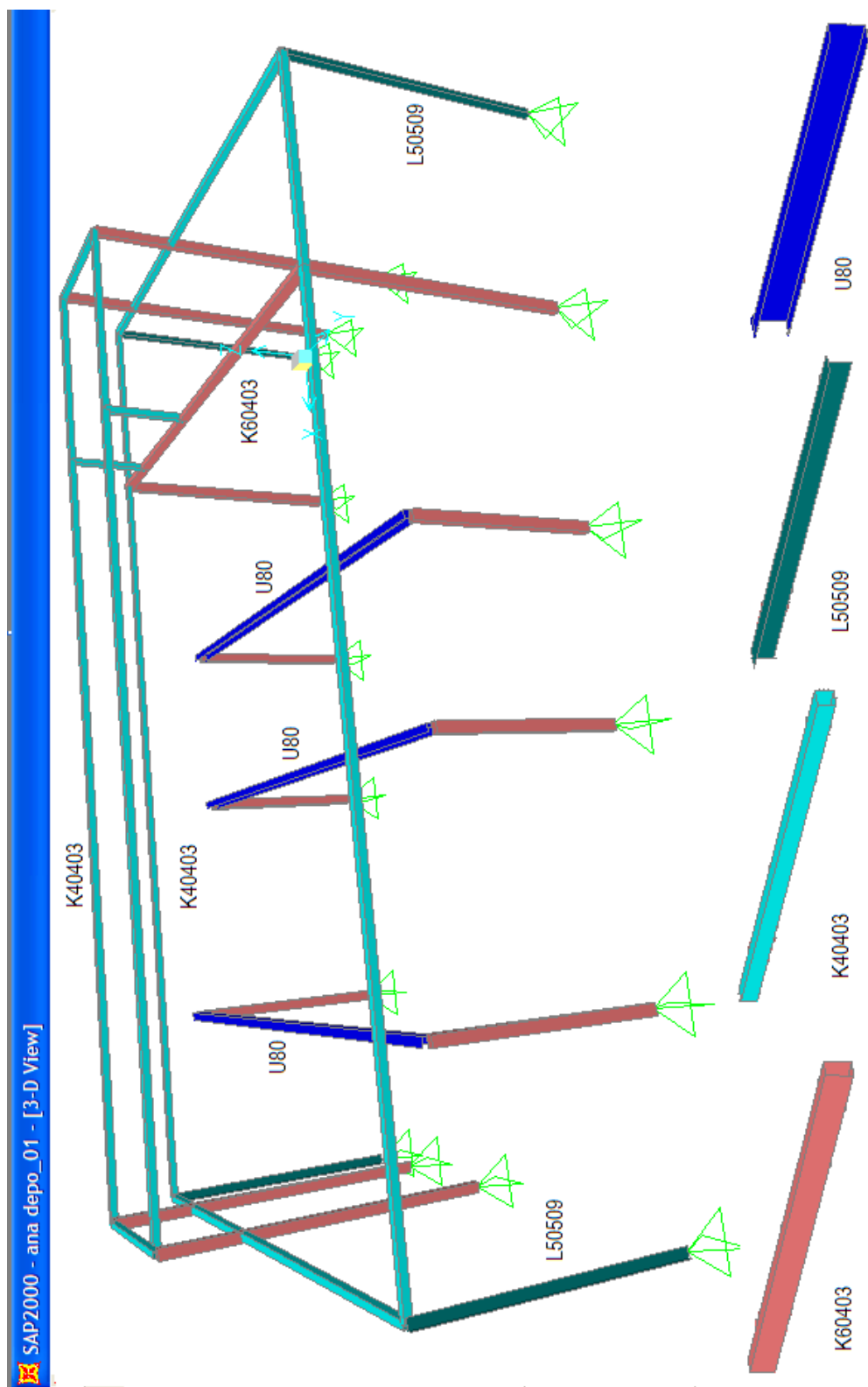


Figure A.7 The profile types used in the construction of the main tank

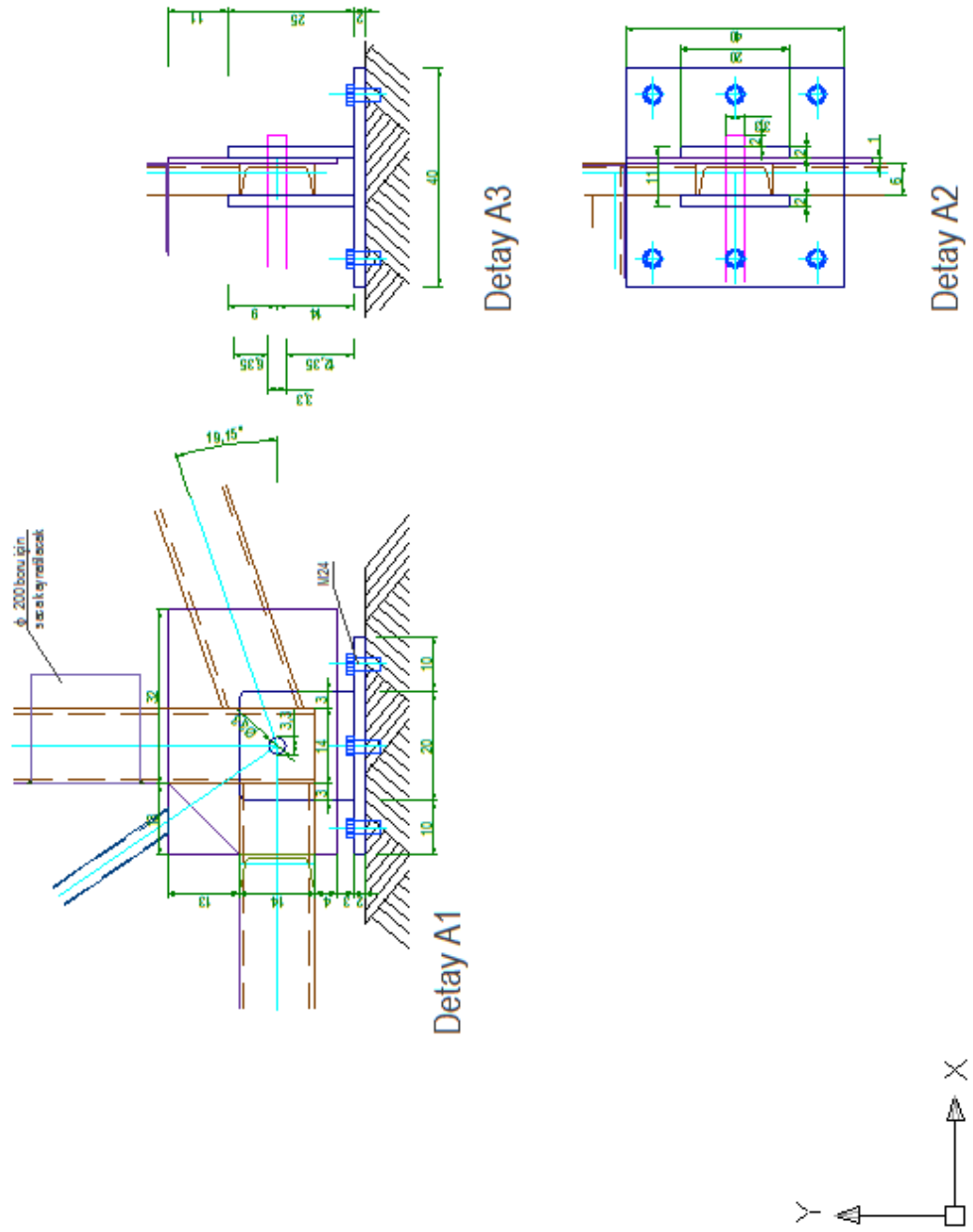


Figure A.8 Design details of the downstream support

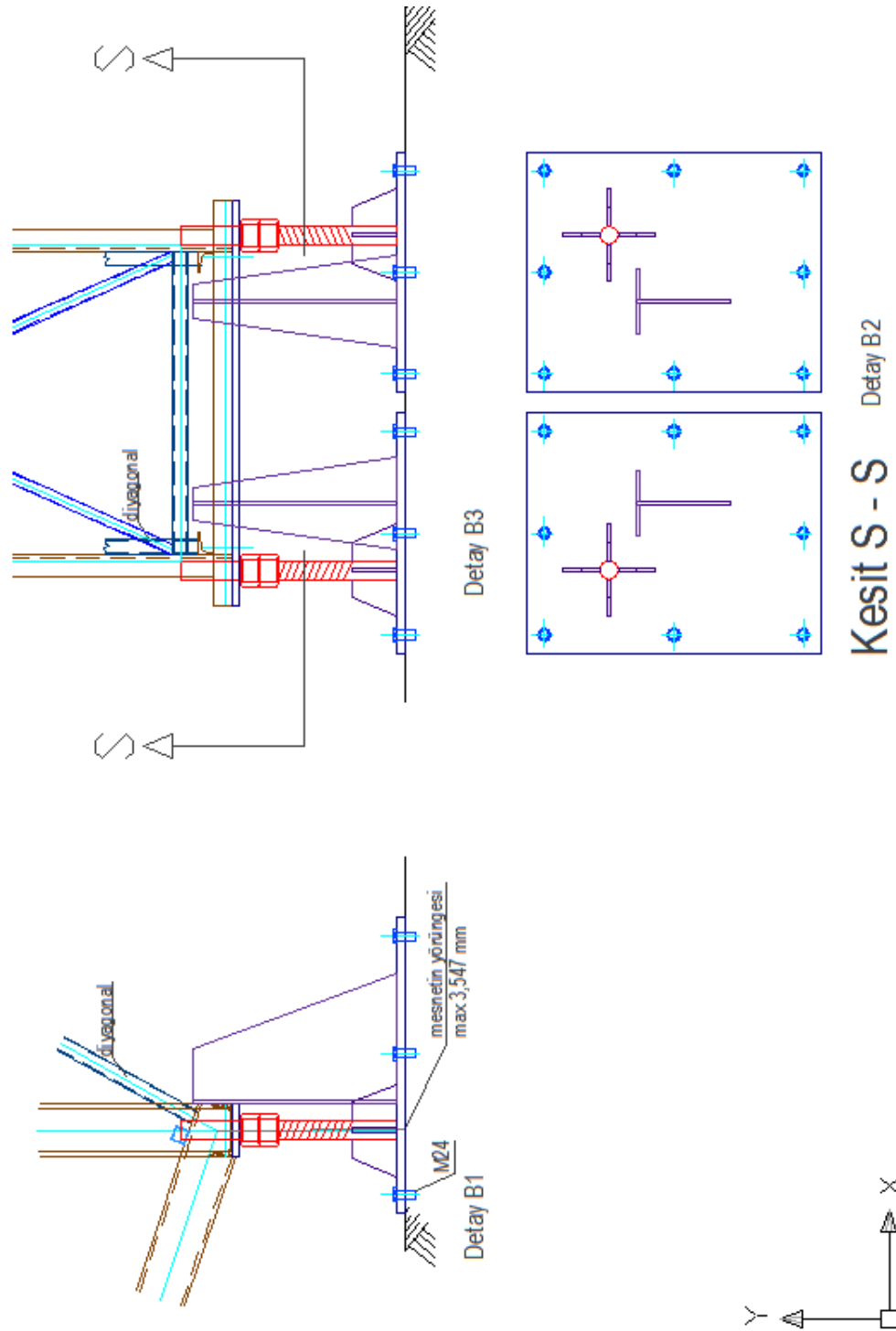


Figure A.9 Design details of the upstream support

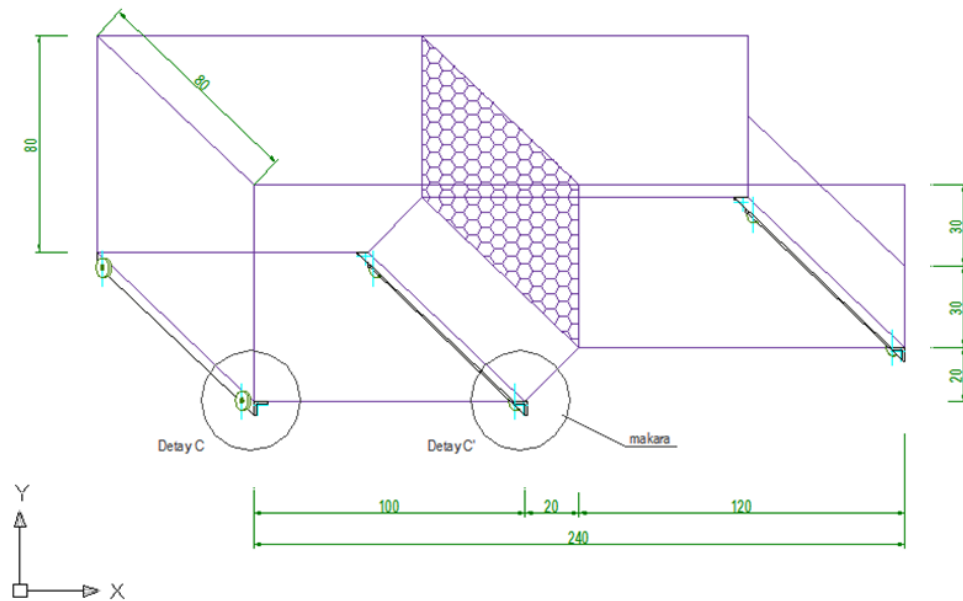
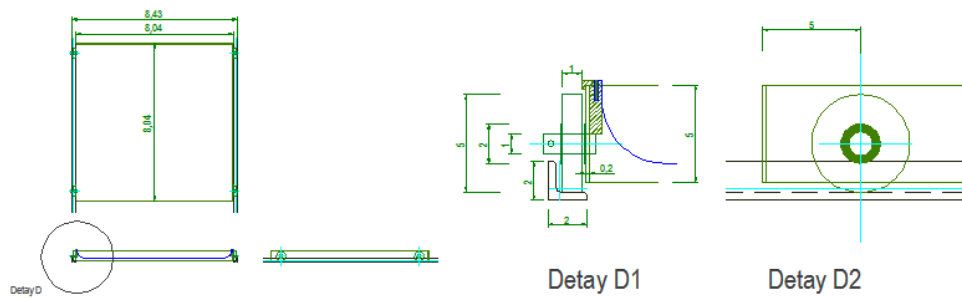


Figure A.10 Design details of the Bazin weir and



Kum Yakalama Sepeti - Dış Çerçeve
(0,80 m x 0,80 m x 0,05 m) x 3

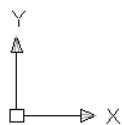


Figure A.11 Design details the sediment baskets

The footing of the flume supports are done in the laboratory (figure A12 to A.15). The skeleton of the channel is constructed by the local manufacturers (figure A.16 to A.18) Assembly of the skeleton of the system is given in figure A.19 to A.23.



Figure A.12 The footing of the flume supports



Figure A.13 The footing of the flume supports



Figure A.14 The footing of the flume supports



Figure A.15 The footing of the flume supports



Figure A.16.a,b,c,d Construction of the skeleton of the channel



Figure A.17 Construction of the skeleton of the channel



Figure A.18 Construction of the skeleton of the channel



Figure A.19 Assembly of the skeleton of the system



Figure A.20 Assembly of the skeleton of the system

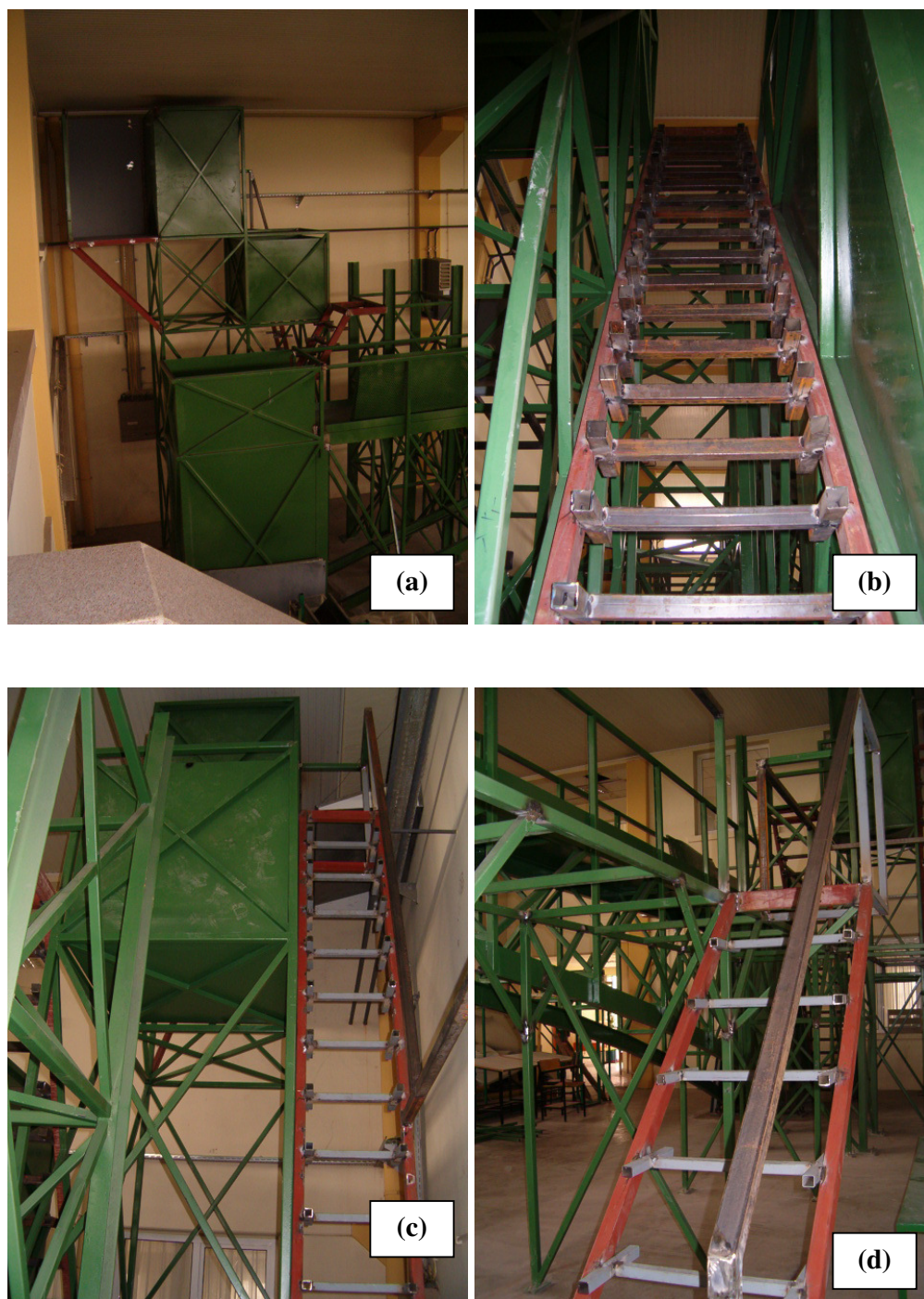


Figure A.21.a,b,c,d Assembly of the skeleton of the system



Figure A.22 Assembly of the skeleton of the system



Figure A.23 Assembly of the skeleton of the system

The transparent Plexiglas sides of the channel are installed as given in figure A.24. The supports of the channel are shown in figure A.25. The tailgate at the downstream end of the channel is shown in figure A.26.

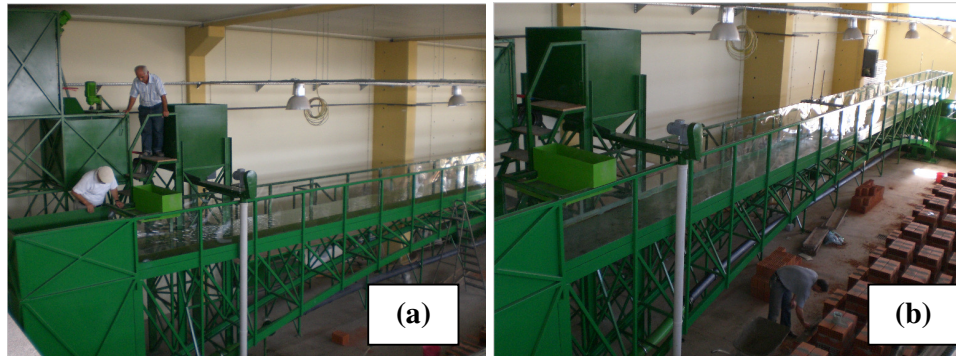


Figure A.24 Installation of plexiglas sides (a) upstream of the system, (b) downstream of the system

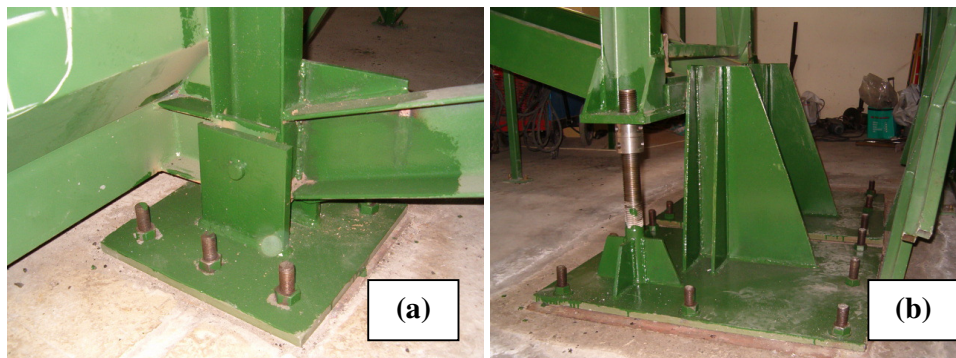


Figure A.25 (a) Upstream support, (b) downstream support

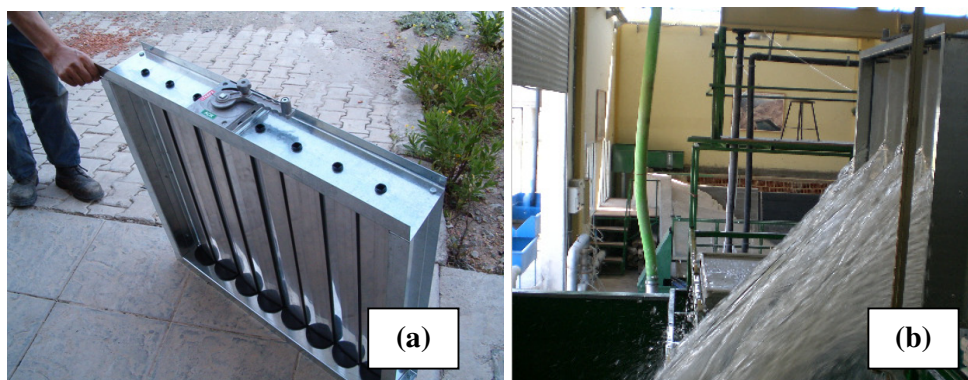


Figure A.26.a and b The tailgate at the downstream of the channel

A.2 Water supply reservoir (main tank)

The base area of the main tank is 3m x 6m (18 m²) and height is 1.5m with a volume of 27 m³. The design of the main tank is given in figure A.27 and the finished product is given in figure A.28.

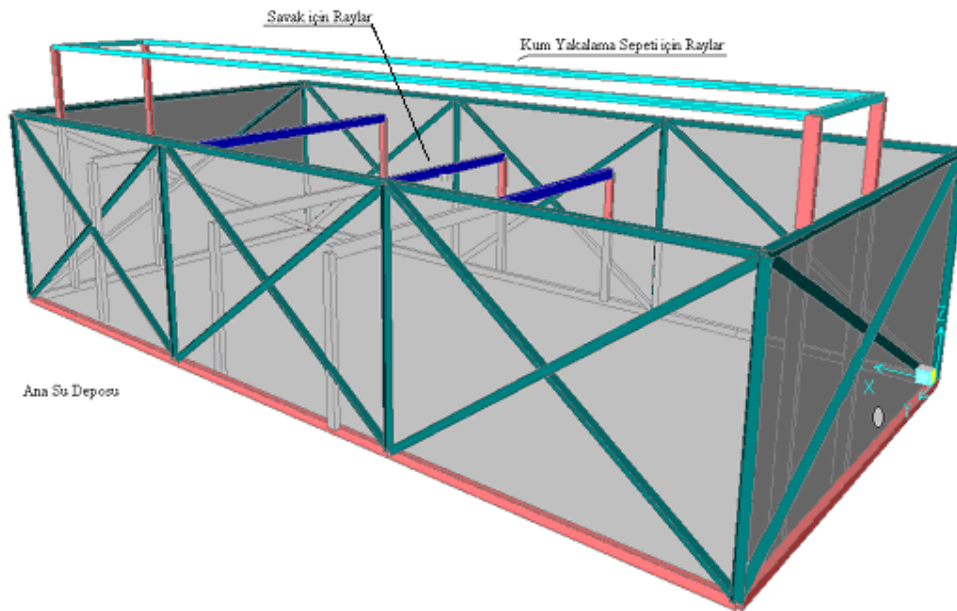


Figure A.27 Design of main tank



Figure A.28 Installation of main tank

A.3 Upper and lower hydrograph tanks

In order to obtain the hydrograph, an elaborate experimental tool involving two elevated tanks (hydrograph tanks) is designed. The upper hydrograph tank ($1,5\text{m}^3$) may be filled with both water and sediments, while the lower tank (1m^3) is kept empty (figure A.29). Sudden opening of the valve at the outlet of the upper tank will result in an increase in the water height in the lower basin and then a gradual decrease. The hydrograph is obtained at the outlet of the lower basin. This method is tested with clear water and gave satisfactory results (Güney et.al., 2008). The so-obtained hydrograph is similar to that encountered in nature.

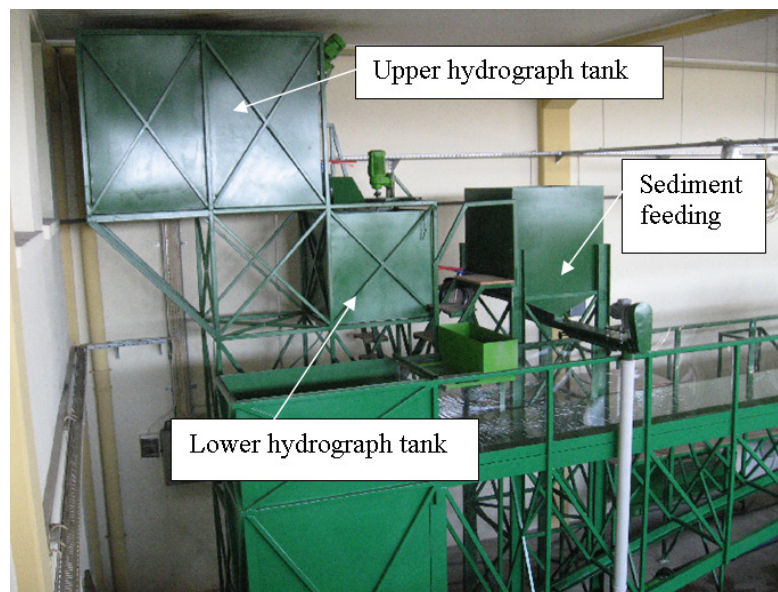


Figure A.29 Upper and lower hydrograph tanks

Each hydrograph tank involves two engines and propellers and valves as given in figure A.30.a and A.30.b, respectively. The design of the tanks and the ladder is shown in figure A.31. The upper hydrograph tank is fed by the pump shown in figure A.32.a from the main tank. The control panel of the pump is shown in figure A.32.b.

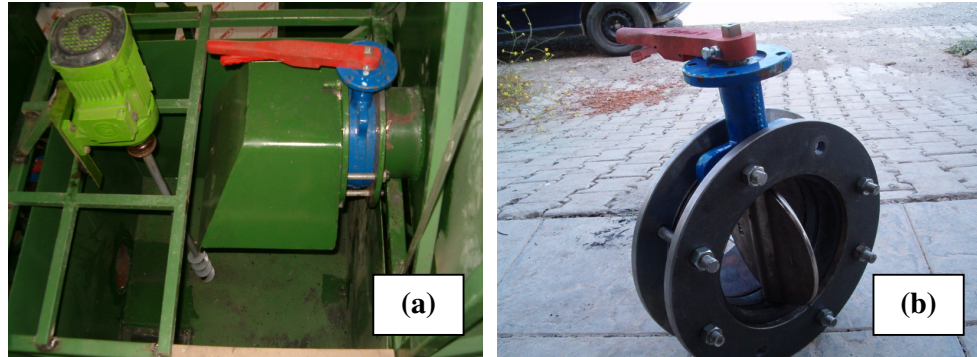


Figure A.30 (a) Engine and propeller, (b) valve

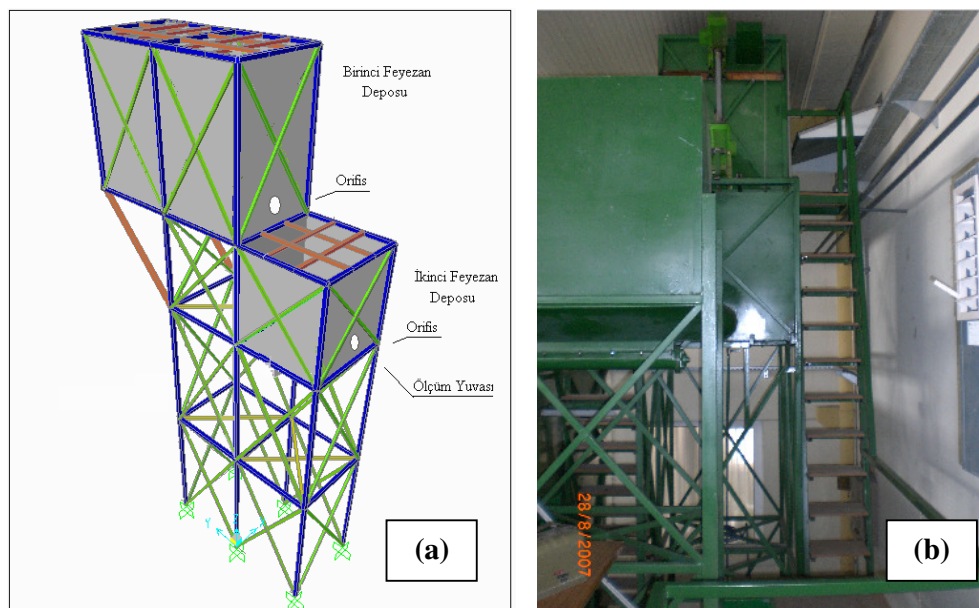


Figure A.31 (a) Design of hydrograph tanks, (b) ladder to hydrograph tanks

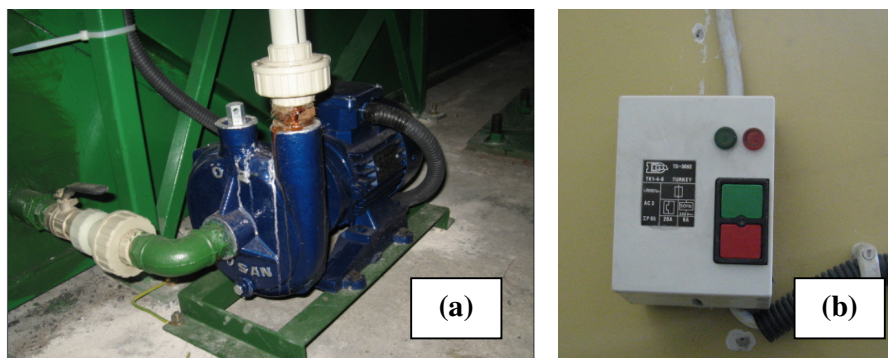


Figure A.32 (a) Pump, (b) pump control panel

A.4 Sediment Feeding Unit

The sediment feeding unit consists of a sediment reservoir with a volume of 1 m^3 , a spiral and a motor (figure A.33).

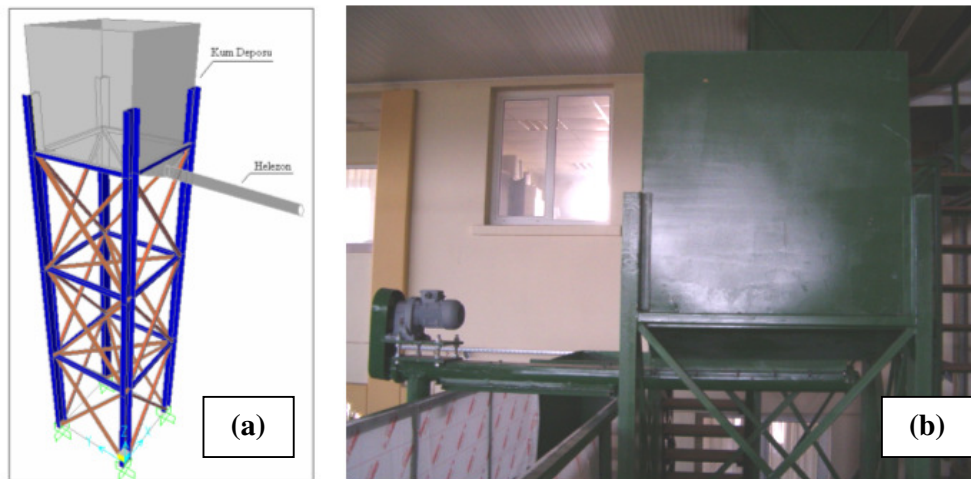


Figure A.33 (a) design of sediment feeding unit, (b) spiral and a motor

A.5 Pipe Lines

There are two lines in the system as given in figure A.34.

- Line 1 involving pump 1 and valve. The pipe is made of HDPE pipe with a diameter of 160 mm.
- Line 2 involving pump 2, pump speed control unit, flow meter, manometer and valve. The pipe is made of HDPE pipe with a diameter of 160 mm.

At each line there are two pumps.

- The Pump 1 is a common centrifugal pump whose capacity is 30 l/s, 1450 rpm, 13 kW, figure A.35.a.
- The Pump 2, having the maximum capacity of 100 l/sec, 1450 rpm, 18.5 kW, figure A.35.b.

Pump 2 is connected to pump rotational speed control unit which can control the flow rate by adjusting the settings. It is also possible to program the device in order to generate triangular or trapezoidal shaped hydrographs (Figure A.36).

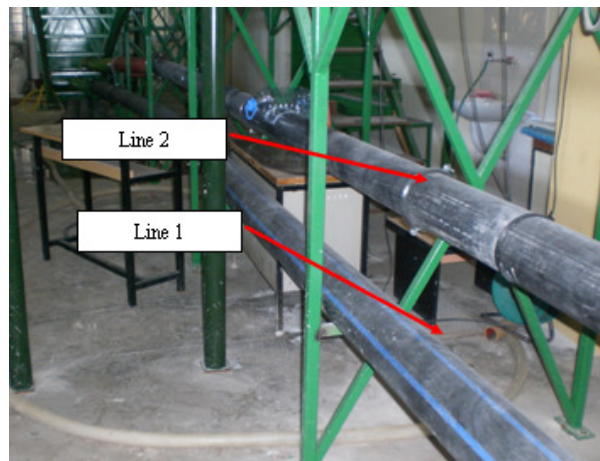


Figure A.34 Two lines in the system

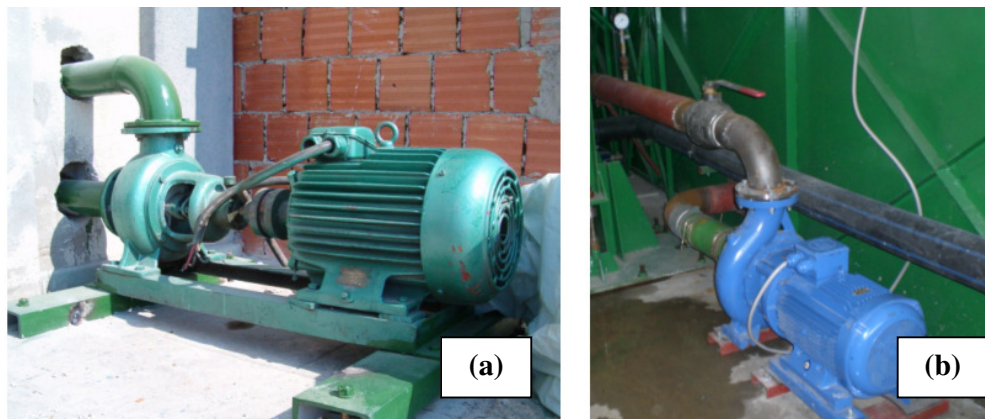


Figure A.35 (a) Pump 1, (b) Pump 2

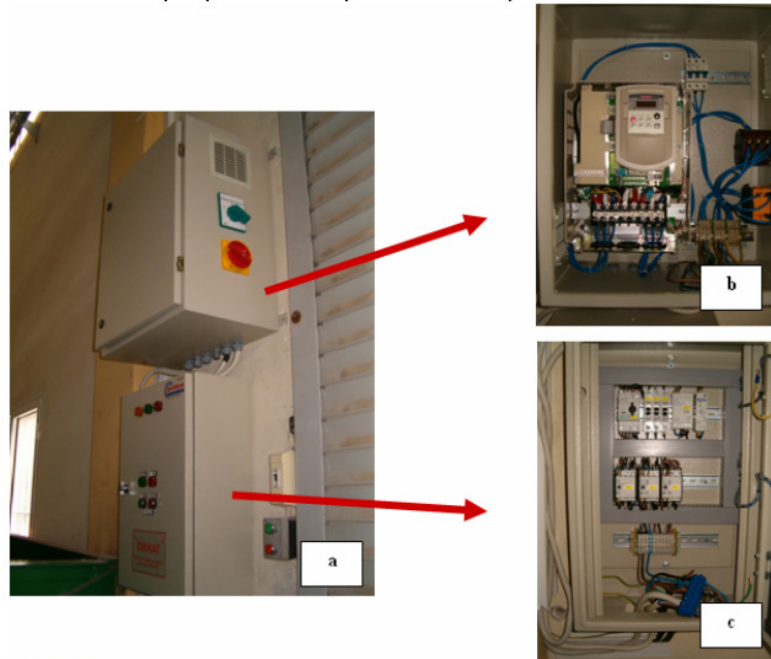


Figure A.36 (a) Control panels of Pump 1 and Pump 2, (b) The pump speed control unit for pump 2, (c) the control panel of pump 1

A.6 Sediment collection system

The sediment baskets have dimensions 80 cm by 80 cm by 5 cm (figure A.37.a). There are totally 60 baskets. The shelves for the baskets are given in figure A.37.b.

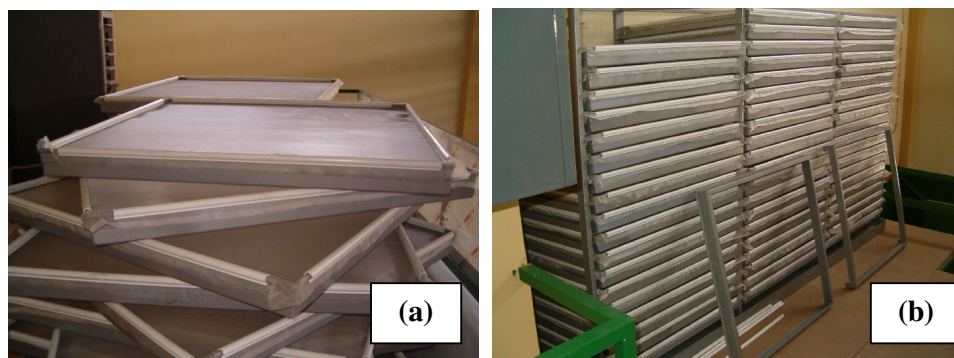


Figure A.37 (a) Sediment baskets, (b) shelves for sediment baskets

A.7 Platform

The platform is 1m wide and 1.8m height. Its length is same as the channel. One can reach to the platform by the ladder (Figure A.38).



Figure A.38 Platform

The general view of the system during the experiments is given in figure A.39.a and A.39.b.

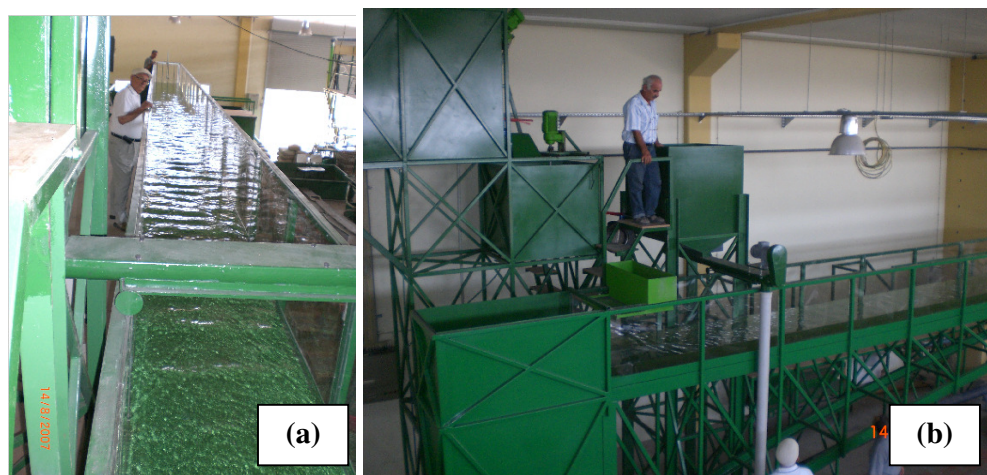


Figure A.39.a, b The system during the experiments

APPENDIX II
THE ULTRASONIC VELOCITY PROFILER AND ITS TRANSDUCERS

The UVP is used with the transducers given in figure B.1. The frequency, length of the transducers and the number of the available transducers are given in Table B.1.



Figure B.1 UVP transducer

Table B.1 The properties of the available transducers

Emitting frequency	Length of the transducer cable (m)	Number of available transducers
0,5 MHz	4	1
1 MHz	4	1
2 MHz	4	1
4 MHz	4	4
4 MHz	8	3

UVP transducers can be used in pipe provided that the pipe material is HDPE by using an ultrasonic gel as shown in figure B.2.a.

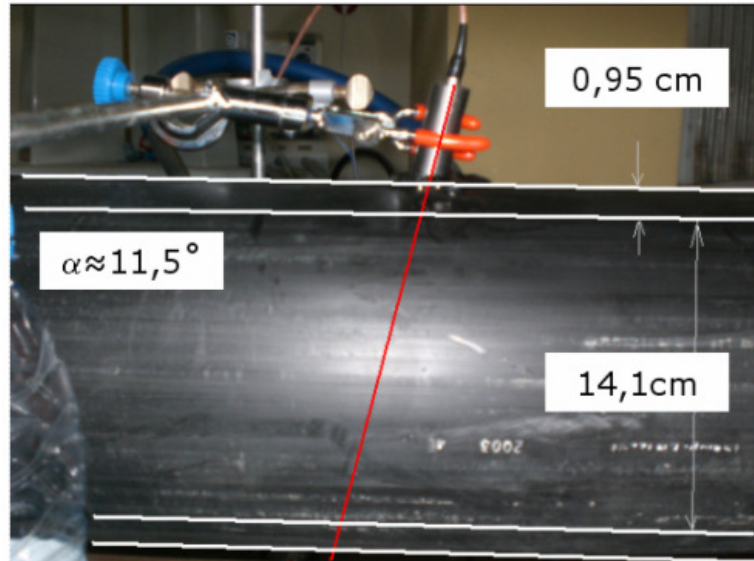


Figure B.2 UVP transducers measuring the flow in pipe

Multiple transducers can also be used in open channels as in the configuration given in figure B.3.



Figure B.3 a, b Different configurations of UVP transducers in open channel

Before each experiment, one should check the measurement parameters as given in figure B.4. The detailed explanation of UVP and its transducers is given in Met-Flow UVP Users Guide.

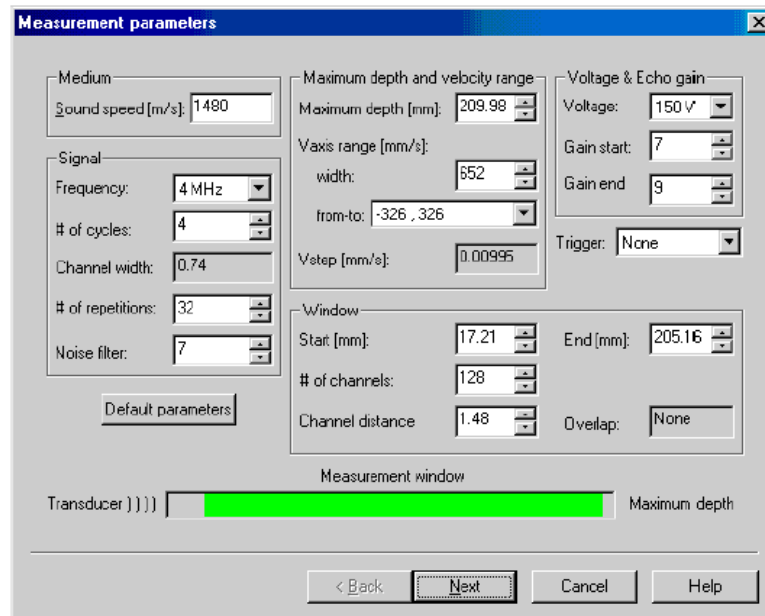


Figure B.4 Measurement parameters window

Medium:

Sound speed: It is the sound speed in the medium (water)

Signal:

Frequency: It is the frequency of the transducer

Number of cycles: The number of waves to be emitted at one time. The cases with 4 and 2 cycles are illustrated in figure B.5.

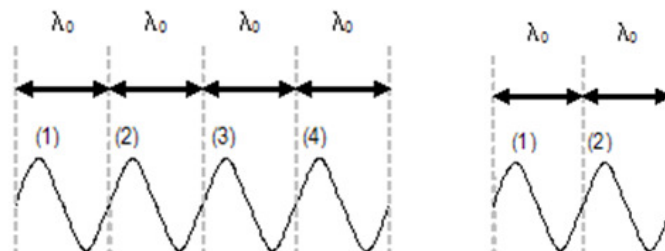


Figure B.5 Description of number of cycles

Channel width: The fictitious channel width as depicted in figure B.6. It is calculated by the software from equation B.1.

$$w = c \lambda_0 \quad (\text{B.1})$$

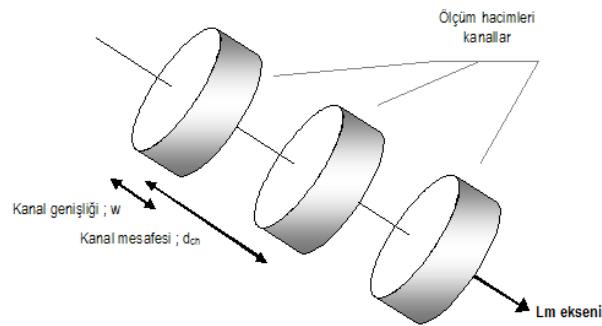


Figure B.6 The measurement channels

Number of repetitions: N_{rep} , It is the number of emissions in order to determine one velocity profile. The more the repetitions, the less the temporal resolution. It determines the total measuring time.

Noise filter: A filter inside the software

Maximum depth and velocity range:

Maximum depth: It is the maximum measurable depth. P_{max} is given in equation B.2.

$$P_{max} = \frac{c}{2F_{pf}} = \frac{cT_{pf}}{2} \quad (\text{B.2})$$

Velocity range: It is the velocity range that the UVP will be able to measure, V_{range} as given in equation B.3. For every transducer, the $P_{max} \times V_{range}$ value is constant, as given in equation B.4.

$$V_{range} = \frac{cF_{prf}}{2f_0} \quad (B.3)$$

$$P_{max} \times V_{range} = \frac{c^2}{4f_0} \quad (B.4)$$

Window:

The measurement window is depicted in figure B.7.

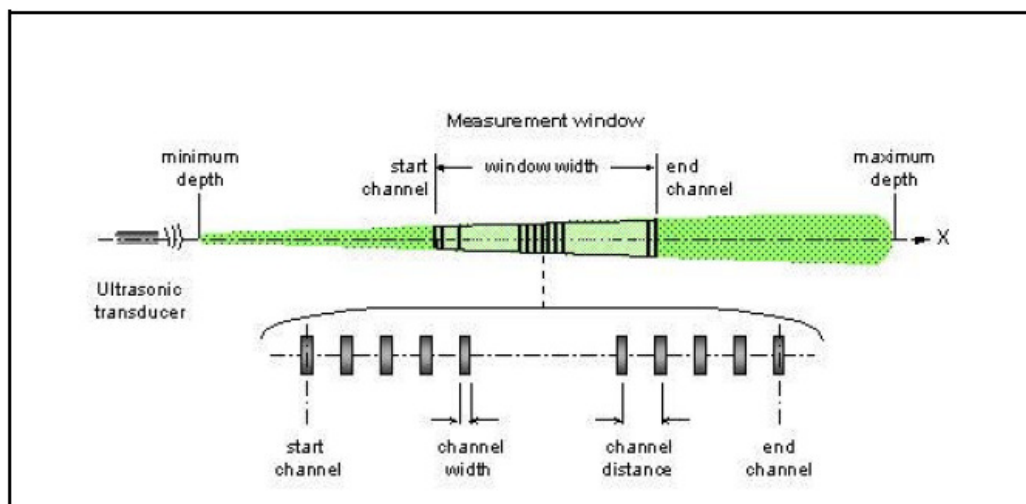


Figure B.7 Illustration of term connected with “measuring window”

Start: The point where the first channel is located

End: The point where the last channel is located

Number of channel: It is the number of channels between start and end channels. The more the number of channels, the less the spatial resolutions as given in figure B.8.

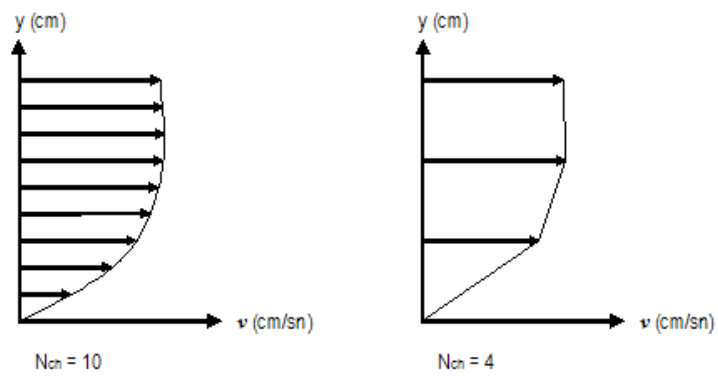


Figure B.8 Spatial resolution

Channel distance: It is the distance between measurement channels as shown in figure B.9.

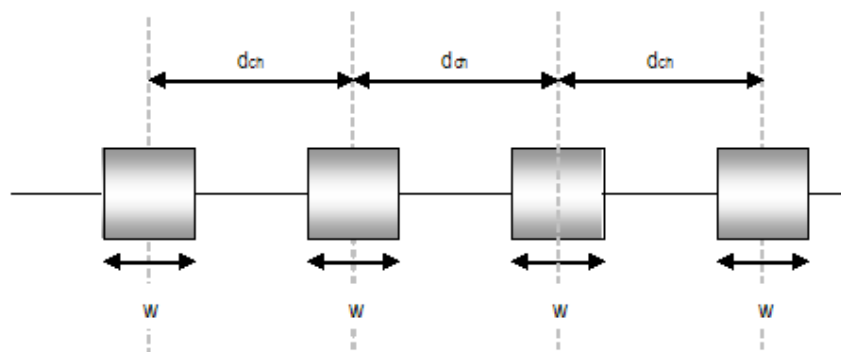


Figure B.9 The distance between measurement channels

Measuring time:

The pulse repetition frequency, F_{prf} and the time corresponding to pulse repetition frequency, T_{prf} can be calculated from the equations B.5 and B.6.

$$F_{prf} = \frac{c}{2.P_{max}} \quad (B.5)$$

$$T_{prf} = \frac{1}{F_{prf}} \quad (B.6)$$

Defining the number of repetitions and the pulse repetition frequency, the total measuring time, T_{meas} , can be calculated as given in equation B.7 and as shown in figure B.10.

$$T_{meas} = N_{rep} \times T_{prf} \quad (B.7)$$

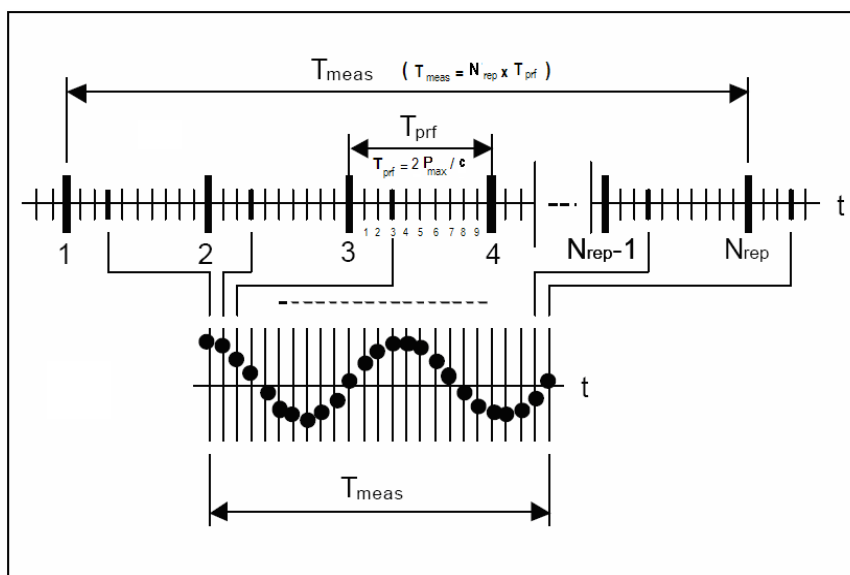


Figure B.10 Establishment of Doppler shift frequency for a single channel

APPENDIX III

PUMP SPEED CONTROL UNIT SOFTWARE

The software of the pump speed control unit is “Drivelink – C” (figure C.1).

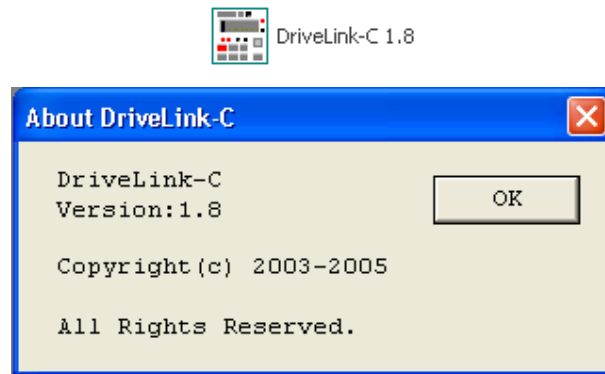


Figure C.1 Drivelink-C software shortcut

In order to start a program;

1. Connect the computer to the pump speed control unit,
2. Run the “Drivelink – C”
3. Open the desired file
4. From “Operation” menu, click to “Link” (figure C.2)
5. Select the COM port (figure C.3)
6. Click to “Link”
7. From “Operation” menu, click to “Write” (figure C.4)
8. Click “Run”

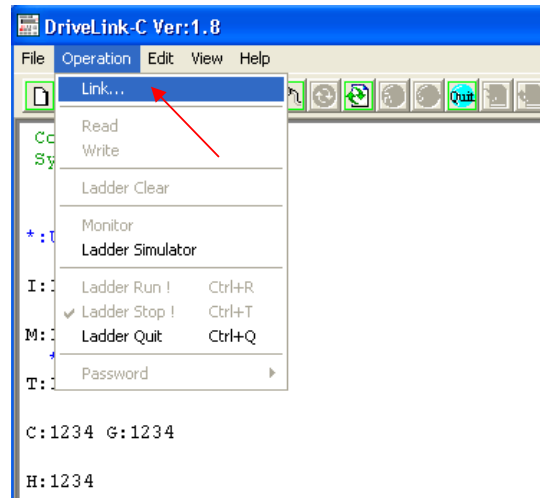


Figure C.2 Link to pump speed control unit

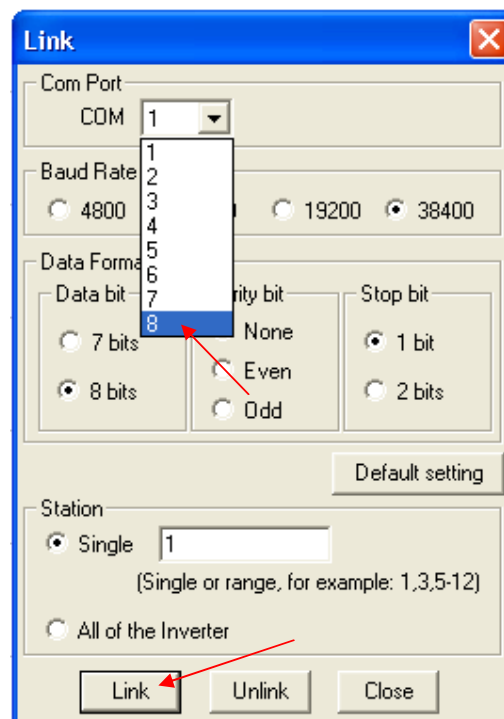


Figure C.3 Selection of COM port to link to pump speed control unit

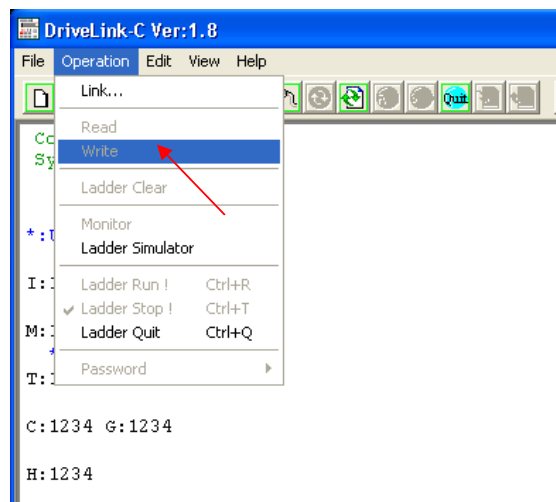


Figure C.4 Write the program to pump speed control unit

The constant pump rotational speed can be achieved by changing the n value as given in figure C.5 by the “Edit Contact/Coil” window as depicted in figure C.6.

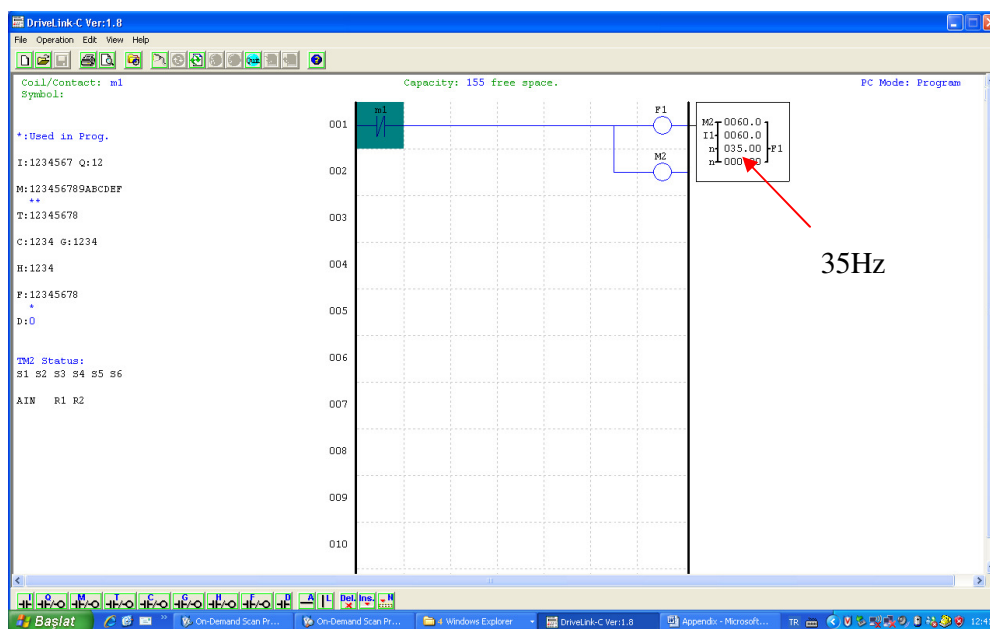


Figure C.5 Changing the n value

The image shows a software window titled "Edit Contact/Coil" with a blue title bar and a close button. The window contains several configuration sections:

- Navigation:** A tabbed interface with tabs labeled T, C, G, H, and F. The F tab is currently selected.
- Select Coil NO.:** A dropdown menu showing "1" with "(1~8)" next to it.
- Output Type:** Four radio buttons labeled I, V, P, and another P.
- Function:** A "Mode" dropdown menu with "No Mode" displayed below it.
- Acc/Dec time:** Two input fields, both containing "0060.0", separated by a "/" and followed by "Sec".
- Set freq.:** A dropdown menu showing "N" followed by "-->" and an input field containing "035.00 Hz".
- Seg freq.:** A dropdown menu showing "N" followed by "-->" and an input field containing "000.00 Hz".
- FWD/REV:** A section with two dropdown menus. The first is labeled "Contact" and shows "M" with "2" next to it.
- Terminal Control:** A section with two dropdown menus. The first is labeled "Contact" and shows "I" with "1" next to it.

At the bottom of the window are two buttons: "OK" and "Cancel".

Figure C.6 "Edit Contact/Coil" window

In order to generate a triangular or trapezoidal shaped hydrograph by the software, the variables $T1$, a_1 , d_1 , $H1$, $T2$, a_2 , d_2 , $H2$, $T3$ are calculated by using the equations C.1 to C.7 which are explained in figure C.7, provided that the values of t_1 , t_3 , t_5 and t_7 are selected.

$$t_1 = a_1 * \frac{H1}{H \max} \quad (C.1)$$

$$t_2 = T1 - t_1 \quad (C.2)$$

$$t_3 = a_2 * \frac{H2 - H1}{H \max} \quad (C.3)$$

$$t_4 = T2 - t_3 \quad (C.4)$$

$$t_5 = a_2 * \frac{H2 - H1}{H \max} \quad (C.5)$$

$$t_6 = T3 - t_5 \quad (C.6)$$

$$t_7 = d_1 * \frac{H1}{H \max} \quad (C.7)$$

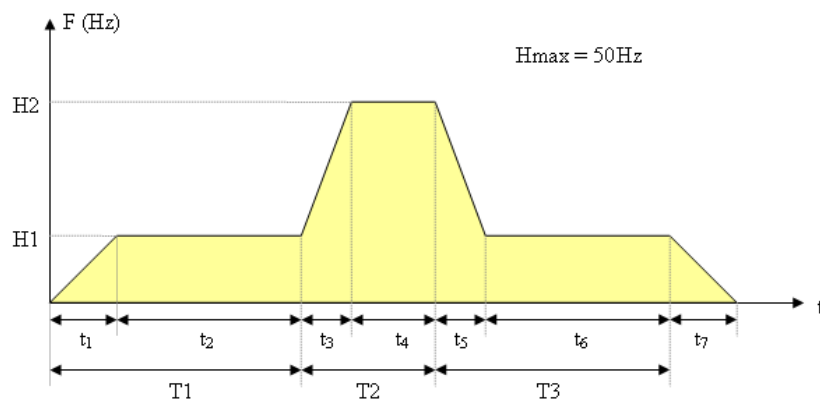


Figure C.7 Variables of the triangular or trapezoidal shaped hydrograph

The a_1 , d_1 , $H1$ are in F1 window and a_2 , d_2 , $H2$ are in F2 window.

Example (Hid-04)

An example of hydrograph is explained below with notations shown in figure C.8.

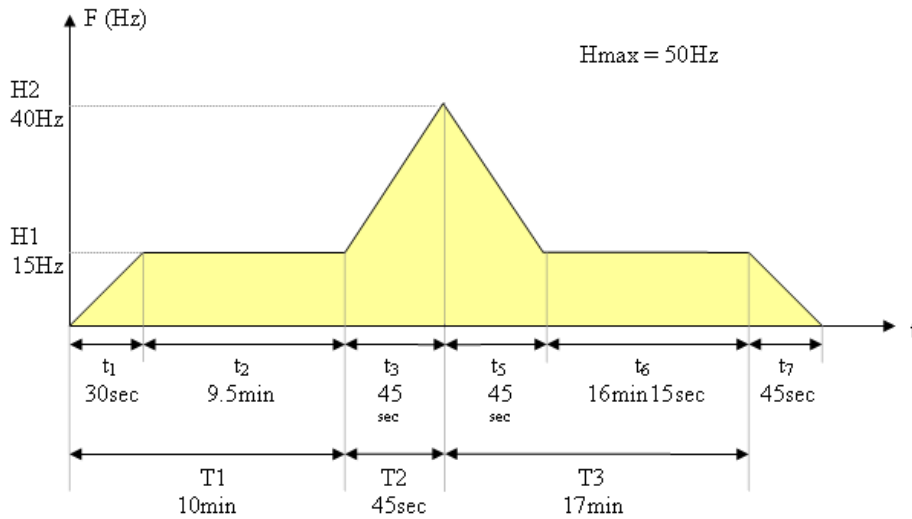


Figure C.8 Variables of the triangular or trapezoidal shaped hydrograph

The relevant calculations are as follows:

$$t_1 = a_1 * \frac{H1}{H \max} = 100 * \frac{15}{50} = 30 \text{ sec}$$

$$t_2 = T1 - t_1 = 10 \text{ min} - 30 \text{ sec} = 9.5 \text{ min}$$

$$t_3 = a_2 * \frac{H2 - H1}{H \max} = 90 * \frac{(40 - 15)}{50} = 45 \text{ sec}$$

$$t_4 = T2 - t_3 = 45 - 45 = 0$$

$$t_5 = a_2 * \frac{H2 - H1}{H \max} = 90 * \frac{(40 - 15)}{50} = 45 \text{ sec}$$

$$t_6 = T3 - t_5 = 17 \text{ min} - 45 \text{ sec} = 16 \text{ min } 15 \text{ sec}$$

$$t_7 = d_1 * \frac{H1}{H \max} = 150 * \frac{15}{50} = 45 \text{ sec}$$

As a result of these calculations, the T1, F1, F2, T2 and T3 given in Table C.1, are loaded as shown in figure C.9 with their windows given in figures C10 to C14.

Table C.1 The parameters, variables and their values

Parameter	Variable and its value
T1	10min
F1	$a_1 = 100$ $d_1 = 150$ $H1 = 15\text{Hz}$
T2	45sec
F2	$a_2 = 90$ $d_2 = 150$ $H2 = 40\text{Hz}$
T3	17min

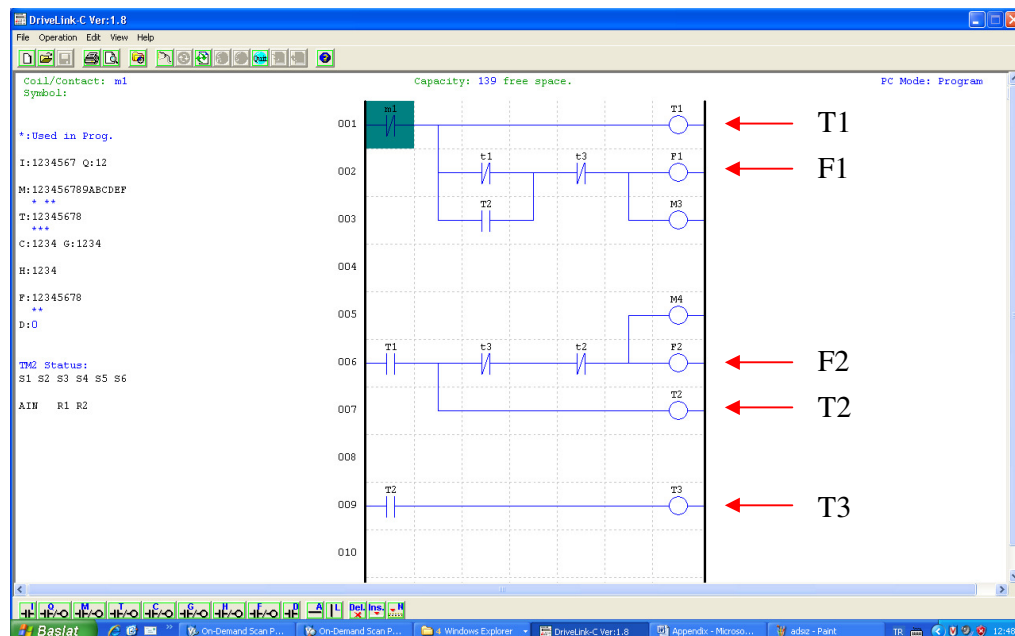
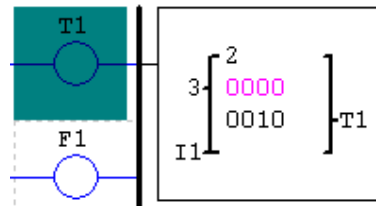


Figure C.9 Variables to be clicked in the Drivelink-C



Edit Contact/Coil

Select Coil NO.: T 1 (1-8) Output Type: I C P

Function: Mode 2 (1-7) On-delay timer mode 2

Time Base: 1 Min

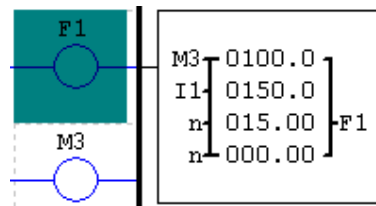
Current value: 0000 Min

Preset value: 0010 Min

Direction Set: Contact Reset Input: Contact I 1

OK Cancel

Figure C.10 T1 window and the parameters



Edit Contact/Coil

Select Coil NO.: F 1 (1-8) Output Type: I C P

Function: Mode No Mode

Acc/Dec time: 0100.0 / 0150.0 Sec

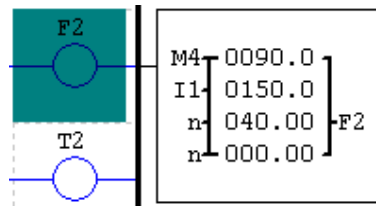
Set freq.: N --> 015.00 Hz

Seg freq.: N --> 000.00 Hz

FWD/REV: Contact H 3 Terminal Control: Contact I 1

OK Cancel

Figure C.11 F1 window and the parameters



Edit Contact/Coil

Select Coil NO.: F 2 (1-8) Output Type: I C P

Function: Mode No Mode

Acc/Dec time: 0090.0 / 0150.0 Sec

Set freq.: N --> 040.00 Hz

Seg freq.: N --> 000.00 Hz

FWD/REV: Contact H 4 Terminal Control: Contact I 1

OK Cancel

Figure C.12 F2 window and the parameters

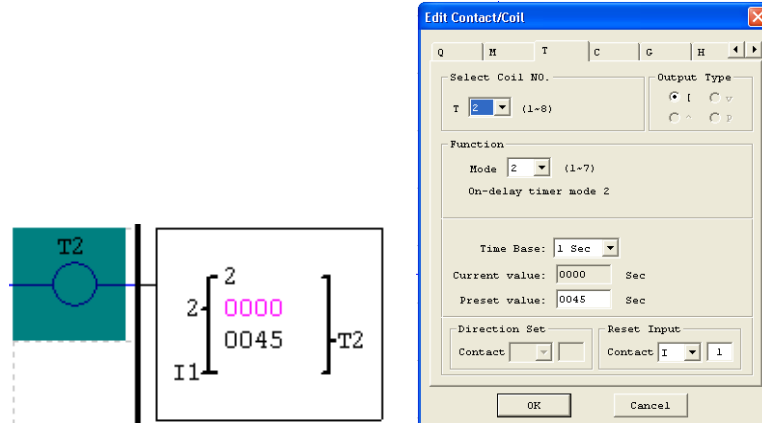


Figure C.13 T2 window and the parameters

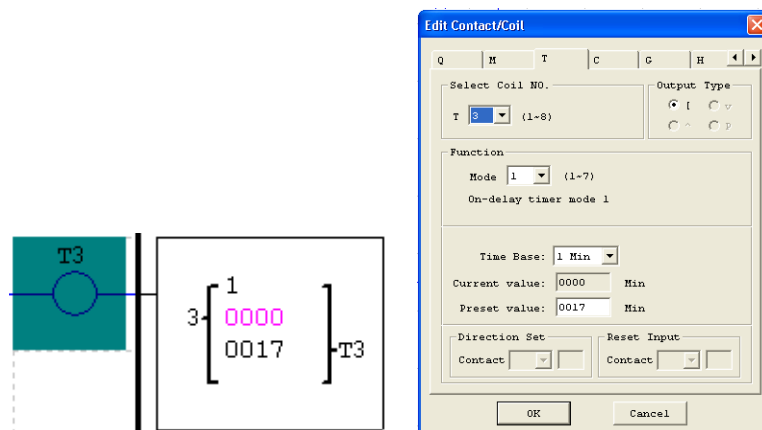


Figure C.14 T3 window and the parameters